UNIVERSITY OF OSLO
Department of Physics

Thesis for the degree
Master of Science:

Steady-State Upscaling of Polymer Flow

Kristin Asklund Larssen

June 3, 2013

Abstract

The process of polymer flooding is widely used in heavy oil production. A polymer solution is injected to displace oil, and the purpose is to reduce the mobility of the displacing fluid. Polymer flow is modeled using the Todd-Longstaff model to account for the mixing of water and polymer.

Upscaling is a mathematical process in reservoir simulation which aims to replace a detailed description of reservoir rock and/or fluid properties with a coarser scale description which has equivalent properties and produces the same flow pattern. Detailed geological models may be upscaled to simulation models to decrease the number of cells. A variety of different upscaling procedures exist. Polymer upscaling refers to the upscaling of parameters in the equations describing polymer flow, and not much work has previously been done regarding this. In this study, steady-state upscaling of polymer flow is performed.

We find that there is no upscaling effect of the viscosities and the mixing parameter. The permeability reduction factor R_k is upscaled using the flow-based technique, and the upscaled values are found to be functions of both direction and saturation. Upscaled values for the residual resistance factor RRF are found using the upscaled R_k values, and thus also these depend on direction and saturation.

Four different cases are upscaled, and the results are evaluated for two of these. The solutions obtained using the small-scale parameters on the fine grid are compared with the solutions obtained using upscaled values on the coarse grid, and the solutions are relatively similar. The saturation dependence of RRF appears to be weak, and solutions obtained using the mean of the saturation dependent upscaled RRF values as a single upscaled value are very similar to solutions obtained using the upscaled RRF values as functions of saturation. We therefore suggest to neglect the saturation dependence and instead use the mean of the upscaled RRF values as a single upscaled value. More tests should however be run to see if this is a valid approximation in general.

Acknowledgements

The master's thesis was written in cooperation with SINTEF, and is my completion of a Master's degree in Physics of Geological Process at the University of Oslo, finishing June 2013.

I would first and foremost like to thank my supervisors, Professor Knut-Andreas Lie, Dr. Marcin Dabrowski, and Dr. Daniel Schmid. Especially, I would like to thank my main supervisor Knut-Andreas for giving me the opportunity to write my thesis at his research group at SINTEF. Thank you for always being interested in my work, for always knowing what is best to do, and for making time for me, even though I know how busy you can be. Thanks to everyone at the group of Applied Mathematics at SINTEF, and especially the group of Porous Media Flow, for making me feel welcome and for always willingly answering my questions. A special thanks to Xavier Raynaud, for always showing great interested and wanting to discuss my results.

I would also like to thank everyone at PGP. A special thank you to the PhD and master students, for making my studies a fun experience and for learning me to work hard.

Finally, I would like to thank my friends and family for always being there for me. A special thank you to Ragnhild and Anette for being excellent housemates.

Contents

List of Symbols

$c_{\max}$	Maximum polymer concentration	16
Γ	Side face of domain	22
λ	Mobility	6
μ	Viscosity	6
Ω	Domain	22
ω	Mixing parameter	15
ϕ	Porosity	5
ρ	Density	7
A	Area of side face	24
c	Polymer concentration	15
C_p^a	Amount of adsorbed polymer	17
$C_p^{a,max}$	Maximum amount of adsorbed polymer	17
f	Fractional flow function	7
g	Gravity	7
K	(Absolute) permeability	5
k_r	Relative permeability	6
L	Length of domain	23
M	Mobility ratio	11
p	Pressure	7
p_c	Capillary pressure	7
PV	Total pore volume	25
q	Sources and sinks	7
R_k	Permeability reduction factor	17
RRF	Residual resistance factor	17
s	Saturation	5
S_{dpv}	Fraction of pore volume inaccessible to polymer	19
t	Time	7
V	Total volume of material	5
v	Flux	7
V_V	Volume of void space in a material	5

Chapter 1

Introduction

The first oil was found on the Norwegian continental shelf in the very end of the 1960s, and it represents the beginning of the Norwegian oil adventure. Today, the petroleum industry is our biggest industry, and it has been of great importance for Norway's economic growth. Even though oil has been produced on the Norwegian Continental Shelf for over 40 years, far from all the resources have been exploited. In addition to searching for new oil fields, the percentage of oil recovered from a field needs to be improved. Today many oil fields are classified as empty when as much as half of the oil still is left in the reservoir. On average, fields on the Norwegian shelf have a recovery factor of 46 percent for oil [3]. This shows that we still lack sufficient knowledge to fully make use of the oil resources we have, and that there is still need for more research in this area.

There are several methods that can be used to better understand the properties of an oil reservoir and the processes of oil recovery. One way is to do experiments, usually then on a smaller scale, of a similar system and see how it behaves and then relate this to actual oil reservoirs. This can give some insight, but the experiment will never be exactly similar to an oil reservoir, so the relevance and validity of the experimental results are not given. Oil reservoirs can also be studied by using differential equations that describe the fluid flow in the reservoirs. These equations along with boundary and initial conditions make up what is called a mathematical model of the system. Petroleum reservoirs are complex systems, and in general simplifications and assumptions must be made to obtain a mathematical model of the reservoir. In most cases, the equations must be solved numerically, but if enough simplifications and assumptions are made, the equations can in some cases be solved analytically. In many cases, the reservoir must be assumed to be homogeneous and isotropic to obtain an analytical solution, and as this is clearly not the case in reality, solving the equations numerically is mostly done.

Computer models are widely used in the oil industry today. Though computer models are not exact descriptions of reservoirs, they can be good approximations and give valuable insight into how a system will behave under certain conditions. Experiments can be performed numerically, which gives the advantage of investigating the effect of different parameters quite easily and to control parameters that could be hard to control in an actual experiment. It is not straight forward to make a good computer model, and even though many exist today, there is still room for improvements and there are many issues that need to be solved.

The process of oil recovery consists of several stages, and in this thesis the focus is on enhanced oil recovery, which is the latest phase in oil recovery. Specifically, we will consider polymer flooding which is widely used in heavy oil production. A mathematical model describing polymer flow is used

to study the system, and the equations are solved numerically. The main purpose of this thesis is to develop techniques for upscaling parameters in the mathematical model describing polymer flow. These are parameters that depend on rock type, and can vary a lot on small scale, and therefore need to be upscaled in order to solve the system on a grid coarse enough for computers to handle it. Polymer upscaling is an unexplored field where not much work has previously been done.

The following chapter is meant to present some background information about oil recovery, and an introduction to fluid flow in reservoirs is given.

1.1 Oil Reservoirs

Oil is formed from organic matter buried by sediments. As time goes, organic matter is buried deeper and deeper, and an increase in temperature and pressure along with geochemical reactions can lead to breakdown of the organic matter and formation of oil and gas. If petroleum is formed, it will migrate through the surrounding porous rock and follow the path of least resistance. Since petroleum is less dense than water it will almost always try to move upwards, but capillary forces and the permeability of the rock will also affect the flow. Some of the petroleum will escape and rise to the surface, while some will be trapped beneath low-permeability layers, and it is this trapped oil that make up the oil reservoirs.

Almost all petroleum occurs in sedimentary rocks, and then mostly in sandstones and carbonates. The rock structures are often layered with different rock types in different layers. The reservoir rock has void spaces were fluids can flow, and these void spaces are called pores. The porosity of a rock is a measure for the amount of void space, and the amount, placement and connection of pores have huge impact on the flow through the rock, as fluids can only flow through pores. Porosity along with permeability, which is a measure for a rock's ability to transmit fluids, is two of the main variables that determine the flow through the rock.

Reservoirs are generally heterogeneous and consist of different types of rocks with fractures and faults. The size of reservoirs naturally varies, but they typically extend over several kilometers in the horizontal direction and a few tens of meters in the vertical direction. Reservoirs can be found at different depths beneath the surface, from just below the surface to several kilometers. North Sea reservoirs can typically be found about 1-3 km below the ocean floor [1].

1.2 Oil Recovery

This section is mainly based on [5] and [14], and is meant to give a short introduction to the different processes in oil recovery. The process of oil recovery is complex and includes several stages, and some of these are mentioned and briefly discussed in this section.

The fact that many oil reservoirs are found several kilometers below the ocean floor, which in turn is below hundreds of meters of ocean and hundreds of kilometers offshore makes the process of recovery anything but straight forward. Various techniques have been developed to enable the recovery of oil, but common for all are that they involve recovering the hydrocarbons through wells drilled into the reservoir rock. Though it is not always a clear distinction between the phases in oil recovery, the process of oil recovery is often divided into three phases: primary, secondary, and tertiary (also called enhanced oil recovery).

Primary recovery is driven by natural forces and by energy that is already in the system. It is recovery without injection of any external fluids or heat to drive it. A well is drilled into the reservoir and oil can be pushed up the well due to the naturally high pressure in the reservoir. As oil is produced, the pressure in the reservoir decreases, and thus also the amount of oil pushed up to the surface is reduced. During primary recovery the reservoir essentially contains only a single fluid such as gas or oil, as the presence of water can usually be neglected. Pumps can be used to recover more oil at this stage, but still about 70-85 percent of the hydrocarbons are usually left in the reservoir after the stage of primary recovery.

Secondary recovery involve injection of external fluids. These can be water or gas, and the purpose of the injection is to sweep the oil towards production wells and to maintain the pressure in the reservoir. The process of injecting water to displace oil is called waterflooding. In some cases, the displacement front between water and oil may become highly unstable due to high viscosity contrasts between water and oil, and therefore waterflooding can be highly influenced by viscous fingering. That is, water "fingers" can penetrate through the oil and create an unstable displacement. This can lead to a not very effective sweep pattern and leave much of the oil in the reservoir. Oil can also get trapped in small pores and not be washed out due to surface tension. When water has reached the production wells and is mainly produced instead of oil, this stage is not necessarily profitable anymore. After the process of water flooding, there is usually left 50 percent or more of the hydrocarbons in the reservoir.

Enhanced oil recovery is all the recovery performed after secondary recovery. It includes injection of materials and fluids that are not normally present in a reservoir, like special fluids as chemicals, miscible gases, or injection of thermal energy. Chemicals injected can be alkaline, surfactant and polymer. Polymer flooding is the process of injecting a polymer solution to increase the viscosity of the water so that it can better displace the oil, and as this process is the focus in this thesis is it described in detail in the next chapter.

1.3 Geological Models and Reservoir Simulation

The primary goal of reservoir simulation is to predict future performance of a reservoir and find ways and means of optimizing the recovery of some of the hydrocarbons [5]. Oil reservoirs are complex systems, and thus numerical methods must usually be used to solve the equations governing the flow in a reservoir. Mathematical models can be solved numerically using several methods, where the most known are finite differences, finite elements and finite volumes. The two-point flux approximation (TPFA) scheme conserves mass and is often used in reservoir simulations. The pressure gradient over a face is found from the difference in pressure in the cell centers of the two cells sharing the face. The flux over a face is proportional to the pressure difference over that face.

Reservoirs are made up of rock and fluids filling the rock, where the fluids present depend on the stage of recovery. Figure 1.1 shows an example of a section of a reservoir grid consisting of three types of rock. The reservoir rock is usually heterogeneous and consists of different types of rock with different properties, and these properties may vary a lot over short distances. A **geological model** can be made by geologists, and it is a fine-grid representation of a reservoir that is made in the meaning of reproducing the geological heterogeneity of the reservoir. Making a geological model is not easy, as there is only limited information and data available and one can not know for certain the types and properties of rock everywhere in a reservoir. Seismic data, well-logs and core samples

can be used to obtain information about a reservoir, but whereas seismic data has the drawback of a too poor resolution, the other three methods only give information about a very limited area in the reservoir.

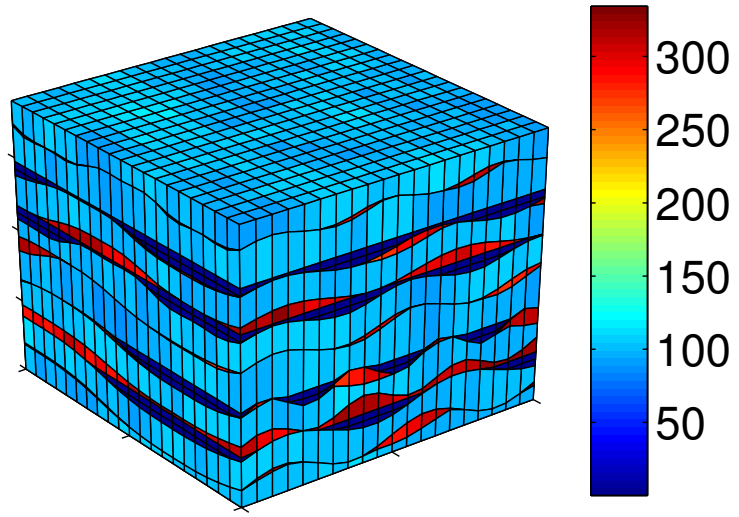

Figure 1.1: *Example of a section of a reservoir grid with horizontal layering. The colorbar shows absolute permeability in mD.*

A geological model is three-dimensional and consists of cells that represent volumes of constant properties. The size of the grid cells is usually 10-100m in the horizontal direction and 10cm-10m in the vertical direction [2]. A geological model is usually finer in the vertical direction than in the horizontal because the rock composition may change abruptly in the vertical direction because of horizontal layering in the reservoir. Also reservoirs can typically extend several kilometers in the horizontal direction and in the range of meters in vertical direction. Heterogeneities on a smaller scale than this are not captured, but still a geological model is usually too detailed and has a too fine grid to be used directly in flow simulations.

Flow simulations are usually performed on coarser models mainly because a geological model has too many grid cells from a numerical point of view. One might think that as time goes and computer power increases, computers will soon be able to handle present geological models and that there will be no need to be able to handle different scales and upscaling in the future. However, this appears not to be the case because the geological models also seem to become more and more detailed and complex, and thus it is believed that it will continue to be a need for upscaling. One might also argue that another reason for performing upscaling is that we are often mainly interested in the large scale flow pattern, often on kilometer scale, in a reservoir. We do not need to know the flow through every single pore on micrometer scale, and thus it would be useful to have a method for obtaining the correct large scale flow pattern without actually having to find the flow in every pore.

1.4 Flow in Porous Media

The flow of oil and other fluids through reservoirs can be studied by using the equations for flow in porous media. As mentioned earlier, fluids flow through the pores of the reservoir rock, and

porosity is a measure of the amount of void spaces in the rock. Porosity can be defined as

$$\phi = \frac{V_V}{V},$$

where ϕ is porosity, V_V is the volume of void space, and V is the total volume of the medium. A high porosity corresponds to a medium with a lot of void space, and therefore it is easier for a fluid to flow in a medium with high porosity. Porosity is typically in the range of 0.1-0.3 in a North Sea reservoir [1].

The flow through the rock is also dependent on the rock's **permeability** K. Permeability is a measure of the ability of a rock to transmit fluids, and depends on how well pores are connected and can make fluid paths. Permeability K, often also referred to as absolute permeability, is usually given in units Darcy (D) or milli-Darcy (mD), but the SI-units are m^2. 1 Darcy is equivalent to $0.98692 \cdot 10^{-12}$ m^2 Since permeability is dependent on the rock, it will therefore vary in the heterogeneous rock of a reservoir. K may be a full tensor

$$\mathbf{K} = \begin{pmatrix} K_{xx} & K_{xy} & K_{xz} \\ K_{yx} & K_{yy} & K_{yz} \\ K_{zx} & K_{zy} & K_{zz} \end{pmatrix},$$

where the permeability in one direction depends on the permeability in other directions. In some cases, $\mathbf{K}$ can be assumed to be a diagonal tensor, so that all off-diagonal terms are assumed to be zero. Permeability may also be a scalar, and then the porous medium is said to be isotropic.

There may be one or several fluids in a reservoir. If more than one fluid phase is present, the **saturation** of the fluid phases must be introduced. The saturation s_γ of a fluid phase γ is a measure of the volume fraction occupied by that phase, and it is in the range of 0-1. The saturations of different phases must sum up to one:

$$\sum_{all\ phases} s_\gamma = 1.$$

For an oil-water system, this gives $s_w + s_o = 1$.

If more than one fluid phase is present, the permeability and the ability of a fluid to flow is reduced. It can be reduced by a factor between 0 and 1, and this factor is called **relative permeability** $k_{r\gamma}$, for phase γ. The effective permeability, or phase permeability, can be defined as the product between absolute permeability and the relative permeability of the phase

$$\mathbf{K}_\gamma = \mathbf{K} k_{r\gamma}$$

Relative permeability is a function of saturation, and typical relative permeability curves for an oil-water system are shown in Figure 1.2. Different types of rock usually have different relative permeability curves.

Viscosity is a fluid property. It is a measure of a fluid's "inner" resistance to flow, usually denoted by the symbol μ. To explain this, the example of honey is often given. Honey has a high viscosity and can be said to flow slowly, whereas water has a lower viscosity and flows easier or faster.

The **mobility** of a phase γ can be defined as relative permeability of the phase divided by its viscosity

$$\lambda_\gamma = \frac{k_{r\gamma}}{\mu_\gamma}.$$

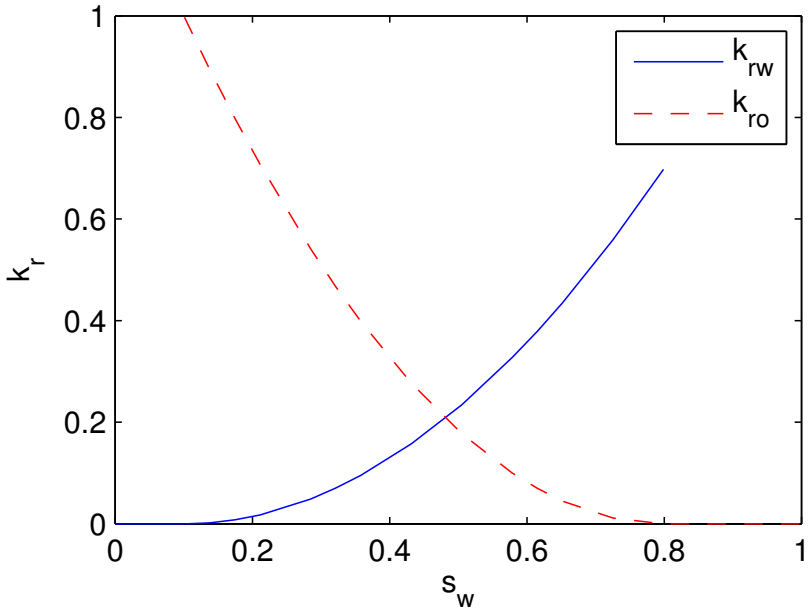

Figure 1.2: *Example of possible relative permeability curves. The blue line represents the relative permeability of water, whereas the red dashed line is relative permeability of oil. Both are functions of water saturation.*

If there is more than just one phase, the total mobility is given as

$$\lambda_t = \sum_{all\ phases} \lambda_\gamma.$$

One can then introduce the **fractional flow** function

$$f_\gamma = \frac{\lambda_\gamma}{\lambda_t},$$

which is the fraction of phase γ of the total flow.

When more than one fluid is present, there will be a discontinuity in fluid pressure across an interface between two immiscible fluids. This is due to interfacial tensions that exist at the interface, and the difference in pressure over the interface is called **capillary pressure**. In an oil-water system the capillary pressure is

$$p_c(s_w) = p_{oil} - p_{water}.$$

Capillary pressure is a function of saturation and depends on the type of rock. In some cases, capillary pressure can be neglected, thus giving $p_o = p_w = p$.

1.4.1 Single-Phase Flow

The fundamental principle of mass conservation gives the following equation:

$$\frac{\partial \rho\phi}{\partial t} + \nabla \cdot (\rho \mathbf{v}) = q. \tag{1.1}$$

This equation will be referred to as the equation for conservation of mass or the continuity equation. Here, ρ is the density of the fluid, ϕ is the porosity of the rock, q denotes sources and sinks (positive for injection), and $\mathbf{v}$ is the superficial Darcy velocity. The superficial Darcy velocity, $\mathbf{v}$, will be referred to as the flow velocity.

The flow velocity is given by an empirical relation found by Darcy:

$$\mathbf{v} = -\frac{\mathbf{K}}{\mu}\left(\nabla p - \rho \mathbf{g}\right), \tag{1.2}$$

which is referred to as Darcy's law. Here, $\mathbf{K}$ is permeability, μ is the fluid's viscosity, p is the pressure, and $\mathbf{g}$ is the gravity vector.

Equation (1.2) can be inserted into Equation (1.1):

$$\frac{\partial \rho \phi}{\partial t} + \nabla \cdot \left(-\rho \frac{\mathbf{K}}{\mu}\left(\nabla p - \rho \mathbf{g}\right)\right) = q. \tag{1.3}$$

This equation can be solved for pressure when appropriate boundary and initial conditions are given.

In some cases, it is a valid approximation to assume that the fluid and rock are incompressible and that the porosity is constant in time. In this case, the term most to the left in Equation (1.3) can be dropped. This leads to a simplification of Equation (1.3). If there are no sources or sinks, Equation (1.3) can be written:

$$\nabla \cdot \left(\frac{\mathbf{K}}{\mu}\left(\nabla p - \rho \mathbf{g}\right)\right) = 0.$$

If one also neglects gravity, the equation can be further simplified to

$$\nabla \cdot \left(\frac{\mathbf{K}}{\mu} \nabla p\right) = 0.$$

To solve this equation for pressure, boundary and initial conditions must be prescribed. The choice of boundary and initial conditions depends on the system one wishes to study, but in the case of large-scale flow in an oil reservoir it may be naturally to introduce no-flow boundary conditions at the edges of the reservoir as one usually wants the fluids to enter and leave the reservoir through wells rather than at the boundaries of the reservoir.

1.4.2 Multiphase Flow

The equations for single phase flow can be extended to multiphase flow. Each fluid phase occupies a volume fraction, and this is given by the saturation. Also a fluid's ability to flow is reduced due to the presence of other phases, and this is included in the equations through relative permeability.

Some more effects must be included in the equations and there must be one equation governing each fluid phase. Each fluid phase occupies a volume fraction, and this is given by the saturation. Also the reduction in a fluid's ability to flow is reduced due to the presence of other phases, and this is included in the equations through relative permeability.

Mass conservation gives for phase γ:

$$\frac{\partial \phi \rho_\gamma s_\gamma}{\partial t} + \nabla \cdot \left(\rho_\gamma \mathbf{v}_\gamma\right) = q_\gamma, \tag{1.4}$$

where ϕ still is the porosity, ρ_γ is the density, s_γ is the saturation, $\mathbf{v}_\gamma$ the flow velocity, and q_γ denotes sources and sinks in phase γ, while t is time.

The velocity of phase γ can be related to the phase pressure through Darcy's law:

$$\mathbf{v}_\gamma = -\frac{k_{r\gamma}}{\mu_\gamma}\mathbf{K}\left(\nabla p_\gamma - \rho_\gamma \mathbf{g}\right). \tag{1.5}$$

Similar to what was done for single-phase flow, Equation (1.5) can be inserted into Equation (1.4)

$$\frac{\partial \phi \rho_\gamma s_\gamma}{\partial t} - \nabla \cdot \left(\rho_\gamma \frac{k_{r\gamma}}{\mu_\gamma}\mathbf{K}\left(\nabla p_\gamma - \rho_\gamma \mathbf{g}\right)\right) = q_\gamma.$$

In the case of incompressibility and no source terms, the equation can be written for phase γ:

$$\frac{\partial \phi s_\gamma}{\partial t} - \nabla \cdot \left(\frac{k_{r\gamma}}{\mu_\gamma}\mathbf{K}\left(\nabla p_\gamma - \rho_\gamma \mathbf{g}\right)\right) = 0.$$

For multiphase flow we also have that the fluids fill up the pore volume, so the saturations must sum up to unity:

$$\sum_{all\ phases} s_\gamma = 1.$$

The capillary pressure relates the pressure on each side of an interface, and it equals the difference between the pressure on each side of the interface.

Two-Phase Flow: Oil-Water System

We now look closer at the equations for a system with two fluids, where the fluid phases are oil (o) and water (w). For each phase (when incompressibility and no source terms are assumed) we have:

$$\frac{\partial \phi s_w}{\partial t} - \nabla \cdot \left(\frac{k_{rw}}{\mu_w}\mathbf{K}\left(\nabla p_w - \rho_w \mathbf{g}\right)\right) = 0,$$

$$\frac{\partial \phi s_o}{\partial t} - \nabla \cdot \left(\frac{k_{ro}}{\mu_o}\mathbf{K}\left(\nabla p_o - \rho_o \mathbf{g}\right)\right) = 0.$$

The saturations must sum up to unity:

$$s_o + s_w = 1.$$

Capillary pressure relates water and oil pressure:

$$p_c(s_w) = p_o - p_w.$$

When appropriate boundary and initial conditions are given, these equations can be solved for p_w, p_o, s_w, and s_o. If capillary pressure is neglected, we have that $p_w = p_o$.

Chapter 2

Polymer Flow

Polymer flooding is the process of injecting a polymer solution to displace oil. During flooding with water the displacement front can get unstable because of a high mobility ratio between water and oil. The mobility ratio, here for water and oil, is defined as the ratio of the displacing fluid mobility to the displaced fluid mobility:

$$M = \frac{\lambda_w}{\lambda_o} = \frac{\frac{k_{rw}}{\mu_w}}{\frac{k_{ro}}{\mu_o}} = \frac{k_{rw}\mu_o}{k_{ro}\mu_w}.$$

This is the primary factor that affects the sweep efficiency. Water is here the displacing fluid, whereas oil is the displaced fluid. The purpose of injecting polymer diluted in water is to decrease the mobility of the displacing fluid and thus decreasing the mobility ratio, as that will lead to a more efficient sweep pattern. The mobility of the displacing fluid can be decreased by either increasing the viscosity or decreasing the relative permeability, and both these effects are achieved by adding polymer. A polymer solution will have a higher viscosity than water, and the rock permeability to water will be reduced when polymer is present. The presence of polymer does not affect the mobility of oil. The difference in sweep pattern in the case of water flooding versus polymer flooding is illustrated in Figure 2.1.

In this chapter a background on polymer flooding is given, and the equations governing polymer flow are presented. This chapter is mainly based on [13] and [15].

2.1 Polymer

A polymer is a material with repeating structural units and consists of molecules with high molecular mass. Examples of well-known polymers are plastic, DNA, and proteins. The most commonly used polymers in oil recovery are a synthetic material called HPAM and a biopolymer called xanthan. These have mainly been used because they are both used extensively in other industries, such as in paper manufacturing and as a thickener in the food industry. To study the chemical structure of the polymers is important, as it is found that virtually all of the important physical properties of polymer, including flow behaviour and adsorption, can be understood in terms of the molecular structure of the polymer [15]. However, how the physical properties can be understood from the molecular structure is not the focus of this thesis and will not be further discussed.

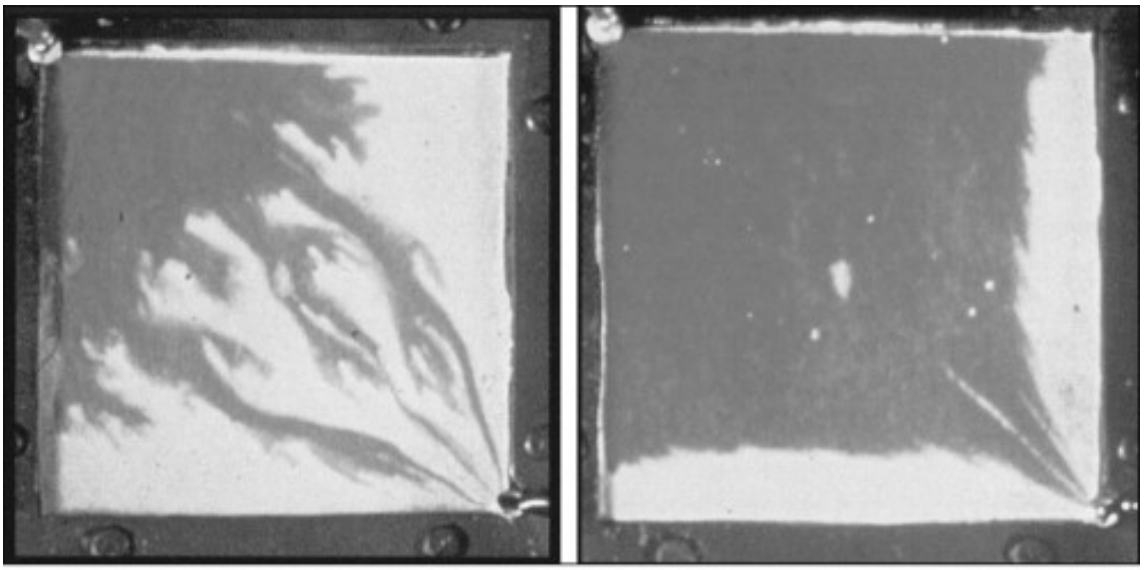

Figure 2.1: *Schematic of macroscopic displacement efficiency improvement by polymer flooding (b) over waterflooding (a). Figure from [14].*

2.2 Properties of Polymer Solutions

As already mentioned, the presence of polymer increases the viscosity and reduces the relative permeability of the displacing fluid. The viscosity of the polymer solution depends on the size and the extension of the polymer molecules in that particular solution. Polymers with larger molecules are generally associated with higher solution viscosities. Also, obviously, the viscosity depends on the concentration of polymer in the solution.

When a polymer solution is injected into the porous rock, the polymer will often interact with the rock and some polymer may be retained. When polymer is retained by the rock it will lead to a lower concentration of polymer in the solution and thus decrease the viscosity. However, the retention may also cause some reduction in the permeability of rock to water and thus in that way contribute to oil recovery. Despite this reduction in the rock's permeability to water, the retention of polymer tends to reduce oil recovery [15].

Polymer retention is one of the key factors in understanding polymer flow. Retention is used about all the mechanisms that remove polymer from the transported aqueous phase, and can be divided into three mechanisms: polymer adsorption, mechanical entrapment, and hydrodynamic retention. Mechanical entrapment is when polymer molecules are too large to pass through narrow pores in the rock, whereas hydrodynamic retention is when polymer molecules are trapped temporarily in stagnant flow regions by hydrodynamic drag forces. Polymer adsorption refers to the interaction between the polymer molecules and the rock surface. When the polymer and rock interact, polymer molecules may get bound to the rock surface. The larger surface area of rock, the more polymer can be adsorbed. The three mechanisms are illustrated in Figure 2.2. According to Sorbie [15], polymer adsorption is the most important mechanism to study in polymer flooding.

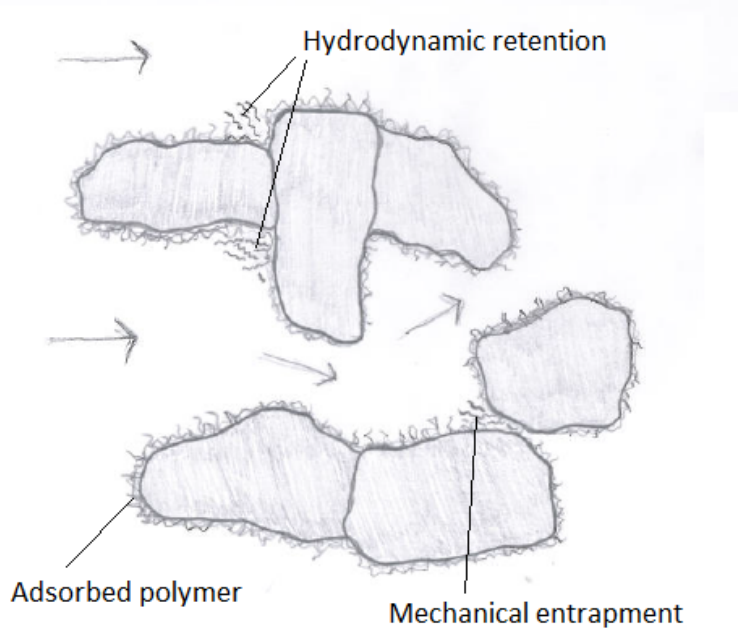

Figure 2.2: *Illustration of the three different polymer retention mechanisms in porous media: Adsorption, mechanical entrapment and hydrodynamic retention.*

2.3 Equations Governing Polymer Flow

In this sections the equations governing polymer flow are presented and explained. For simplicity, gravity and capillary forces are neglected, and fluids and rock are assumed to be incompressible.

During polymer flooding there are three fluid phases present in the reservoir; a hydrocarbon phase, a pure water phase, and a phase consisting of polymer diluted in water. Polymer is assumed to only move and spread in the water, and the oil phase is assumed to be unaffected by the presence of polymer. The polymer phase has a polymer concentration c. Polymer will mix with and spread out in the water, and thus the polymer solution and water phase are miscible with each other. Polymer and water are considered to be immiscible with the hydrocarbon phase.

Two fluids are miscible if the molecules of one fluid can freely mix with the molecules in the other fluids, and there is no interface between the two fluids. Two fluids are immiscible if there is a well-defined interface between the two fluids and they stay distinct. Miscible fluids mix with each other, whereas immiscible do not.

The equations governing a two-phase system with water and oil was stated in Section 1.4.2. For polymer flow we will have one equation governing the oil phase, one describing the total water phase, and one for the polymer phase. The equation governing water will be altered because of the presence of polymer, whereas the equation governing the oil phase is unchanged as the presence of polymer is assumed to not affect the oil phase. The equation governing oil is therefore as stated earlier:

$$\phi \frac{\partial s_o}{\partial t} - \nabla \cdot \left[\frac{\mathbf{K} k_{ro}}{\mu_o} \nabla p \right] = 0,$$

where ϕ is porosity, s_o is oil saturation, $\mathbf{K}$ is absolute permeability, k_{ro} is relative permeability of oil, and μ_o is oil viscosity.

2.3.1 Mixing of Polymer and Water

When a polymer solution with concentration c is injected and comes in contact with pure water they will start to mix. Modeling this process is not straight forward.

Todd and Longstaff [16] discuss how to model miscible flow. In recovery processes there is often an unstable front moving, which can be fingering due to viscosity differences or because of gravity and density differences. Todd and Longstaff [16] argue that a successful miscible-flood simulator should allow for the possibility of unstable frontal advance and must also describe the dispersion phenomenon, but that attempts on making simulators solving the equations for miscible flow have been met with limited success. This is mainly because of numerical dispersion and the need of a very fine grid structure to model the unstable front.

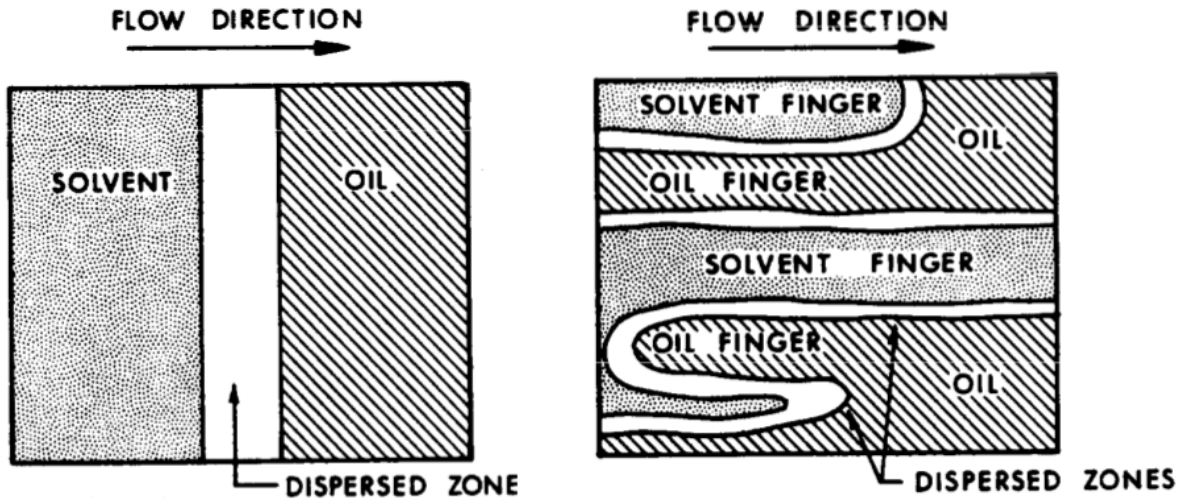

Figure 2.3: *Figure from [16] that shows two different possible displacement fronts in a grid block. To the left we see a stable front, while to the right we see an unstable front with fingering. The width of the dispersed zone (white area in the figures) is determined by ω. When $\omega = 0$ it corresponds to no mixing and no dispersed zone, whereas $\omega = 1$ corresponds to full mixing and that the dispersed zone fills the whole grid block. The main purpose of the Todd-Longstaff model is that the displacement front does not have to be modeled in detail, only the thickness of the dispersed zone matters in the model.*

Todd and Longstaff suggest an alternative way to model miscible flow where the unstable front does not have to be reproduced. A way to model miscible flow without actually solving the equations for miscible flow is suggested, and this will be referred to as the Todd-Longstaff model. It is suggested to model two miscible fluids as two immiscible fluids, where the effect of mixing is included in altered parameters. Then a coarser grid can be used, as the fine structure of the flow does not have to be reproduced. Todd and Longstaff [16] suggest to alter the viscosities, densities, and relative permeabilities to account for mixing, and introduce a new variable ω to be used in the alternation. This new variable, ω, is called the mixing parameter, and must be in the range of $[0, 1]$; $\omega = 1$ corresponds to full mixing, $\omega = 0$ corresponds to no mixing, whereas an ω between 0 and 1 will correspond to partially mixing. Two different possible displacement fronts are illustrated in Figure 2.3, and ω essentially describes the width of the dispersed zone compared to the size of the grid block. The Todd-Longstaff model is used to model the mixing of polymer and water, but only the viscosities are altered to account for the mixing. This is because the density of the aqueous

phase is assumed to be independent of polymer concentration and unaffected by the presence of polymer, and also the relative permeability is assumed to be the same as that of pure water.

The altered viscosities of the water phase and the polymer phase depend on the local concentration of polymer. From Todd and Longstaff [16], the viscosities of partially mixed water and polymer are:

$$\mu_{w,e} = \mu_m(c)^{\omega}\mu_w^{1-\omega},$$
$$\mu_{p,e} = \mu_m(c)^{\omega}\mu_p^{1-\omega}.$$

Here, μ_w is the viscosity of pure water, μ_m is the viscosity of a fully mixed polymer solution, and μ_p is the viscosity of the polymer solution at maximum polymer concentration: $\mu_p = \mu_m(c_{\max})$. See that when it is fully mixed ($\omega = 1$), then $\mu_{w,e} = \mu_{p,e} = \mu_m(c)$, so then the viscosities of the polymer and water are equal as they should be when fully mixed. When there is no mixing ($\omega = 0$), then $\mu_{w,e} = \mu_w$ and $\mu_{p,e} = \mu_p$, and the altered viscosities equal the viscosities of the pure components.

The equations for the pure water phase and polymer phase, when using the altered viscosities and incompressibility is assumed, are:

$$\phi\frac{\partial s_{ww}}{\partial t} + \nabla\cdot(\mathbf{v}_{ww}) = 0, \qquad \mathbf{v}_{ww} = -\mathbf{K}\frac{k_{rww}}{\mu_{w,e}}\nabla p,$$

$$\phi\frac{\partial s_{wp}}{\partial t} + \nabla\cdot(\mathbf{v}_{wp}) = 0, \qquad \mathbf{v}_{wp} = -\mathbf{K}\frac{k_{rwp}}{\mu_{p,e}}\nabla p.$$

The total saturation of the water phase is the sum of the pure water saturation and polymer solution saturation: $s_w = s_{ww} + s_{wp}$. The effective polymer viscosity is defined to be equal to the viscosity of the polymer solution:

$$\mu_{p,\text{eff}} = \mu_{p,e} = \mu_m(c)^{\omega}\mu_p^{1-\omega}.$$

The total water equation can now be written as the sum of contributions from the polymer solution and the pure water:

$$\phi\frac{\partial(s_{ww}+s_{wp})}{\partial t} + \nabla\cdot(\mathbf{v}_{ww}+\mathbf{v}_{wp}) = 0.$$

The saturation of pure water and water with polymer are related to the polymer concentration:

$$s_{ww} = \left(1 - \frac{c}{c_{\max}}\right)s_w, \quad s_{wp} = \frac{c}{c_{\max}}s_w.$$

If we let

$$k_{ww}(s_{ww}) = \left(1 - \frac{c}{c_{\max}}\right)k_w(s_w), \quad k_{wp}(s_{wp}) = \frac{c}{c_{\max}}k_w(s_w),$$

then the total water equation can be written

$$\phi\frac{\partial s_w}{\partial t} - \nabla\cdot\left[\mathbf{K}\left(\frac{k_{rww}}{\mu_{w,e}} + \frac{k_{rwp}}{\mu_{p,\text{eff}}}\right)\nabla p\right] = 0,$$

or alternatively

$$\phi\frac{\partial s_w}{\partial t} - \nabla\cdot\left[\mathbf{K}k_{rw}\left(\frac{1-\frac{c}{c_{\max}}}{\mu_{we}} + \frac{\frac{c}{c_{\max}}}{\mu_{p,\text{eff}}}\right)\nabla p\right] = 0.$$

This gives

$$\frac{1}{\mu_{w,\text{eff}}} = \frac{1-\frac{c}{c_{\max}}}{\mu_{w,e}} + \frac{\frac{c}{c_{\max}}}{\mu_{p,\text{eff}}}. \tag{2.1}$$

So we have for the total water phase:

$$\phi\frac{\partial s_w}{\partial t} - \nabla\cdot\left[\mathbf{K}\frac{k_{rw}}{\mu_{w,\text{eff}}}\nabla p\right] = 0,$$

which can also be written

$$\phi\frac{\partial s_w}{\partial t} + \nabla\cdot\mathbf{v}_w = 0$$

with $\mathbf{v}_w = -\mathbf{K}\frac{k_{rw}}{\mu_{w,\text{eff}}}\nabla p$. Now we look at the equation for polymer:

$$\phi\frac{\partial s_{wp}}{\partial t} - \nabla\cdot\left[\mathbf{K}\frac{k_{rwp}}{\mu_{p,\text{eff}}}\nabla p\right] = 0.$$

We use that $s_{wp} = \frac{c}{c_{\max}}s_w$ and $k_{rpw} = \frac{c}{c_{\max}}k_{rw}$, which gives

$$\phi\frac{\partial}{\partial t}\left(\frac{c}{c_{\max}}s_w\right) - \nabla\cdot\left[\mathbf{K}\frac{c\,k_{rw}}{c_{\max}\mu_{p,\text{eff}}}\nabla p\right] = 0,$$

$$\phi\frac{\partial(cs_w)}{\partial t} - \nabla\cdot\left[c\mathbf{K}\frac{k_{rw}}{\mu_{p,\text{eff}}}\nabla p\right] = 0,$$

$$\phi\frac{\partial(cs_w)}{\partial t} + \nabla\cdot(c\mathbf{v}_{wp}) = 0,$$

where we have defined $\mathbf{v}_{wp} = -\mathbf{K}\frac{k_{rw}}{\mu_{p,\text{eff}}}\nabla p$. This equation will be used to describe the polymer phase.

We now have one equation governing the oil phase, one equation for the total water phase, and one equation for the polymer phase.

For oil:

$$\phi\frac{\partial s_o}{\partial t} - \nabla\cdot\mathbf{v}_o = 0, \qquad \mathbf{v}_o = \mathbf{K}\frac{k_{ro}}{\mu_o}\nabla p.$$

For water:

$$\phi\frac{\partial s_w}{\partial t} + \nabla\cdot\mathbf{v}_w = 0, \qquad \mathbf{v}_w = -\mathbf{K}\frac{k_{rw}}{\mu_{w,\text{eff}}}\nabla p.$$

For polymer:

$$\phi\frac{\partial cs_w}{\partial t} + \nabla\cdot c\mathbf{v}_{wp} = 0, \qquad \mathbf{v}_{wp} = -\mathbf{K}\frac{k_{rw}}{\mu_{p,\text{eff}}}\nabla p.$$

We assume that $k_{rw} = k_{rww}$. The equations stated above are simplified versions of the equations governing polymer flow. Additional effects, such as adsorption and dead pore space, are introduced and included in the equations in the next sections.

2.3.2 Adsorption and Permeability Reduction

The retention of polymer, especially adsorption and mechanical entrapment/pore blocking, leads to a reduction in the relative permeability of the aqueous phase. This can be included in the equations for water and polymer through a permeability reduction factor R_k, while the equation governing oil stays unchanged as polymer does not affect the oil phase. It is assumed that the reduction

in permeability is proportional to the amount of polymer retained by the rock. The permeability reduction factor can be given by an expression used in [4]:

$$R_k(c) = 1 + (RRF - 1)\frac{C_p^a(c)}{C_p^{a,max}}. \tag{2.2}$$

Here, RRF is the residual resistance factor, C_p^a is the amount of polymer adsorbed, while $C_p^{a,max}$ is the maximum possible adsorbed polymer. They all depend on rock type, but whereas RRF and $C_p^{a,max}$ is set to be constant in a rock type, C_p^a also depends on the concentration of polymer. When the polymer concentration is at its maximum, the amount of adsorbed polymer will equal the maximum possible adsorbed polymer: $C_p^a(c = c_{max}) = C_p^{a,max}$. Then the permeability reduction factor will equal RRF. The permeability reduction factor can be included in the equations by dividing the relative permeability of water and polymer (which is assumed to be the same) by R_k.

The residual resistance factor is defined as the decrease in mobility of water that follows a polymer solution relative to water flow before the flow of the polymer solution:

$$RRF = \frac{\lambda_w(initial)}{\lambda_w(after\ polymer)}.$$

The polymer adsorption can not be fully reversible if this definition should make any sense. The definition of RRF is from [10], and RRF is given as a constant value for each type of rock.

Polymer adsorption can be included in the equations by adding a mass accumulation term in the equation for the polymer phase. The equation governing the oil phase remains unaltered, whereas the equations governing the water and polymer phase become:

$$\phi\frac{\partial s_w}{\partial t} - \nabla\cdot\left[\frac{\mathbf{K}k_{rw}}{\mu_{w,\text{eff}}R_k}\nabla p\right] = 0,$$

$$\frac{\partial}{\partial t}(\rho_w\phi c s_w) + \frac{\partial}{\partial t}\left(\rho_r(1-\phi)C_p^a\right) - \nabla\cdot\left[\rho_w c\frac{\mathbf{K}k_{rw}}{\mu_{p,\text{eff}}R_k}\nabla p\right] = 0,$$

where ρ_r is the rock density. The adsorption of polymer can either be modeled as a reversible or irreversible process. Desorption is when the adsorbed polymer is released from the rock surface, thus the opposite of adsorption. If there is no desorption, the polymer adsorbed to the rock will continue to be bound to the rock also after the passage of polymer and then the earlier maximum concentration of polymer will matter. If desorption is included, the concentration of polymer at that specific time will matter, and it will not be history dependent. These are things to consider when deciding whether to include desorption or not, when the equations are solved numerically.

2.3.3 Dead Pore Space

In core flooding experiments it has been observed that polymer moves faster through the porous rock than tracers. This is believed to be caused by parts of the pore space being inaccessible for polymer. This inaccessible pore space can be referred to as dead pore space. The porous medium is made up of pores of different sizes, and the polymer is believed to be too large to fit through certain pore throats and therefore can not access all the pores. Since the polymer then only moves in a subset of the total pore space, it will move faster than a tracer that is moving through all the pores. The dead pore space depends on the type of rock, but is modeled as constant within each rock type. It represents the amount of total pore volume in each grid cell that is inaccessible to the polymer.

The effect of dead pore space can be included in the equations by instead of using the full pore volume in the polymer equation, only the pore volume accessible for polymer is used. We define S_{dpv} as the fraction of the pore volume that is not accessible to polymer. Including dead pore space in the equations only alters the polymer equation:

$$\frac{\partial}{\partial t}(\rho_w(1-S_{dpv})\phi c s_w) + \frac{\partial}{\partial t}\left(\rho_r(1-\phi)C_p^a\right) - \nabla\cdot\left[\rho_w c\mathbf{K}\frac{k_{rw}}{\mu_{p,\text{eff}}R_k}\nabla p\right] = 0.$$

2.3.4 Full Model and Summary

In this chapter the equations governing polymer flow has been presented. To sum up, the equations governing the oil phase, water phase, and polymer phase are stated here:

$$\phi\frac{\partial s_o}{\partial t} + \nabla\cdot\mathbf{v}_o = 0, \qquad \mathbf{v}_o = -\frac{k_{ro}(s_o,\mathbf{x})}{\mu_o}\mathbf{K}(\mathbf{x})\nabla p, \tag{2.3}$$

$$\phi\frac{\partial s_w}{\partial t} + \nabla\cdot\mathbf{v}_w = 0, \qquad \mathbf{v}_w = -\frac{k_{rw}(s_w,\mathbf{x})}{\mu_{w,\text{eff}}(c)R_k(c,\mathbf{x})}\mathbf{K}(\mathbf{x})\nabla p, \tag{2.4}$$

$$\phi\frac{\partial}{\partial t}(\rho_w(1-S_{dpv})c s_w) + \frac{\partial}{\partial t}\left(\rho_r(1-\phi)C_p^a\right) + \nabla\cdot[\rho_w c\mathbf{v}_{wp}] = 0,$$

$$\mathbf{v}_{wp} = -\frac{k_{rw}(s_w,\mathbf{x})}{\mu_{p,\text{eff}}(c)R_k(c,\mathbf{x})}\mathbf{K}(\mathbf{x})\nabla p. \tag{2.5}$$

Chapter 3

Upscaling

Upscaling is a mathematical process in reservoir simulation which aims to replace a detailed description of reservoir rock and/or fluid properties with a coarser scale description which has equivalent properties. In other words, the purpose is to replace a fine model by a coarser model that gives the same flow pattern. Experience has shown that it is difficult to design a robust upscaling technique that gives reliable results for all kinds of flow scenarios. There exists a variety of upscaling techniques, and different procedures are appropriate in different situations. Different parameters can be upscaled, and upscaling techniques can be classified in terms of the parameters upscaled. Single-phase upscaling refers to upscaling of parameters in the single-phase equations, typically of porosity and absolute permeability. Two-phase upscaling refers to upscaling of parameters in the two-phase equations, like relative permeability, capillary pressure and saturation. Here, the term polymer upscaling will be used about upscaling parameters only found in the equations governing polymer flow.

Upscaling can be performed to go from geological models to simulation models, but also to go from an even smaller scale, such as BED and SBED models, and up to geological or simulation models. In either case, the purpose is to obtain the same flow pattern when using upscaled parameters compared to when using the fine-scale parameters. Upscaling is performed to reduce the number of cells, and a geological model with millions of cells can typically be upscaled to a simulation model with tens of thousands of cells. This is done by dividing the grid of the geological model into blocks, and then upscaling each block. Each block will correspond to a coarse cell.

The following chapter will present upscaling procedures for single-phase, two-phase, and polymer flow. Upscaled parameters will be denoted by an asterisk.

3.1 Single-Phase Upscaling

As mentioned, upscaling techniques can be classified in terms of the parameters upscaled, and then further in terms of the way upscaled parameters are computed. Single-phase upscaling is the most widely used and best understood form of upscaling [6]. The procedures available are simple techniques as harmonic and arithmetic means, power averaging techniques, and flow based methods. A review of different single-phase upscaling techniques is given in [8].

For single-phase flow, the parameters to upscale are porosity and absolute permeability. Porosity is

normally upscaled by simply volume averaging:

$$\phi^* = \frac{1}{V(\Omega)} \int_\Omega \phi(x) dx,$$

where V is the total volume $\int_\Omega 1 dx$. The pore volume is exactly conserved between the fine and coarse scale.

Flow-based upscaling of $\mathbf{K}$, also called numerical pressure computation technique, is performed by solving the single-phase equation in a coarse scale grid cell using the fine-scale permeability field. The solution obtained is then used to obtain an effective permeability. Figure 3.1 illustrates the upscaling of permeability, where we go from many cells on fine-scale (left) to one cell on coarse scale (right). The fine-scale grid may be a block of a larger grid that is being upscaled. After upscaling, a permeability tensor is obtained for the coarse cell.

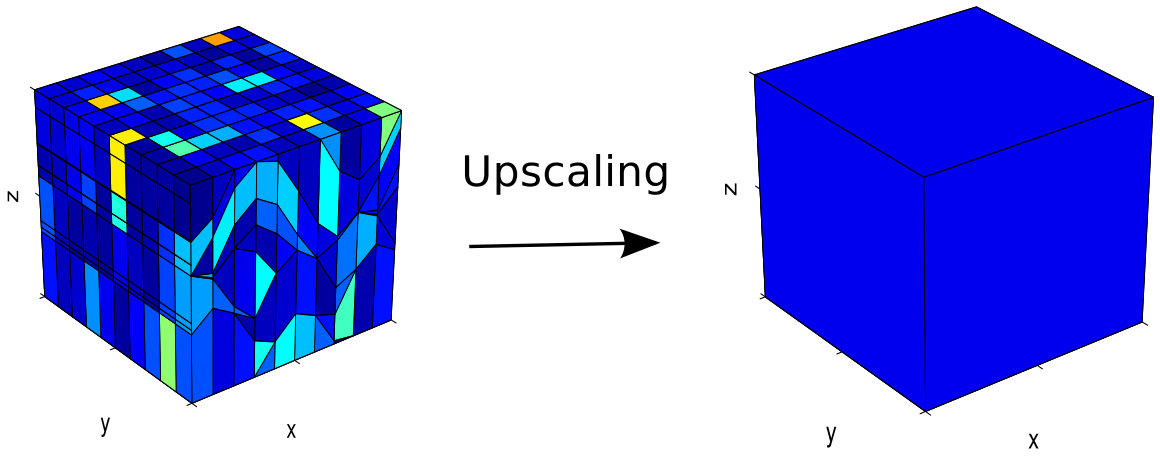

Figure 3.1: *Illustration of upscaling of permeability. The grid to the left is the fine-scale grid consisting of many cells. Upscaling is performed, and a upscaled permeability tensor is obtained for the coarse cell to the right.*

When the single-phase equation is solved in a coarse grid cell, boundary conditions must be chosen, and often a pressure gradient is set up in one direction to drive the flow. Different boundary conditions can give different upscaled values, and since it is difficult to predict in advance how the flow will be in the coarse cell, it can be difficult to know which boundary conditions to use. One possibility is to set up a pressure gradient in one direction, and then have no-flow at the boundaries in the other directions. This will give a diagonal upscaled permeability tensor. Another possibility is to use periodic boundary conditions. Periodic boundary conditions are usually more robust than fixed boundary conditions [2], and give a symmetric and positive definite tensor.

We consider a simple three-dimensional domain as illustrated in Figure 3.2. The domain has the following side faces:

$$\begin{aligned}
\Gamma_x^1 &= \{(x,y,z)\,\epsilon\,\Omega \;\mid\; x = 0\}, & \Gamma_x^2 &= \{(x,y,z)\,\epsilon\,\Omega \;\mid\; x = L_x\},\\
\Gamma_y^1 &= \{(x,y,z)\,\epsilon\,\Omega \;\mid\; y = 0\}, & \Gamma_y^2 &= \{(x,y,z)\,\epsilon\,\Omega \;\mid\; y = L_y\},\\
\Gamma_z^1 &= \{(x,y,z)\,\epsilon\,\Omega \;\mid\; z = 0\}, & \Gamma_z^2 &= \{(x,y,z)\,\epsilon\,\Omega \;\mid\; z = L_z\}.
\end{aligned}$$

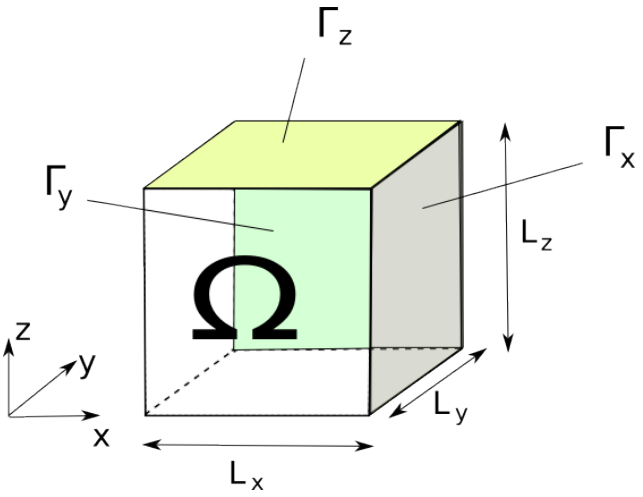

Figure 3.2: *Illustration of a simple three-dimensional domain Ω.*

Periodic boundary conditions with a pressure gradient set up in the x-direction for a domain like this are

$$v_{\Gamma_\alpha^1} = v_{\Gamma_\alpha^2}, \qquad p_{\Gamma_\alpha^2} - p_{\Gamma_\alpha^1} = \begin{cases} \Delta p_x & \text{if } \alpha = x \\ 0 & \text{if } \alpha \neq x \end{cases}$$

for $\alpha = x, y, z$.

For incompressible single-phase flow where gravity is neglected the following equation is solved

$$\nabla \cdot \left(\frac{\mathbf{K}}{\mu} \nabla p \right) = 0 \tag{3.1}$$

with chosen boundary conditions. For flow-based upscaling, the system must be solved for the pressure gradient set up in each direction to obtain a full tensor for upscaled permeability. For a three-dimensional domain, the full tensor can be written $\mathbf{K}^* = [\mathbf{K}_x^*, \mathbf{K}_y^*, \mathbf{K}_z^*]$. Here, $\mathbf{K}_x^*$ is obtained from solving with a pressure gradient in the x-direction, $\mathbf{K}_y^*$ from solving with the pressure gradient in the y-direction, and $\mathbf{K}_z^*$ from solving with the pressure gradient in the z-direction.

For the pressure gradient set up in direction β we can find $\mathbf{K}_\beta^*$ from

$$\mathbf{K}_\beta^* = -\frac{\mathbf{v}_\beta^* \mu L_\beta}{\Delta p_\beta} \tag{3.2}$$

and $K_{\alpha\beta}$ from

$$K_{\alpha\beta}^* = -\frac{v_{\alpha\beta}^* \mu L_\beta}{\Delta p_\beta}, \tag{3.3}$$

where $\beta = x, y, z$ and $\alpha = x, y, z$. Here, L_β is the length of the domain in the x-direction and Δp_β is the pressure difference over the domain in the x-direction. The upscaled flux, $v_{\alpha\beta}^*$, is obtained from solving the single-phase equation with the pressure gradient in the β-direction. We have that $v_{\alpha\beta}^* = \mathbf{v}_\beta^* \cdot \mathbf{e}_\alpha$ and that

$$v_{\alpha\beta}^* = \frac{1}{A_\alpha} \int_{\Gamma_\alpha} \mathbf{v}_\beta \cdot \mathbf{e}_\alpha \, ds.$$

Here, $v^*_{\alpha\beta}$ is the sum of the flux through a side face divided by the area of that side face. For a side face α one can chose between the faces Γ^1_α and Γ^2_α, since the flux through those faces will be the same because of periodicity. The area of the chosen side face is A_α. The unit vectors are defined as

$$\mathbf{e}_x = \begin{bmatrix} 1 \\ 0 \\ 0 \end{bmatrix}, \quad \mathbf{e}_y = \begin{bmatrix} 0 \\ 1 \\ 0 \end{bmatrix}, \quad \mathbf{e}_z = \begin{bmatrix} 0 \\ 0 \\ 1 \end{bmatrix}.$$

The flux $\mathbf{v}_\beta$ is given by

$$\mathbf{v}_\beta = -\frac{\mathbf{K}}{\mu}\nabla p_\beta.$$

Here, p_β is the solution of the single-phase equation (3.1) with the following boundary conditions:

$$v_{\Gamma^1_\alpha} = v_{\Gamma^2_\alpha}, \qquad p_{\Gamma^2_\alpha} - p_{\Gamma^1_\alpha} = \begin{cases} \Delta p_\beta & \text{if } \alpha = \beta \\ 0 & \text{if } \alpha \neq \beta. \end{cases}$$

3.2 Two-Phase Upscaling

Two-phase upscaling is not as well understood as single-phase upscaling, and is also more complex. There exist numerous techniques for upscaling two-phase parameters, and even though a lot of research has been done in this area, a robust methodology still does not exist [2].

The parameters to upscale for two-phase flow are normally relative permeability, capillary pressure, and saturation. The equations governing two-phase flow are time-dependent, and relative permeability depends on the saturation. Upscaling relative permeability will give an upscaled relative permeability corresponding to a certain saturation. Therefore, relative permeability must be upscaled for different saturation to obtain an upscaled relative permeability curve versus saturation.

Upscaling of two-phase flow parameters is often divided into two categories; steady state methods and dynamic methods. The main idea behind dynamic methods is to do simplified fine-scale flow simulations that mimic the flow pattern, whereas for steady state methods the basic principle is assuming that the system is in steady state.

For two-phase flow, the equations governing the water and oil phase (when gravity and capillary forces are neglected) are:

$$\frac{\partial \phi s_w}{\partial t} - \nabla \cdot \left(\frac{k_{rw}}{\mu_w} \mathbf{K} \nabla p \right) = 0,$$

$$\frac{\partial \phi s_o}{\partial t} - \nabla \cdot \left(\frac{k_{ro}}{\mu_o} \mathbf{K} \nabla p \right) = 0.$$

For steady-state upscaling, the system is assumed to be in steady state, and thus the time-derivative terms in the equations are neglected. Then the equations reduce to

$$\nabla \cdot \left(\frac{k_{rw}}{\mu_w} \mathbf{K} \nabla p \right) = 0, \tag{3.4}$$

$$\nabla \cdot \left(\frac{k_{ro}}{\mu_o} \mathbf{K} \nabla p \right) = 0. \tag{3.5}$$

For steady-state upscaling, one of the challenges is to obtain the correct saturation distribution at steady state. Obtaining correct saturation distribution at steady state can be done in several

ways. Assumptions can be made, *e.g.*, assuming that certain forces dominate while other forces can be neglected, and the capillary limit and viscous limit are methods often used. When capillary forces are assumed to dominate, saturations can be found from the capillary pressure (or J-function) curves, whereas when viscous forces are assumed to dominate, the saturations can be obtained from the assumption of constant fractional flow. The methods are described in [7]. A more general way to obtain the saturations is to simulate the system and solve the equations until steady state is actually reached. This method has the advantage that no assumptions need to be made, but the drawback of being computationally expensive. In this thesis, steady-state upscaling is performed, and the system is simulated until steady state is reached to obtain the solution at steady state.

An upscaled saturation value is found from the saturation distribution at steady state. Often the saturation value is found from volume averaging:

$$s_w^* = \frac{\int_\Omega \phi s_w \, dx}{\int_\Omega \phi \, dx} \, ,$$

where ϕ is porosity and the total pore volume is $PV(\Omega) = \int_\Omega \phi \, dx$.

When the solution at steady state is obtained, an upscaled relative permeability $k_{r\gamma}^*$ can be found for phase γ using the flow-based technique. On the fine scale, relative permeabilities are given as scalars, but upscaled relative permeabilities may be vectors, or even tensors in some cases. When having the pressure gradient in different directions produces different upscaled relative permeabilities, it can be given as a vector: $\mathbf{k}_{r\gamma}^*(s_w^*) = \left[k_{r\gamma,x}^*(s_w^*), k_{r\gamma,y}^*(s_w^*), k_{r\gamma,z}^*(s_w^*)\right]$, where $\gamma = w, o$. Here, we will assume that upscaled permeabilities are vectors, where in some cases the entries in the vector will be equal.

For two-phase flow, where the phases are water and oil, the upscaled water and oil relative permeabiltiy can be found from the following equations when the pressure gradient is set up in direction β:

$$k_{rw,\beta}^*(s_w^*) = -\frac{\mu_w L_\beta v_{w,\beta\beta}^*}{K_{\beta\beta}^* \Delta p_\beta}, \tag{3.6}$$

$$k_{ro,\beta}^*(s_o^*) = -\frac{\mu_o L_\beta v_{o,\beta\beta}^*}{K_{\beta\beta}^* \Delta p_\beta}. \tag{3.7}$$

Here Δp_β is the pressure difference over the domain in direction β with the pressure gradient set up in β-direction. The upscaled flux is

$$v_{\gamma,\beta\beta}^* = \frac{1}{A_\beta} \int_{\Gamma_\beta} \mathbf{v}_{\gamma,\beta} \cdot \mathbf{e}_\beta \, ds, \qquad \mathbf{v}_{\gamma,\beta} = -\frac{k_{r\gamma}}{\mu_\gamma} \mathbf{K} \nabla p_\beta,$$

so that

$$v_{\gamma,\beta\beta}^* = -\frac{1}{A_\beta} \int_{\Gamma_\beta} \frac{k_{r\gamma}}{\mu} \mathbf{K} \nabla p_\beta \cdot \mathbf{e}_\beta \, ds$$

Here, p_β is the solution of the two-phase equations (3.4) and (3.5) with the the following boundary conditions:

$$(\mathbf{v}_{\gamma,\beta} \cdot \mathbf{e}_\alpha)_{\Gamma_\alpha^1} = (\mathbf{v}_{\gamma,\beta} \cdot \mathbf{e}_\alpha)_{\Gamma_\alpha^2} \, , \qquad p_{\Gamma_\alpha^2} - p_{\Gamma_\alpha^1} = \begin{cases} \Delta p_\beta & \text{if } \alpha = \beta \\ 0 & \text{if } \alpha \neq \beta \end{cases}$$

for $\alpha = x, y, z$. The expression for $v_{w,\beta\beta}^*$ can be inserted into the expression for upscaled water relative permeability (3.6):

$$k_{rw,\beta}^*(s_w^*) = \frac{\mu_w L_\beta}{K_{\beta\beta}^* A_\beta \Delta p_\beta} \int_{\Gamma_\beta} \frac{k_{rw}}{\mu_w} \mathbf{K} \nabla p_\beta \cdot \mathbf{e}_\beta \, ds.$$

Viscosity can be moved outside the integral and eliminated:

$$k^*_{rw,\beta}(s^*_w) = \frac{L_\beta}{K^*_{\beta\beta} A_\beta \Delta p_\beta} \int_{\Gamma_\beta} k_{rw} \mathbf{K} \nabla p_\beta \cdot \mathbf{e}_\beta \, ds. \tag{3.8}$$

Similar can be done for $k^*_{ro,\beta}$ to obtain:

$$k^*_{ro,\beta}(s^*_o) = \frac{L_\beta}{K^*_{\beta\beta} A_\beta \Delta p_\beta} \int_{\Gamma_\beta} k_{ro} \mathbf{K} \nabla p_\beta \cdot \mathbf{e}_\beta \, ds.$$

3.3 Upscaling Polymer Flow

Upscaling of polymer flow is a relatively unexplored field, and there is not much literature to find. Compared to the equations for two-phase flow, some new variables are introduced in the polymer equations. These are R_k, which include C_p^a, C_p^{amax} and RRF, S_{dpv}, $\mu_{w,\text{eff}}$, $\mu_{p,\text{eff}}$ and ω, and at first sight these may all be possible candidates for upscaling. On the fine scale, the parameters S_{dpv}, R_k, C_p^a, C_p^{amax}, and RRF all depend on rock type, whereas the viscosities depend on concentration, and ω is constant. Jakupsstovu et al. [9] reported a very limited upscaling effect of ω. In this section it is shown that when performing steady-state upscaling using the flow-based technique, there will actually be no upscaling effect at all of the viscosities and ω. This is because at steady state, the polymer concentration is constant in space (shown in Section 3.3.1), and from this it follows that also the viscosities will be constant in space as they only depend on the concentration. In the following sections we also consider the upscaling of C_p^a, C_p^{amax}, RRF, and R_k. Some variables are upscaled using a simple volume averaging technique, whereas others are upscaled by solving until steady state is reached and using the flow-based technique, analogous to the upscaling of permeabilities previously explained.

3.3.1 Uniform Polymer Concentration at Steady State

In this section it is shown that the polymer concentration is constant in space at steady state. We consider a simple rectangular domain as the one illustrated in Figure 3.3. A pressure gradient is set up in the x-direction and the subscripts L and R correspond to the left and right side face of the domain, respectively, while T and B correspond to top and bottom. Gravity and capillary pressure are neglected to enhance readability, but can easily be included in the analysis.

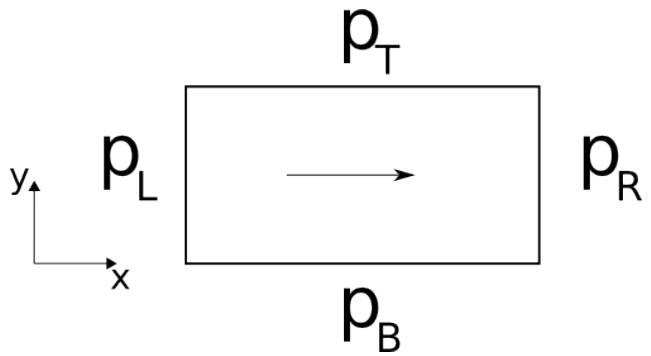

Figure 3.3: *Sketch of a simple two-dimensional domain. A pressure gradient is set up in the x-direction to drive the flow, and the arrow in the domain indicates the flow direction, thus* $p_L > p_R$.

At steady state, polymer flow is governed by the following equations:

$$\nabla \cdot \mathbf{v}_o = 0, \qquad \mathbf{v}_o = -\frac{k_{ro}(s_o, \mathbf{x})}{\mu_o}\mathbf{K}(\mathbf{x})\nabla p \tag{3.9a}$$

$$\nabla \cdot \mathbf{v}_w = 0, \qquad \mathbf{v}_w = -\frac{k_{rw}(s_w, \mathbf{x})}{\mu_{w,\text{eff}}(c)R_k(c, \mathbf{x})}\mathbf{K}(\mathbf{x})\nabla p = 0, \tag{3.9b}$$

$$\nabla \cdot c\mathbf{v}_{wp} = 0, \qquad \mathbf{v}_{wp} = \frac{k_{rw}(s_w, \mathbf{x})}{\mu_{p,\text{eff}}(c)R_k(c, \mathbf{x})}\mathbf{K}(\mathbf{x})\nabla p = 0, \tag{3.9c}$$

$$s_w + s_o = 1 \tag{3.9d}$$

with the periodic boundary conditions

$$p_L = p_R + \Delta p, \tag{3.9e}$$

$$p_B = p_T, \tag{3.9f}$$

$$(\mathbf{v}_\gamma \cdot \mathbf{n})_L = -(\mathbf{v}_\gamma \cdot \mathbf{n})_R, \tag{3.9g}$$

$$(\mathbf{v}_\gamma \cdot \mathbf{n})_B = -(\mathbf{v}_\gamma \cdot \mathbf{n})_T, \tag{3.9h}$$

where $\gamma = o, w, wp$. The solution of the polymer system depends on the total amount of water ($\bar{s}_w$), oil ($\bar{s}_o$) and polymer ($\bar{c}$) given initially in the system. We have

$$\bar{s}_w = \frac{1}{PV(\Omega)}\int_\Omega \phi s_w dx, \tag{3.9i}$$

$$\bar{s}_o = \frac{1}{PV(\Omega)}\int_\Omega \phi s_o dx, \tag{3.9j}$$

$$\bar{c} = \frac{1}{\bar{s}_w PV(\Omega)}\int_\Omega c s_w \phi dx \tag{3.9k}$$

We have four unknowns: p, s_w, s_o, c. We take for granted that given Δp, $\overline{s_w}$, $\overline{s_o}$ and $\bar{c}$, there exists a solution (p, s_w, s_o, c) to (3.9), and this solution is unique. Let (p, s_w, s_o) be the unique solution of the following problem:

$$\nabla \cdot [k_{ro}(s_o, \mathbf{x})\mathbf{K}\nabla p] = 0, \tag{3.10a}$$

$$\nabla \cdot \left[\frac{k_{rw}(s_w, \mathbf{x})}{R_k(\bar{c}, \mathbf{x})}\mathbf{K}\nabla p\right] = 0 \tag{3.10b}$$

with boundary conditions (3.9e) - (3.9h) and which satisfy (3.9i) - (3.9j). We define $\tilde{k}_{rw} = \frac{k_{rw}}{R_k}$ and rewrite (3.10b) as

$$\nabla \cdot \left[\tilde{k}_{rw}(s_w, \mathbf{x})\mathbf{K}\nabla p\right] = 0 \tag{3.11}$$

We then realize that (3.10a) and (3.11) correspond to the steady state equations for a two-phase problem. The solution (p, s_w, s_o) of such a problem exists and is unique.

We define ($\tilde{p}$, $\tilde{s}_w$, $\tilde{s}_o$, $\tilde{c}$) = (p, s_w, s_o, $\bar{c}$). Let us check that ($\tilde{p}$, $\tilde{s}_w$, $\tilde{s}_o$, $\tilde{c}$) satisfy the polymer equations (3.9). We have

$$\nabla \cdot \left[\frac{k_{ro}(\tilde{s}_o, \mathbf{x})}{\mu_o}\mathbf{K}(\mathbf{x})\nabla\tilde{p}\right] = \frac{1}{\mu_o}\nabla \cdot [k_{ro}(\tilde{s}_o, \mathbf{x})\mathbf{K}(\mathbf{x})\nabla\tilde{p}] = 0$$

from (3.10a) so that (3.9a) is fulfilled. We have

$$\nabla \cdot \left[\frac{k_{rw}(\tilde{s}_w, \mathbf{x})}{\mu_{w,\text{eff}}(\tilde{c})R_k(\tilde{c}, \mathbf{x})}\mathbf{K}(\mathbf{x})\nabla\tilde{p}\right] = \frac{1}{\mu_{w,\text{eff}}(\tilde{c})}\nabla \cdot \left[\frac{k_{rw}(\tilde{s}_w, \mathbf{x})}{R_k(\tilde{c}, \mathbf{x})}\mathbf{K}(\mathbf{x})\nabla\tilde{p}\right]$$
$$= \frac{1}{\mu_{w,\text{eff}}(\tilde{c})}\nabla \cdot \left[\tilde{k}_{rw}(\tilde{s}_w, \mathbf{x})\mathbf{K}(\mathbf{x})\nabla\tilde{p}\right] = 0$$

because $\mu_{w,\text{eff}}$ is constant and from (3.11) so that (3.9b) is fulfilled. Again, since $\tilde{c}$ is constant, we have

$$\nabla \cdot \left[\tilde{c} \frac{k_{rw}(\tilde{s}_w, \mathbf{x})}{\mu_{p,\text{eff}}(\tilde{c}) R_k(\tilde{c}, \mathbf{x})} \mathbf{K}(\mathbf{x}) \nabla \tilde{p} \right] = \frac{\tilde{c}}{\mu_{p,\text{eff}}(\tilde{c})} \nabla \cdot \left[\frac{k_{rw}(\tilde{s}_w, \mathbf{x})}{R_k(\tilde{c}, \mathbf{x})} \mathbf{K}(\mathbf{x}) \nabla \tilde{p} \right] = 0$$

so that (3.9c) is fulfilled. Using again the fact that $\tilde{c}$ is constant, we infer that (3.9g) - (3.9h) are fulfilled.

In conclusion, we see that ($\tilde{p}$, $\tilde{s}_w$, $\tilde{s}_o$, $\tilde{c}$) solve the polymer equations (3.9), and therefore is equal to the unique solution of (3.9), that is, (p, s_w, s_o, c) = ($\tilde{p}$, $\tilde{s}_w$, $\tilde{s}_o$, $\tilde{c}$). In particular, it means that $c = \tilde{c} = \overline{c}$. Therefore, for the solution of the polymer equations at steady state, the concentration distribution is constant in space and equal to $\overline{c}$.

3.3.2 Upscaling Viscosities and the Mixing Parameter

The upscaling of permeability and relative permeability has already been considered, and we now consider upscaling of viscosities and the mixing parameter ω. We also here do flow-based upscaling at steady state. Using that at steady state the polymer distribution will be constant in space, it can be shown that there will be no upscaling effect of the viscosities and ω.

We consider a polymer system where the effect of the permeability reduction factor is not yet included. We let $R_k = 1$, which corresponds to the case where $RRF = 1$ or $C_p^a = 0$. Then the equations governing polymer flow at steady state are the same as (3.9) except that the R_k-factor is not present:

$$\nabla \cdot \mathbf{v}_o = 0, \qquad \mathbf{v}_o = \frac{k_{ro}(s_o, \mathbf{x})}{\mu_o} \mathbf{K}(\mathbf{x}) \nabla p, \tag{3.12a}$$

$$\nabla \cdot \mathbf{v}_w = 0, \qquad \mathbf{v}_w = \frac{k_{rw}(s_w, \mathbf{x})}{\mu_{w,\text{eff}}(c)} \mathbf{K}(\mathbf{x}) \nabla p, \tag{3.12b}$$

$$\nabla \cdot c\mathbf{v}_{wp} = 0, \qquad \mathbf{v}_{wp} = \frac{k_{rw}(s_w, \mathbf{x})}{\mu_{p,\text{eff}}(c)} \mathbf{K}(\mathbf{x}) \nabla p. \tag{3.12c}$$

The boundary and initial conditions are still given as (3.9e) - (3.9k). An expression for upscaled effective water viscosity can be found from the flux in Equation (3.12b) when the pressure gradient is set up in β-direction:

$$\mu^*_{w,\text{eff},\beta}(\overline{c}) = -\frac{k^*_{rw,\beta} K^*_{\beta\beta} \Delta p_\beta}{v^*_{w,\beta\beta} L_\beta},$$

where $v^*_{w,\beta\beta}$ is set, as before, as

$$v^*_{w,\beta\beta} = \frac{1}{A_\beta} \int_{\Gamma_\beta} \mathbf{v}_{w,\beta} \cdot \mathbf{e}_\beta \, ds = -\frac{1}{A_\beta} \int_{\Gamma_\beta} \frac{k_{rw}}{\mu_{w,\text{eff}}} \mathbf{K} \nabla p_\beta \cdot \mathbf{e}_\beta \, ds. \tag{3.13}$$

We have shown that c is constant, and therefore the equations (3.12a) - (3.12c) reduce to the two-phase steady-state equations as the viscosity terms can be eliminated. The same holds for the boundary conditions. This means that s_w, s_o, and p_β solve both the two-phase and polymer equations when $R_k = 1$, which implies that

$$k^*_{rw,\beta}(s^*_w) = \frac{L_\beta}{K^*_{\beta\beta} A_\beta \Delta p_\beta} \int_{\Gamma_\beta} k_{rw} \mathbf{K} \nabla p_\beta \cdot \mathbf{e}_\beta \, ds$$

as in (3.8), but when now p_β is also the solution of the polymer equations (3.12a) - (3.12c) with boundary and initial conditions (3.9e) - (3.9k).

The upscaled relative permeability $k^*_{rw,\beta}$ is found from (3.8) and $K^*_{\beta\beta}$ is found from (3.3).

The expressions for $k^*_{rw,\beta}$ and $v^*_{w,\beta\beta}$ can be inserted:

$$\mu^*_{w,\text{eff},\beta}(\overline{c}) = -\frac{K^*_{\beta\beta}\Delta p_\beta L_\beta \int_{\Gamma_\beta} k_{rw}\mathbf{K}\nabla p_\beta \cdot \mathbf{e}_\beta \, ds}{L_\beta K^*_{\beta\beta} A_\beta \Delta p_\beta \left(-\frac{1}{A_\beta}\int_{\Gamma_\beta} \frac{k_{rw}}{\mu_{w,\text{eff}}}\mathbf{K}\nabla p_\beta \cdot \mathbf{e}_\beta \, ds\right)}.$$

Hence,

$$\mu^*_{w,\text{eff},\beta} = \frac{\int_{\Gamma_\beta} k_{rw}\mathbf{K}\nabla p_\beta \cdot \mathbf{e}_\beta \, ds}{\int_{\Gamma_\beta} \frac{k_{rw}}{\mu_{w,\text{eff}}(c)}\mathbf{K}\nabla p_\beta \cdot \mathbf{e}_\beta \, ds}.$$

Since we know that $c = \bar{c}$ is constant in space, $\mu_{w,\text{eff}}$ can be moved outside the integral and we get

$$\mu^*_{w,\text{eff}} = \mu_{w,\text{eff}}.$$

Upscaled effective water viscosity equals small scale effective water viscosity. The same arguments can be made for the effective polymer viscosity to show that $\mu^*_{p,\text{eff}} = \mu_{p,\text{eff}}$. Since there is no upscaling effect of viscosities, there is no upscaling effect of ω and μ_m, that is $\omega^* = \omega$ and $\mu^*_m = \mu_m$

3.3.3 Upscaling Permeability Reduction Factor: R_k

The permeability reduction factor R_k is contained in the total water flux and in the polymer flux. We perform flow-based upscaling where the equations for flux are used to obtain an upscaled value of R_k. An expression for upscaled R_k can be found from the expression for the water flux in a polymer flow system when the pressure gradient is set up in the β-direction:

$$R^*_{k,\beta} = -\frac{k^*_{rw,\beta}K^*_{\beta\beta}\Delta p_\beta}{\mu_{w,\text{eff}}L_\beta v^*_{w,\beta\beta}}, \tag{3.14}$$

where $k^*_{rw,\beta}$ is the upscaled relative permeability of water obtained from two-phase upscaling, $K^*_{\beta\beta}$ is upscaled absolute permeability in β-direction obtained from a single-phase simulation with pressure gradient in β-direction. The effective water viscosity is $\mu_{w,\text{eff}}$, which has no upscaling effect. The upscaled flux $v^*_{w,\beta\beta}$ is:

$$v^*_{w,\beta\beta} = \frac{1}{A_\beta}\int_{\Gamma_\beta} \mathbf{v}_{w,\beta} \cdot \mathbf{e}_\beta \, ds = -\frac{1}{A_\beta}\int_{\Gamma_\beta} \frac{k_{rw}}{\mu_{w,\text{eff}}R_k}\mathbf{K}\nabla p_\beta \cdot \mathbf{e}_\beta \, ds.$$

3.3.4 Upscaling C^a_p and RRF

The definition of R_k is given in Equation (2.2), and it includes the parameters RRF, C^a_p and $C^{a,max}_p$, which also need to be upscaled. As $C^a_p(c_{\max}) = C^{a,max}_p$, we also have that $C^{a\,*}_p(c_{\max}) = C^{a,max\,*}_p$, so that upscaled $C^{a,max}_p$ can be found from upscaled C^a_p. Thus we only need to upscale RRF and C^a_p.

The amount of adsorbed polymer is upscaled using volume averaging:

$$C^{a*}_p(c) = \frac{\int_\Omega \rho_r(1-\phi)C^a_p(c) \, dx}{\int_\Omega \rho_r(1-\phi) \, dx}.$$

As C_p^a is a function of concentration, the amount of adsorbed polymer must be upscaled for different concentrations to obtain an upscaled C_p^a curve versus concentration.

Upscaled R_k is found from flow-based steady-state upscaling, and is used to find upscaled RRF values. From looking at the definition of R_k in Equation (2.2) we see that when plotting R_k versus C_p^a, this should produce a straight line:

$$R_k(c) = a\, C_p^a(c) + 1,$$

which is the formula of a straight line where a is the slope of the line, which in this case is:

$$a = \frac{RRF - 1}{C_p^{a,max}}\ .$$

We upscale RRF by using the slope of upscaled $R_{k\beta}$ for direction β versus upscaled C_p^a:

$$R_{k\beta}^*(c) = a_\beta^*\, C_p^{a\,*} + 1,$$

where the slope is:

$$a_\beta^* = \frac{RRF_\beta^* - 1}{C_p^{a,max\,*}}\ .$$

Hence, RRF_β^* can then be found from solving

$$RRF_\beta^* = a_\beta^* C_p^{a,max\,*} + 1.$$

3.4 Summary

In this chapter the upscaling procedures for single-, two-phase, and polymer flow has been presented. Absolute permeability is upscaled using the flow-based technique, while porosity is upscaled using volume averaging. Relative permeabilities are upscaled by solving the two-phase system until steady state is reached and then using the flow-based technique to upscale. We saw that for polymer flow the concentration distribution at steady state will be uniform, and that there will be no upscaling effect of viscosities and the mixing parameter ω. The permeability reduction factor R_k is upscaled by solving a system with polymer flow until steady state is reached and then performing flow-based upscaling. The amount of adsorbed polymer C_p^a is upscaled by volume averaging, and from $C_p^{a\,*}(c_{\max})$ we find $C_p^{a,max\,*}$. Upscaled RRF values are found from the slope of R_k^* versus $C_p^{a\,*}$.

Chapter 4

Numerical Results

A polymer flow solver developed by SINTEF has been used. This is a part of the open source MATLAB Reservoir Simulation Toolbox (MRST) [11]. MRST is also used for handling grids and for plotting. The polymer solver solves (2.3) - (2.5), with valid initial and boundary conditions that must be given, using implicit Euler and Newton's method.

A steady-state solver is made, which runs a dynamic simulation of the system until a steady state is reached, and then single-phase, two-phase, and polymer upscaling is performed. The parameters that are upscaled are K, k_r, R_k, C_p^a, and RRF. In the previous chapter it was shown that there should not be an upscaling effect of viscosities and ω, and this is also verified by upscaling the viscosities and ω numerically.

In the following chapter, the results obtained from numerical upscaling of four different grids are presented.

4.1 Program Structure

Before solving and upscaling, the system must be set up. A grid with belonging properties must be provided, and fluid properties and initial conditions must be given. Boundary conditions must be chosen, and here we use periodic boundary conditions with a pressure gradient set up in one direction, as described in Section 3.1.

First, the single-phase problem is solved, and from that upscaled absolute permeability is obtained. The single-phase problem only has to be solved once due to the assumption of incompressibility and no time dependence in the equations. Next, the two-phase problem is solved until steady state, and then upscaling of relative permeabilities is performed. The two-phase problem must be solved until steady state for different saturations to obtain upscaled permeabilities for different saturations. Then, the polymer equations are solved, and also they are solved until the system reaches steady state. The solution can be used to obtained upscaled parameters, such as R_k^*. For both two-phase and polymer upscaling an upscaled saturation value is found from the saturation distribution at steady state using volume averaging. Upscaled C_p^a values are found from volume averaging, and upscaled RRF values are found from the slope of upscaled R_k values versus upscaled C_p^a values.

The rock and fluids are assigned parameters based on realistic models. An absolute permeability is given for each cell and for each direction, and is in some cases isotropic. Relative permeability

curves are given for each type of rock, and are given as tabulated values for different saturations. The amount of adsorbed polymer is given as tabulated values for different concentrations, and a C_p^a curve is given for each type of rock. A value for the residual resistance factor and for the maximum possible adsorbed polymer is given for each type of rock, and these are constant values in a rock type. The inaccessible pore space is currently set to be zero, and gravity and capillary forces are neglected. The mixing parameter is set to be 1 for all simulations.

Steady state is found by running a dynamic simulation until the system reaches steady state. The steady-state solver is implemented so that for each time step the solution obtained is compared with the solution of the previous time step. If these two solutions are equal enough, *i.e.*, the change is below a set tolerance, it is said that steady state is reached. The variables checked for change are saturation, concentration, and pressure.

4.2 Verification of Code

It is important to verify that the code is working correctly and gives reliable results. The best way to do this is to run the code for a system that can be solved analytically, and then compare the results. We will here look at a simple system where upscaled R_k values can be found (semi) analytically, and compare the analytically obtained upscaled values with the values obtained when upscaling purely numerically.

We consider a simple system consisting of two cells with one type of rock in each cell. Both rocks have equal permeability and porosity. The system is illustrated in Figure 4.1. A pressure gradient is set up in the x-direction to drive the flow.

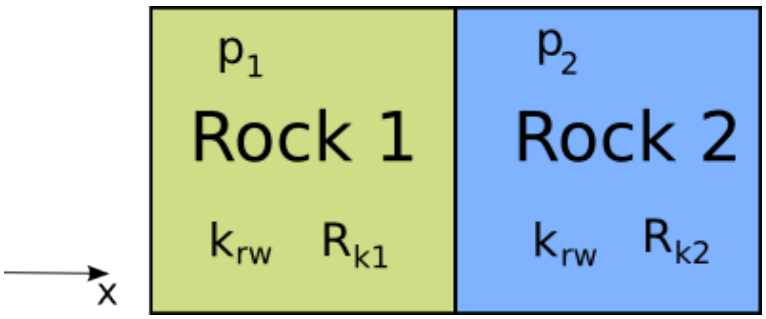

Figure 4.1: *Illustration of a simple domain containing two cells with Rock 1 and Rock 2.*

We consider the solution in the x-direction of a two-phase problem in this domain with gravity and capillary forces neglected, and where the phases are water and oil. The equations governing the water and oil phase in this system in the x-direction at steady state are:

$$\frac{\partial}{\partial x}\left(\frac{Kk_{rwe}(s_w,x)}{\mu_w}\frac{\partial p}{\partial x}\right)=0,$$
$$\frac{\partial}{\partial x}\left(\frac{Kk_{ro}(s_w)}{\mu_o}\frac{\partial p}{\partial x}\right)=0.$$

Here, μ is constant in x for both phases, and as we also set K to be the same in both rocks, both μ

and K can be eliminated from the equations:

$$\frac{\partial}{\partial x}\left(k_{rwe}(s_w, x)\frac{\partial p}{\partial x}\right) = 0,$$
$$\frac{\partial}{\partial x}\left(k_{ro}(s_w)\frac{\partial p}{\partial x}\right) = 0.$$

We define k_{rwe} to be a so-called effective relative permeability of the water phase, which is defined as the relative permeability k_{rw} of water divided by a permeability reduction factor R_k:

$$k_{rwe} = \frac{k_{rw}(s_w)}{R_k(x, c)}. \tag{4.1}$$

The relative permeability k_{rw} is equal in the two rocks, but the rocks have different permeability reduction factors. The concentration c is constant in the domain. The effective relative permeabilties of Rock 1 and Rock 2 are, respectively:

$$k^1_{rwe} = \frac{k_{rw}(s_w)}{R_{k1}(c, x)},$$
$$k^2_{rwe} = \frac{k_{rw}(s_w)}{R_{k2}(c, x)}.$$

The water flux in the x-direction is defined as

$$v_w = k_{rwe}(s, x)\frac{\partial p}{\partial x},$$

and it must be continuous in the x-direction, giving:

$$k^1_{rwe}(s_{w1})\frac{\Delta p_1}{x_1} = k^2_{rwe}(s_{w2})\frac{\Delta p_2}{x_2}. \tag{4.2}$$

Here, Δp_1 is the pressure difference over Rock 1, while Δp_2 is the pressure difference over Rock 2. The saturations in the two rocks are s_{w1} and s_{w2}. The lengths of Rock 1 and Rock 2 are x_1 and x_2, respectively. In this case, the two rocks have the same length, so that $x_1 = x_2$, and Equation (4.2) can be written:

$$k^1_{rwe}(s_{w1})\Delta p_1 = k^2_{rwe}(s_{w2})\Delta p_2 \tag{4.3}$$

The oil flux must also be continuous, and this gives the following equation:

$$k_{ro}(s_{w1})\Delta p_1 = k_{ro}(s_{w2})\Delta p_2. \tag{4.4}$$

The relative permeability of oil is equal in the two rocks, and it is not affected by the permeability reduction factor. The two rocks are of equal size and have the same porosity, and therefore the average saturation, or upscaled saturation, in the domain is

$$s^*_w = \frac{s_{w1} + s_{w2}}{2}\ . \tag{4.5}$$

We also have that the total pressure difference over the domain in the x-direction equals the pressure difference over Rock 1 plus the pressure difference over Rock 2:

$$\Delta p = \Delta p_1 + \Delta p_2.$$

If we use that $s_{w2} = 2s_w^* - s_{w1}$ from Equation (4.5), and that $\Delta p_2 = \Delta p - \Delta p_1$, Equation (4.3) and Equation (4.4) can be written:

$$k_{rwe}^1(s_{w1})\Delta p_1 = k_{rwe}^2(2s_w^* - s_{w1})(\Delta p - \Delta p_1) \tag{4.6}$$

$$k_{ro}(s_{w1})\Delta p_1 = k_{ro}(2s_w^* - s_{w1})(\Delta p - \Delta p_1) \tag{4.7}$$

If we divide (4.6) by (4.7) we obtain the following equation:

$$\frac{k_{rwe1}(s_{w1})}{k_{ro}(s_{w1})} = \frac{k_{rwe2}(2\bar{s}_w - s_{w1})}{k_{ro}(2\bar{s}_w - s_{w1})},$$

and after rearranging, this gives

$$k_{rwe1}(s_{w1})k_{ro}(2\bar{s}_w - s_{w1}) - k_{ro}(s_{w1})k_{rwe2}(2\bar{s}_w - s_{w1}) = 0. \tag{4.8}$$

We now have one equation with one unknown, and this equation can be solved for s_{w1} using a computer, as long as values for s_w^*, k_{rw}, k_{ro}, c, and R_k are given. When the solution s_{w1} is obtained, s_{w2} can also be obtained, and from that $k_{rwe}^1(s_{w1})$ and $k_{rwe}^2(s_{w2})$ can be found. We want to use this solution to obtain upscaled values for k_{rwe}, and then further obtain upscaled values for R_k. Since k_{rw} is the same in the two rocks, the upscaled k_{rw} values equals the small-scale values: $k_{rw}^*(s_w^*) = k_{rw}(s_w^*)$. In the x-directions the two rocks are laying in series, and in that case upscaled effective relative permeability values equals the harmonic mean:

$$k_{rwe}^* = 2\left(\frac{1}{k_{rwe}^1(s_{w1})} + \frac{1}{k_{rwe}^2(s_{w2})}\right)^{-1} \tag{4.9}$$

The upscaled R_k values can be found from Equation 4.1 using k_{rw} and upscaled k_{rwe}:

$$R_k^* = \frac{k_{rw}}{k_{rwe}^*} \tag{4.10}$$

Thus, shortly explained, we can find an upscaled value for R_k in the x-direction by solving Equation (4.8) for s_{w1} for given s_w^*, k_{rw}, k_{ro}, c, and R_k values. When s_{w1} and s_{w2} are obtained, the saturations can be used to find k_{rwe}^* from Equation (4.9). And then, at last, an upscaled R_k value is found from Equation (4.10).

Table 4.1: *Example of set of values on small-scale and the corresponding upscaled values. Numbers in bold are numbers obtained from solving and upscaling, whereas the others are values given initially. The results from analytical and numerical upscaling are equal.*

	s_w	c	$k_{rw}(s_w^*)$	$k_{rwe}(s_w)$	R_k
Rock 1	**0.4666**	4	0.29	0.17	1.4
Rock 2	**0.5334**	4	0.29	0.11	3.2
Upscaled analytically	0.5	4	0.29	**0.133**	**2.179**
Upscaled numerically	0.5	4	0.29	**0.133**	**2.179**

We upscale R_k for different saturations using this method, and different saturations produce different upscaled R_k values. We compare these analytically obtained values with values that are obtained from using the polymer solver and upscaling numerically. We compare both the saturation distribution at steady state and the upscaled values obtained, and the results from the analytical method are in agreement with the results obtained numerically.

The values obtained from solving and upscaling with $s_w^* = 0.5$ are given in Table 4.1. The values in bold in the table are values that are found from solving and upscaling, while the others are values that must be given initially. See that the same upscaled values are obtained from the analytical and numerical method.

4.3 Upscaling of Simple Layered Case

We first consider the upscaling if the simple Cartesian layered grid illustrated in Figure 4.2, which consists of two types of rock that are layered. The blue layer in the middle of the domain will be referred to as Rock 1, whereas the red represents Rock 2. Rock 1 has a permeability of 0.1 mD, while the permeability of Rock 2 is 100mD. The porosity is set to 0.1 in both rocks. The residual resistance factor is 1.4 in Rock 1, and 3.2 in Rock 2.

For this grid we upscale $\mathbf{K}$, k_r, R_k, and RRF. Preliminary we let C_p^a be the same in both rocks so that upscaled C_p^a equals small-scale C_p^a.

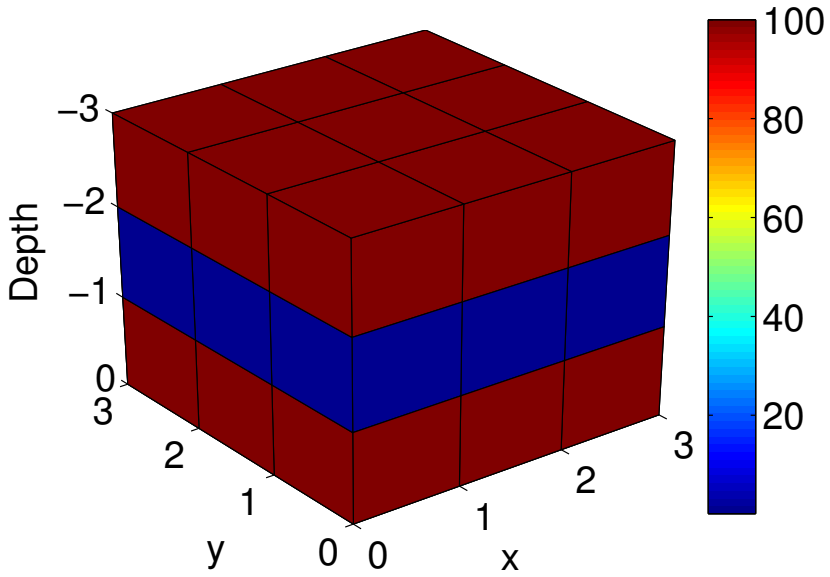

Figure 4.2: *Illustration of the simple layered grid. Colorbar shows permeability in mD, which is 0.1 mD for the blue rock (Rock 1), and 100 mD for the red rock (Rock 2). The porosity is 0.1 everywhere. The grid consists of 27 cells.*

4.3.1 Single- and Two-Phase Upscaling

For a simple case like this, upscaled permeability $\mathbf{K}^*$ can be calculated analytically. The x- and y-directions are symmetric, and thus we expect to get the same upscaled permeability in those directions. One may say that in the x- and y-directions the rocks are laying in parallel, and then upscaled permeability is given as the volume-weighted arithmetic average:

$$K_{xx}^* = K_{yy}^* = \frac{(2 \cdot 100 + 1 \cdot 0.1)}{3} = 66.7\text{mD}. \tag{4.11}$$

In the z-direction the rocks are laying in series, and then upscaled permeability is given as the volume-weighted harmonic average:

$$K^*_{zz} = 3\left(\frac{2}{100} + \frac{1}{0.1}\right)^{-1} = 0.299\text{mD}. \tag{4.12}$$

Upscaled $\mathbf{K}$ is found numerically from solving the single-phase equation with a pressure difference of 1 bar set up over the domain in direction β, and then obtaining $\mathbf{K}^*_\beta$ as described in Section 3.1 and from Equation (3.2). For this simple layered grid we obtain:

$$\mathbf{K}^* = \begin{pmatrix} 66.7 & 0 & 0 \\ 0 & 66.7 & 0 \\ 0 & 0 & 0.2994 \end{pmatrix} \text{mD},$$

which is in agreement with the analytical results.

Relative permeabilities are upscaled using steady state and the flow-based technique as described in Section 3.2. The relative permeabilities are only upscaled for saturations for which the small-scale relative permeabilities of the different rocks are defined. Initially the saturation distribution is set up to be uniform, and a pressure difference of 1 bar is set up over the domain. Upscaled water and oil relative permeabilities for direction β are found from Equations (3.6) and (3.7), respectively, and are plotted as functions of saturations together with the small-scale k_{rw} and k_{ro} values in Figure 4.3.

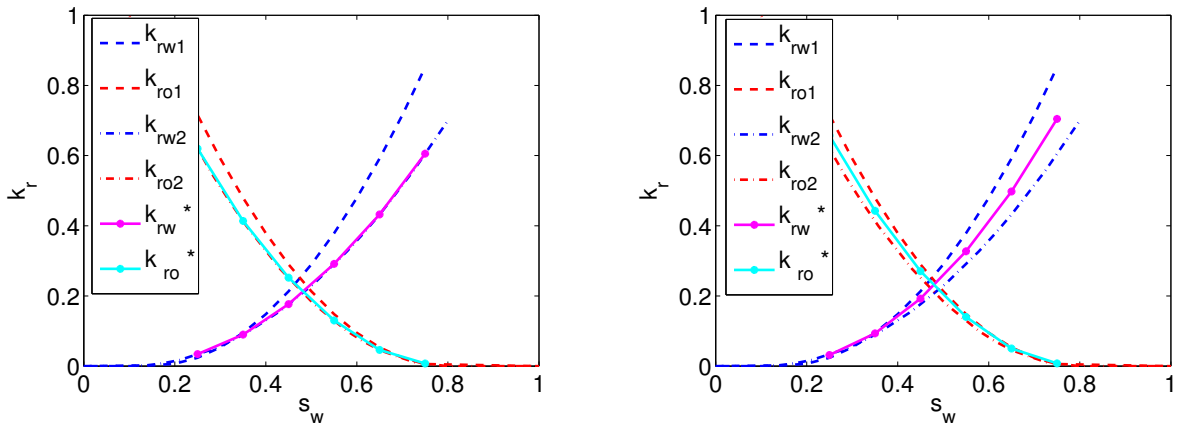

(a) *Upscaled relative permeabilities in the x- and y-directions plotted together with the small-scale relative permeabilities.*

(b) *Upscaled relative permeabilities in the z-direction plotted together with the small-scale relative permeabilities.*

Figure 4.3: *Upscaled relative permeabilities plotted together with small-scale relative permeabilities. Small-scale values are plotted with dashed lines, whereas upscaled values are plotted with solid lines. The upscaled relative permeabilities are equal in the x- and y-directions because of symmetry.*

Upscaled relative permeabilities for the x- and y-directions are plotted together with the small-scale relative permeability curves in Figure 4.3a. Because of the symmetry in the x- and y-directions, the upscaled relative permeabilities are equal in these two directions. They are very close to the small-scale relative permeability values of Rock 2 (top and bottom layer in grid), and this is believed to be caused by the fact that Rock 2 has a much higher permeability than Rock 1, which leads to

most of the flow being through Rock 2. The upscaled relative permeabilities are mostly influenced by the relative permeabilities of the rock with the most flow, which is Rock 2 in this case. In the z-direction, the upscaled permeabilities are approximately in the middle of the small-scale relative permeabilities, and k^*_{rz} is plotted together with small-scale relative permeabilities in Figure 4.3b. With the pressure gradient set up in the z-direction and the main flow being in that direction, the flow needs to go through both Rock 1 and Rock 2, and therefore one may say that the properties of both rocks will influence the upscaled relative permeabilities.

The solution at steady state for the pressure gradient set up in either x- or y-direction is a constant saturation distribution. This is because the system is set up initially with a uniform saturation distribution, and with the flow being in the x- and y-direction there is nothing disturbing this uniform distribution as the flow is along the rock layers. The fluids will not prefer to be in one rock rather than the other because they will not notice the other rock when the flow is along the layers and not across. In the z-direction, the saturation is not constant in space as the flow goes through both layers and the fluids get to choose their preferred rock to be in.

4.3.2 Polymer Upscaling

c	C_p^a
0	0
0.25	0.00001
0.5	0.000013
0.75	0.000015
1.0	0.000017
1.25	0.000018
1.5	0.000019
2.0	0.000023
2.75	0.000025
3.0	0.000025
4.0	0.000025

Table 4.2: *Values for C_p^a for different concentrations given in input file.*

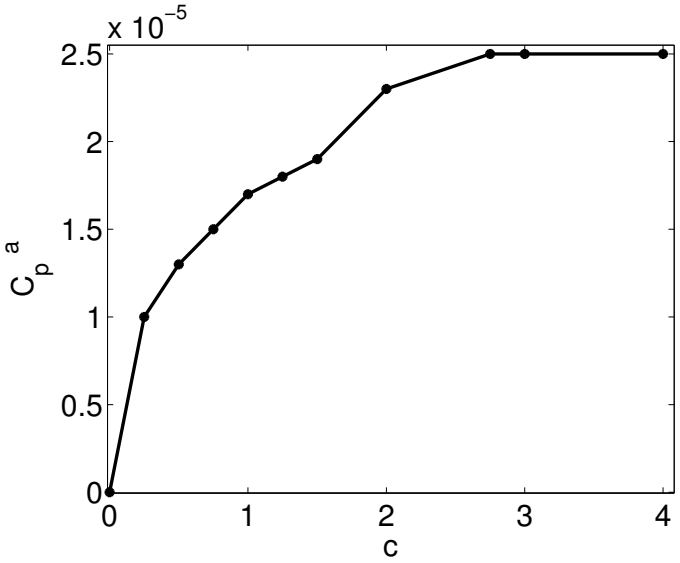

Figure 4.4: *Plot of the amount of adsorbed polymer C_p^a versus concentration of polymer, values given in Table 4.2 .*

After performing single- and two-phase upscaling, we now consider polymer upscaling. Here, the two rocks are assigned different residual resistance factors, and thus have different permeability reduction factors. The amount of adsorbed polymer depends on the polymer concentration, and tabulated values are provided for different concentrations. The values are shown in Table 4.2 and plotted in Figure 4.4. The initial conditions are uniform saturation and concentration in space. The pressure difference over the domain is set to be 1 bar.

The permeability reduction factor R_k is upscaled as described in Section 3.3.3 using Equation (3.14). It is upscaled for different saturations, but only for saturations for which the small-scale relative permeabilities are defined. Upscaled permeability reduction factor values are obtained for each direction, and Figure 4.5a shows R^*_{kx}, R^*_{ky} and R^*_{kz} for a water saturation of 0.5. Analogous to what we saw for upscaled relative permeabilities, the upscaled R_k values for the x- and y-directions

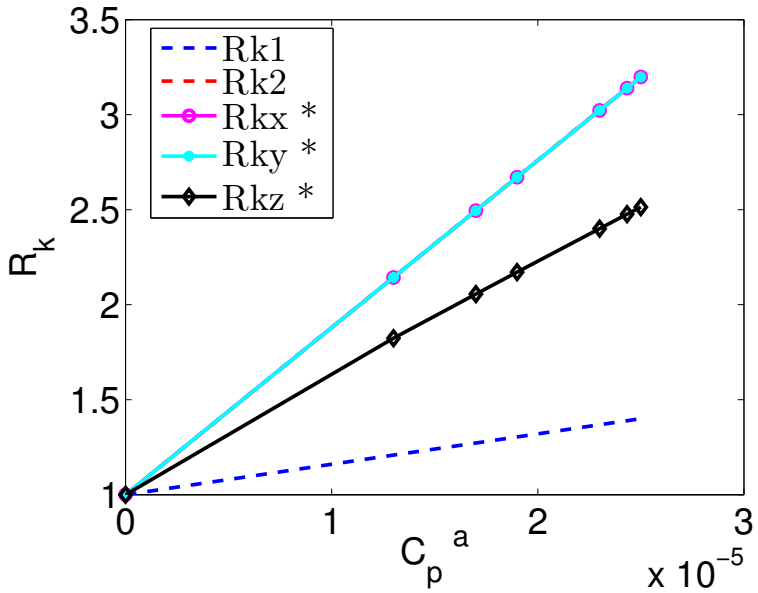

(a) *Upscaled R_{kx}, R_{ky}, R_{kz} values for $s_w = 0.25$ plotted together with the small-scale values.*

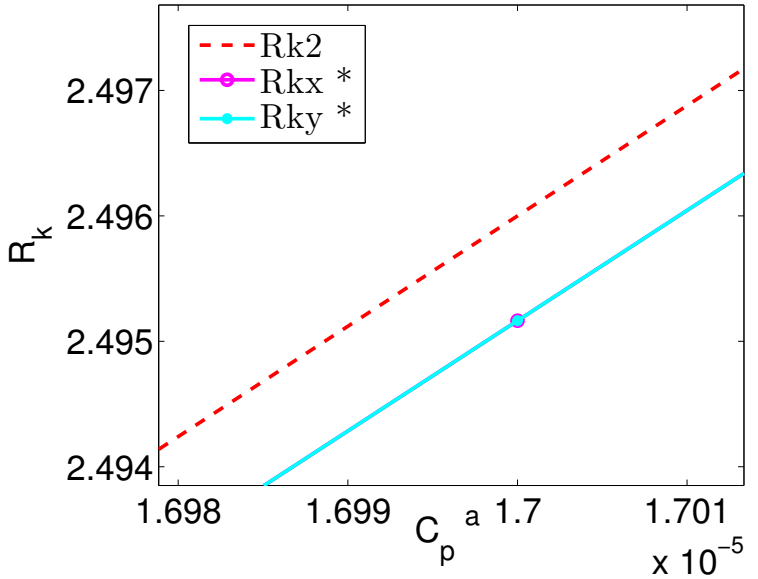

(b) *Close-up of Figure 4.5a to get a closer look at R^*_{kx}, R^*_{ky}, and R_{k2}.*

Figure 4.5: *Plots of upscaled R_k values for the different directions for $s_w = 0.25$. For the x- and y-directions R^*_k are equal, and very close to R_{k2}. In the close-up we see that the upscaled R_k values for the x- and y-directions are just below the R_{k2} values.*

are equal and close to the small-scale values of Rock 2. For the z-direction, the upscaled R_k values are approximately in the middle between the small-scale values of Rock 1 and Rock 2. Figure 4.5b shows a close-up of R^*_{kx}, R^*_{ky}, and R_{k2}, and we see that R^*_{kx} and R^*_{ky} are just below R_{k2}. So the upscaled values are in the range of the small-scale values.

Upscaled R_k values for the z-direction for different saturations are plotted in Figure 4.6a along

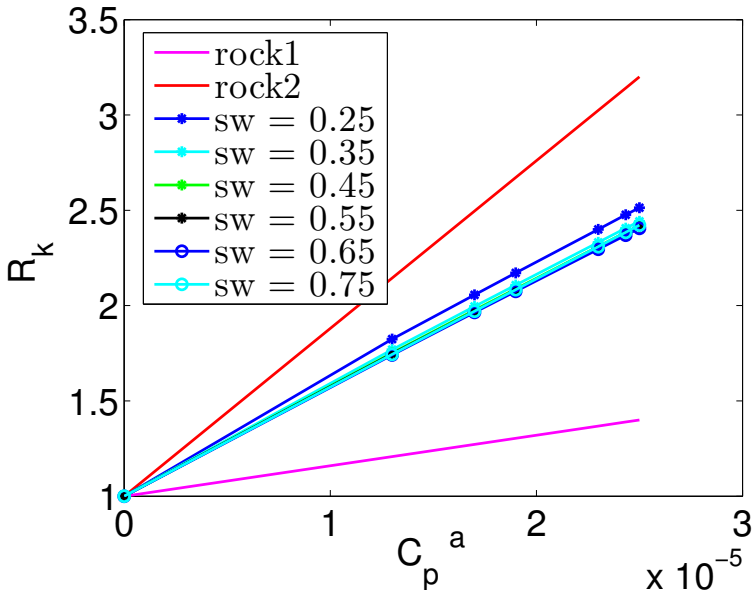

(a) Upscaled R_k for the z-direction.

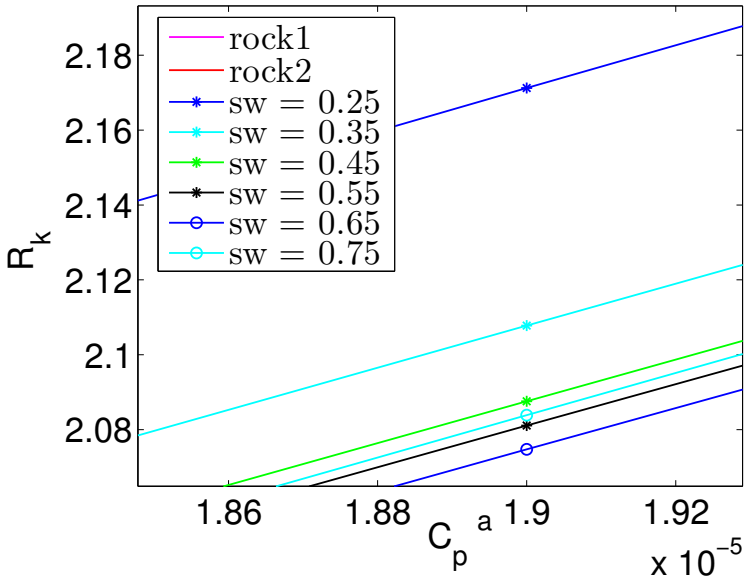

(b) Close-up of R^*_{kz} for various saturations from Figure 4.6a. No obvious pattern in the R_k dependence on saturation.

Figure 4.6: *Plots of upscaled R_k values for the z-direction for different saturations. Pink and red line are for Rock 1 and Rock 2, while the other lines represent upscaled R_k values for the saturations given in the legend. The upscaled values depend on saturation, but the dependence does not seem to be strong.*

with the small-scale R_k values of the two rocks. We see that R^*_{kz} depends on saturation, but the dependence does not seem to be strong. Figure 4.6b shows a close-up of R^*_{kz}, and there is not an obvious pattern in the dependence on saturation. It almost appears as increasing saturation decreases R^*_k, but R^*_k for $s_w = 0.75$ does not follow this trend.

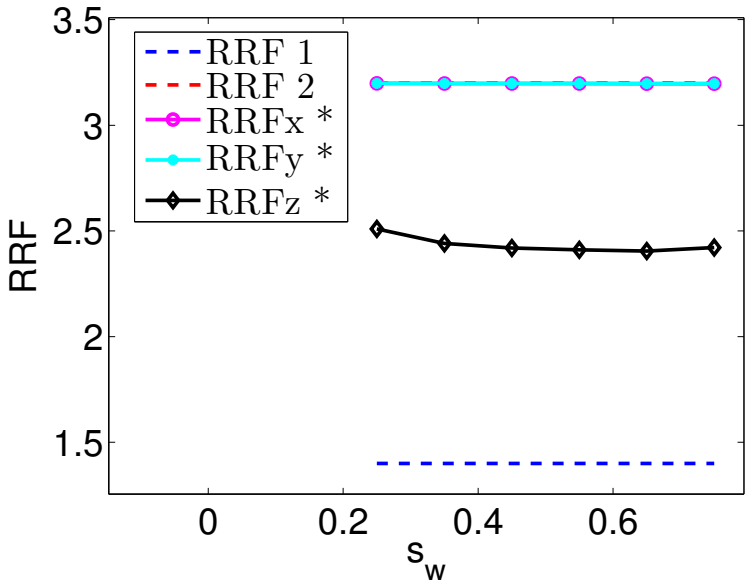

(a) *Upscaled RRF values plotted against saturation for all directions together with the small-scale RRF values.*

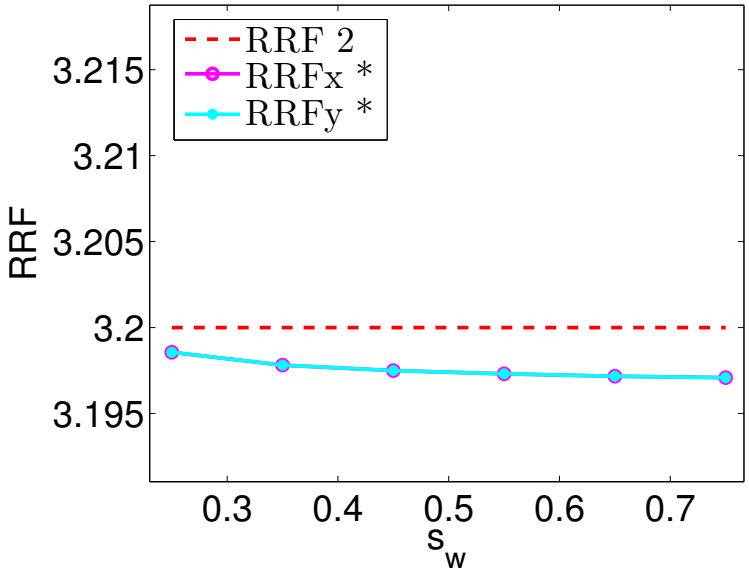

(b) *Section of Figure 4.7a, which shows a close-up of RRF_x^*, RRF_y^* and RRF_2.*

Figure 4.7: *Plot of upscaled RRF values as functions of saturation. The saturation dependence appears to be weak. The upscaled RRF values for the x- and y-directions are equal and very close to the RRF of Rock 2.*

The residual resistance factor RRF is upscaled as described in Section 3.3.4. Plotting the R_k^* values versus the C_p^{a*} values produces almost straight lines, and RRF^* is found from the slopes of the lines. As R_k^* has different slopes for different saturations, RRF will also depend on saturation, and as R_k^* depends on direction, so will RRF^*. Figure 4.7a shows upscaled RRF for the three

different directions for different saturations together with the small-scale values of RRF. We see that RRF_x^* and RRF_y^* are almost equal to the RRF of Rock 2. The close-up in Figure 4.7b shows that $RRF_x^* = RRF_y^*$, and that the values are just smaller than the RRF of Rock 2. Though the upscaled RRF values depend on saturation, the dependence seems to be weak. The upscaled RRF values obtained are given in Table 4.3.

Table 4.3: *Values obtained from upscaling RRF for the simple layered grid where the two rocks have the same C_p^a values. The same values are obtained for the x- and y-directions due to symmetry.*

s_w	RRF_x^*	RRF_y^*	RRF_z^*
0.25	3.1986	3.1986	2.5096
0.35	3.1978	3.1978	2.4408
0.45	3.1975	3.1975	2.4194
0.55	3.1973	3.1973	2.4110
0.65	3.1972	3.1972	2.4047
0.75	3.1971	3.1971	2.4214
mean	3.1976	3.1976	2.4345

4.3.3 Polymer Upscaling with Different C_p^a in the Two Rocks

We now look at upscaling of the same grid as in the previous section, the simple layered grid in Figure 4.2, but now with the two rocks having different C_p^a values. This is to see how the upscaling of C_p^a will affect the results obtained in the previous section. The amount of adsorbed polymer C_p^a is upscaled using volume averaging as described in Section 3.3.4. Table 4.4 shows the small-scale and the upscaled values of C_p^a, and these are plotted in Figure 4.8.

Table 4.4: *Small-scale C_p^a values for the two rocks and upscaled C_p^a values obtained using volume averaging.*

c	C_{p1}^a	C_{p2}^a	$C_p^{a\,*}$
0	0	0	0
0.25	0.00001	0.000015	0.000013
0.5	0.000013	0.000018	0.000016
0.75	0.000015	0.000020	0.000018
1.0	0.000017	0.000023	0.000021
1.25	0.000018	0.000025	0.000023
1.5	0.000019	0.000027	0.000024
2.0	0.000023	0.000028	0.000026
2.75	0.000025	0.000030	0.000028
3.0	0.000025	0.000030	0.000028
4.0	0.000025	0.000030	0.000028

The fact that C_p^a is different in the two rocks and needs to be uspcaled affects the upscaled R_k values. Figure 4.9 shows upscaled R_k values plotted together with small-scale R_k values for Rock 1 and Rock 2 for a water saturation of 0.25. We see that the R_{kx}^* and R_{ky}^* values are not in the range of the small-scale values of Rock 1 and Rock 2. One would expect the values of Rock 1 and Rock 2 to act as lower and upper bounds for the upscaled R_k values, but this is not the case here. As the upscaled values were in the range of the small-scale values when C_p^a was the same in the two rocks,

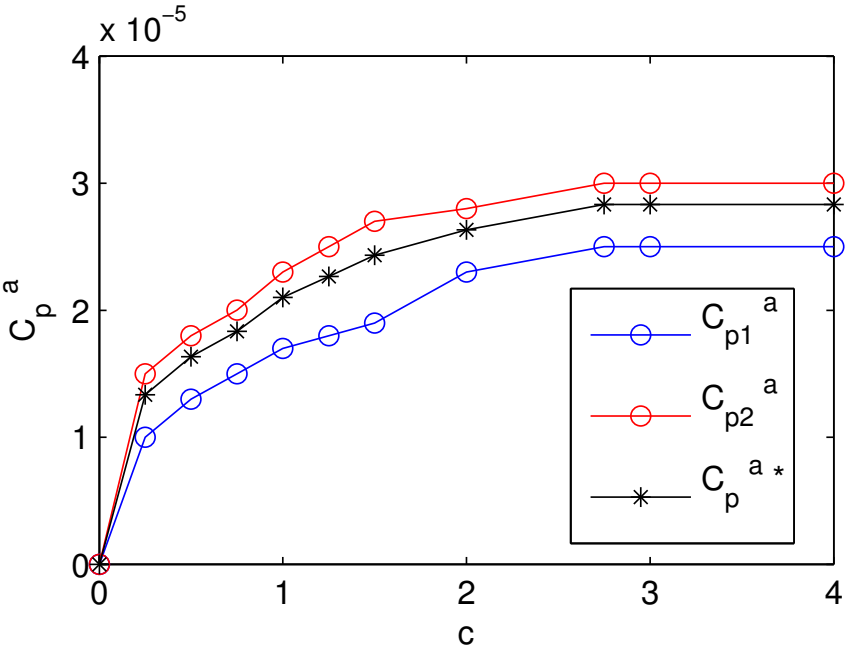

Figure 4.8: *Small-scale C_p^a values for the two rocks plotted together with upscaled C_p^a values found from volume averaging. The black line represents upscaled C_p^a values.*

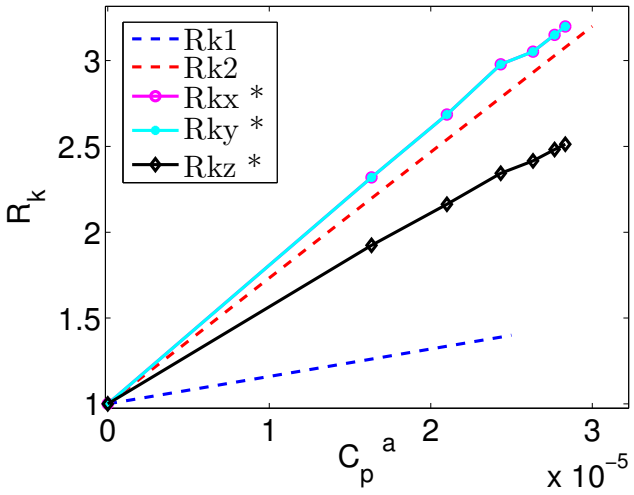

Figure 4.9: *Upscaled R_k values for the x-, y-, and z-directions for $s_w = 0.25$. For the x- and y-directions the upscaled values are outside the range of the small-scale values, and this we believe to be caused by the upscaling of C_p^a.*

we believe it to be an effect caused by the upscaling of C_p^a. This could perhaps be an indication of that using volume averaging to upscale C_p^a is not the best method.

We already know that most of the flow goes through Rock 2 since it is a lot more permeable than Rock 1, and one might therefore think that more correct upscaled C_p^a values should be closer to the C_p^a values of Rock 2 than what is obtained using volume averaging. For the upscaling of relative permeabilities and the permeability reduction factor we also saw that indeed the upscaled values for the x- and y-directions were almost equal to the values of Rock 2. The closer the upscaled C_p^a values are to the C_p^a values of Rock 2, the more likely the R_{kx}^* and R_{ky}^* curves as functions of $C_p^{a\,*}$ are to lie below the R_{k2} curve as a function of $C_{p\,2}^a$. In the next section we therefore consider some other

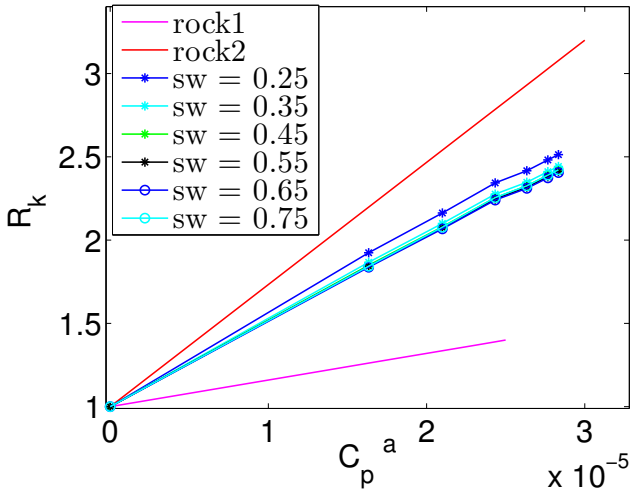

Figure 4.10: *Upscaled R_k values for the z-direction. Pink and red lines are for Rock 1 and Rock 2, while the other lines are upscaled R_k values for the saturations given in legend.*

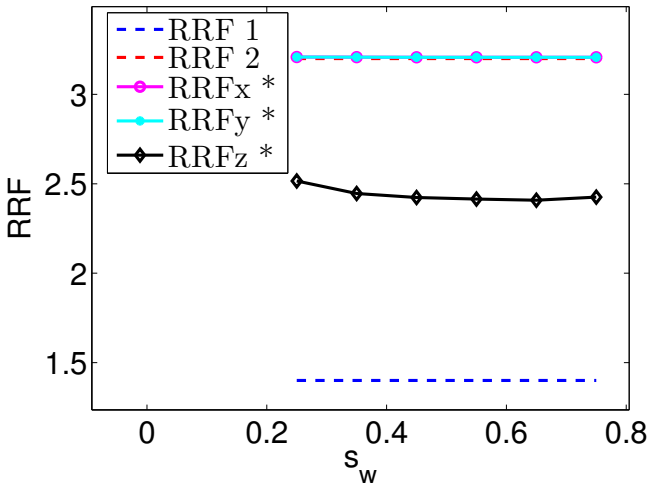

Figure 4.11: *Upscaled RRF values for all directions plotted together with small-scale RRF values. The upscaled values for the x- and y-directions are outside the range of the small-scale values.*

procedures for upscaling C_p^a. Another effect that the upscaling of C_p^a has on the results is that the upscaled R_k curves becomes less linear than in the case where there was no upscaling of C_p^a. This can especially be seen for the upscaled R_k curves for the x- and y-directions in Figure 4.9 and for the highest ${C_p^a}^*$ values.

Figure 4.10 shows the upscaled R_k values for the z-direction. They resemble the ones obtained when C_p^a was the same in the two rocks, but the values are not the same. Also here we see that the upscaled values depends in saturation, but not very much. The upscaled RRF values obtained for the different directions are plotted versus saturation together with the small-scale RRF values in Figure 4.11. We see that the RRF_x^* and RRF_y^* values are just above RRF_2, and outside the range of the small-scale RRF values. The values for upscaled RRF for the z-direction are approximately in the middle of the small-scale values. The values for the z-direction depend more on saturation

than the ones obtained for the x- and y-directions, but still the dependence appear to be weak. The upscaled RRF values for the different directions are given in Table 4.5.

Table 4.5: *Values obtained from upscaling RRF when C_p^a is different in the two rocks for the simple layered grid. The values obtained for the x- and y-directions are equal.*

s_w	RRF_x^*	RRF_y^*	RRF_z^*
0.25	3.2087	3.2087	2.5155
0.35	3.2080	3.2080	2.4453
0.45	3.2077	3.2077	2.4234
0.55	3.2075	3.2075	2.4149
0.65	3.2073	3.2073	2.4084
0.75	3.2072	3.2072	2.4253
mean	3.2077	3.2077	2.4388

4.3.4 Considering Other Procedures for Upscaling C_p^a

In this section we consider alternative procedures for upscaling C_p^a. In addition to volume averaging, we consider upscaling by harmonic, geometric and arithmetic averaging. We upscale C_p^a using the four methods just mentioned, and compare the results. The upscaled C_p^a values for the different methods are given in Table 4.6 together with the small-scale C_p^a values of Rock 1 and Rock 2. The upscaled values are plotted together with the small-scale values in Figure 4.12.

Table 4.6: *Small-scale and upscaled C_p^a values obtained using the different averaging techniques. The arithmetic average equals the volume average in this case since all the cells have the same volume and porosity. The different upscaling procedures produce fairly similar upscaled values.*

c	C_{p1}^a	C_{p2}^a	C_p^a * volume/ arithmetic	C_p^a * harmonic	C_p^a * geometric
0	0	0	0	0	0
0.25	0.00001	0.000015	0.00001333	0.00001286	0.00001310
0.5	0.000013	0.000018	0.00001633	0.00001595	0.00001615
0.75	0.000015	0.000020	0.00001833	0.00001800	0.00001817
1.0	0.000017	0.000023	0.00002100	0.00002058	0.00002080
1.25	0.000018	0.000025	0.00002267	0.00002213	0.00002241
1.5	0.000019	0.000027	0.00002433	0.00002368	0.00002402
2.0	0.000023	0.000028	0.00002633	0.00002611	0.00002622
2.75	0.000025	0.000030	0.00002833	0.00002812	0.00002823
3.0	0.000025	0.000030	0.00002833	0.00002812	0.00002823
4.0	0.000025	0.000030	0.00002833	0.00002812	0.00002823

In Section 4.3.3 we presented results that could indicate that using volume averaging to upscale C_p^a might not be the best way as we obtained upscaled values for R_k that was outside the range of the small-scale values. Since most of the flow is through Rock 2, we also suggested that more correct upscaled values of C_p^a should be closer to the C_p^a values of Rock 2, and that volume averaging may underestimate C_p^{a*}. Here we see that upscaled C_p^a values found from arithmetic, harmonic and geometric averaging does not produce values any closer to that of Rock 2 than what volume averaging does. Volume averaging and the arithmetic average produce here the same values, which is

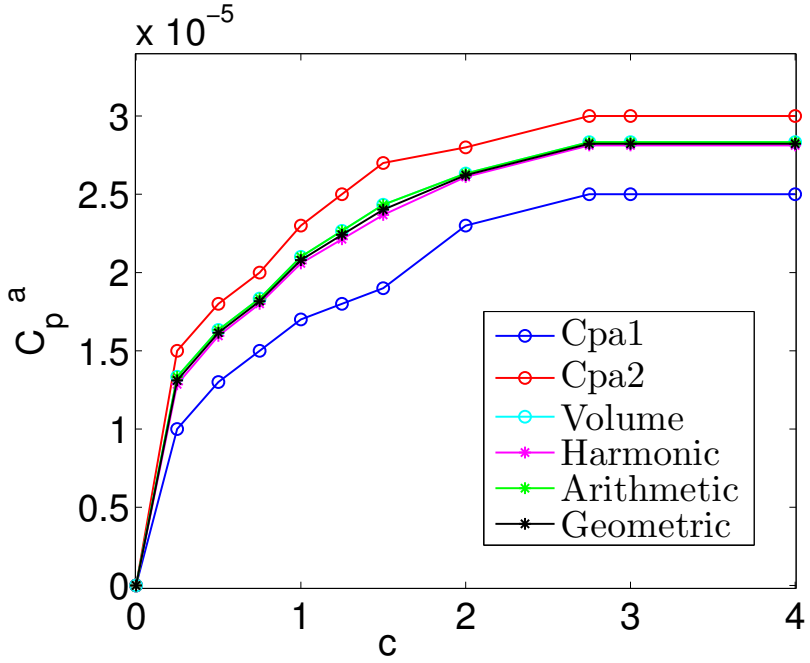

(a) Upscaled C_p^a values obtained from volume, harmonic, arithmetic, and geometric average plotted together with the small scale values.

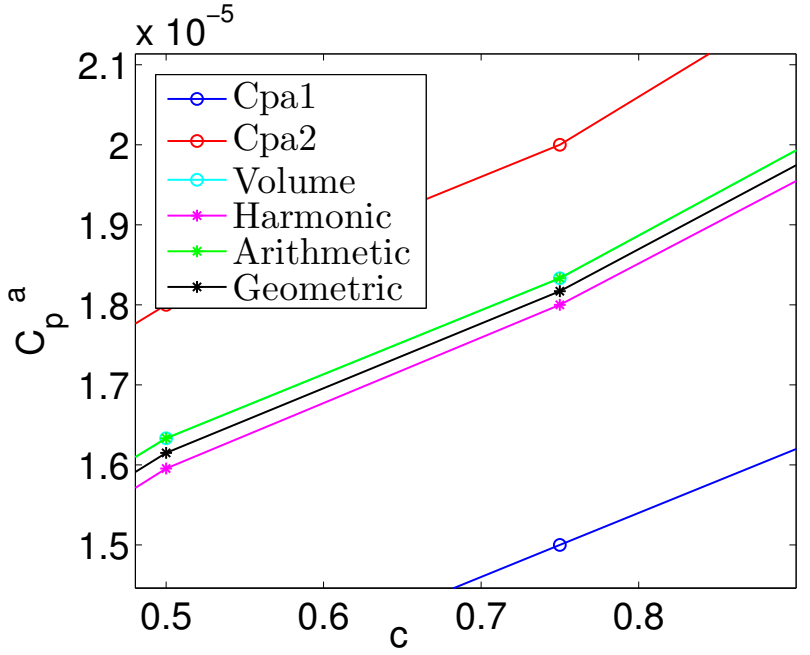

(b) Close-up of Figure 4.12a. The volume and arithmetic average produce the values closest to the C_p^a values of Rock 2.

Figure 4.12: *Upscaled C_p^a values obtained from volume, harmonic, arithmetic, and geometric averaging plotted together with the small-scale values. Volume and arithmetic averaging produce the same values in this case. In the close-up we see that the values obtained using volume and arithmetic averaging are the closest to the values of Rock 2.*

caused by all the cells in the grid having the same volume and porosity. The harmonic and geometric average produce values that are just below the values obtained using volume/arithmetic averaging. In Figure 4.13 the upscaled R^*_{kx} values for $s_w = 0.25$ for the simple layered grid are plotted versus the different $C_p^{a\,*}$ obtained using the different methods. We see that they all produce R^*_k values that are outside the range of the small-scale values. Since none of the alternative procedures for upscaling C_p^a that are suggested in this section produce values that are closer to being in the range of the small-scale values than what volume averaging does, we choose to stick with upscaling C_p^a by volume averaging and do not believe the alternative methods to be any better.

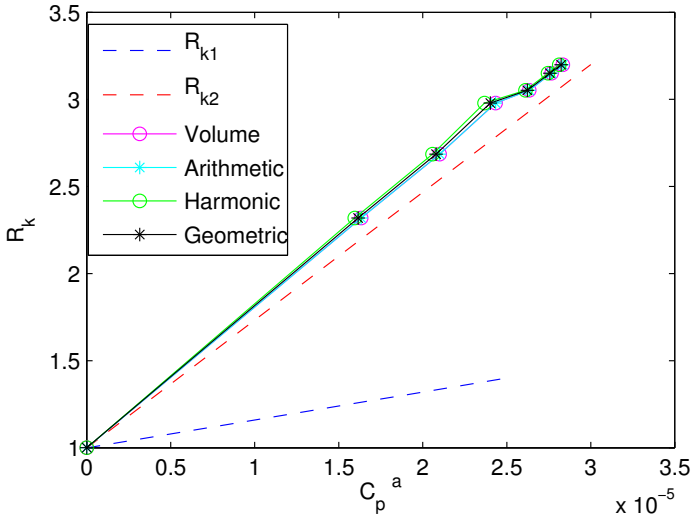

(a) *Upscaled R_k values for the x-direction versus upscaled C_p^a values obtained using the different upscaling procedures.*

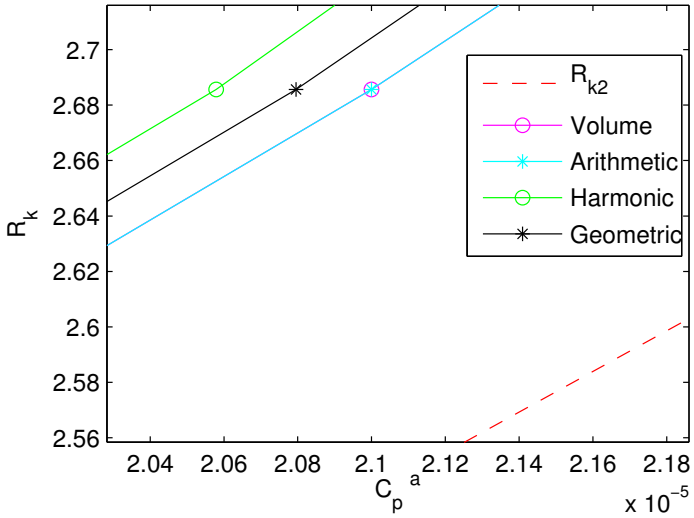

(b) *Close-up of Figure 4.13a, which shows that the volume and arithmetic average produce values closest to that of Rock 2.*

Figure 4.13: *Upscaled R_k values for the x-direction plotted against the the upscaled C_p^a values obtained using the different averaging methods, which are volume, arithmetic, harmonic, and geometric averaging. This is for a water saturation of 0.25. Wee see that volume and arithmetic averaging produce values closest to the values of Rock 2.*

4.4 Upscaling of Tilted Layered Case

We next consider the upscaling of the tilted layered grid in Figure 4.14. The grid is from [12]. The initial conditions are uniform saturation and concentration in space. The upscaling is performed as for the simple layered grin in the previous section. Upscaled absolute permeability for this grid is:

$$\mathbf{K}^* = \begin{pmatrix} 49.97 & 0 & 0 \\ 0 & 2.48 & 0.13 \\ 0 & 0.13 & 0.21 \end{pmatrix} \text{mD}$$

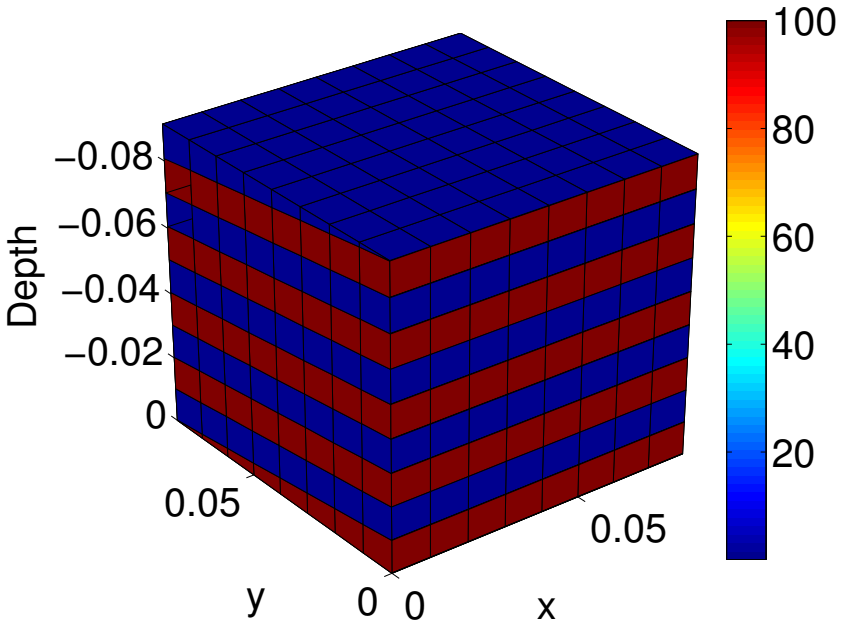

Figure 4.14: *Tilted layered grid consisting of layers that are almost horizontal, but a bit tilted. The colorbar shows permeability in mD, which is 0.1 mD for the blue rock and 100 mD for the red rock. The porosity is set to be 0.1 everywhere. The number of cells is 640. The grid consists of two types of rock, where the blue will be referred to as Rock 1 and the red as Rock 2.*

Upscaled relative permeabilities are plotted for each direction and together with the small-scale relative permeabilities in Figure 4.15. The upscaled relative permeabilities for the x-direction are very close to the relative permeabilities of Rock 2. This is because for flow in the x-direction the flow is along the layers and not across. The solution is therefore uniform saturation in space when the initial set-up is uniform saturation. Since Rock 2 is much more permeable than Rock 1, most of the flow is through Rock 2, and therefore upscaled relative permeabilities in the x-direction are close to that of Rock 2. In the z-direction, the upscaled relative permeabilities are approximately in the middle between the two small-scale curves, which is because in the z-direction the flow is across the layers and must go through both types of rock. In the y-direction the flow is both along and slightly across the layers, and the upscaled relative permeabilities are closer to that of Rock 2 than that of Rock 1.

Figure 4.16 shows upscaled C_p^a values together with small-scale C_p^a values, where the upscaled values are found from volume averaging. The values are given in Table 4.7.

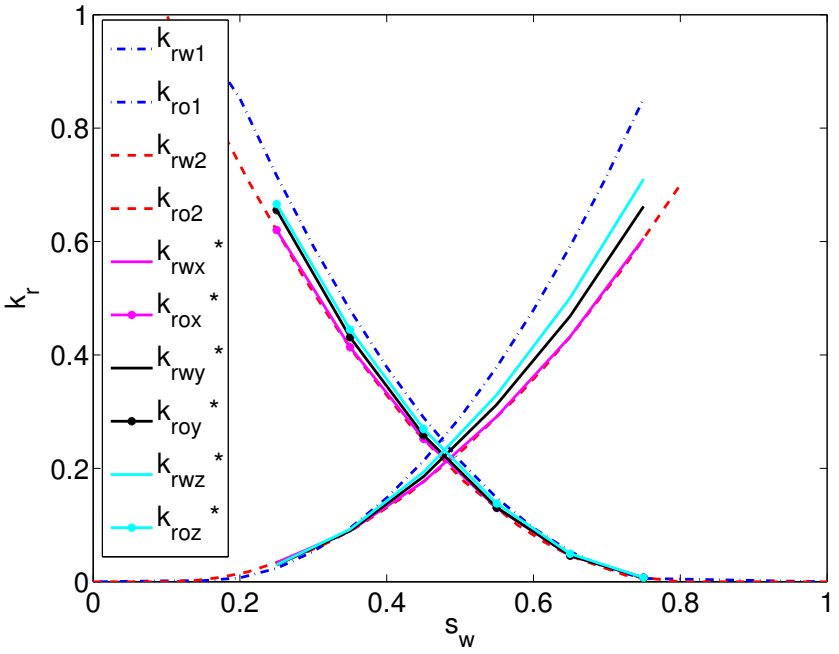

Figure 4.15: *Small-scale and upscaled relative permeabilities in the x-, y- and z-directions for the tilted layered grid in Figure 4.14. The dashed lines are for the small-scale values, while the solid lines are for the upscaled permeabilities in the different directions. Oil relative permeabilities are the decreasing lines, while water relative permeabilities are increasing with water saturation.*

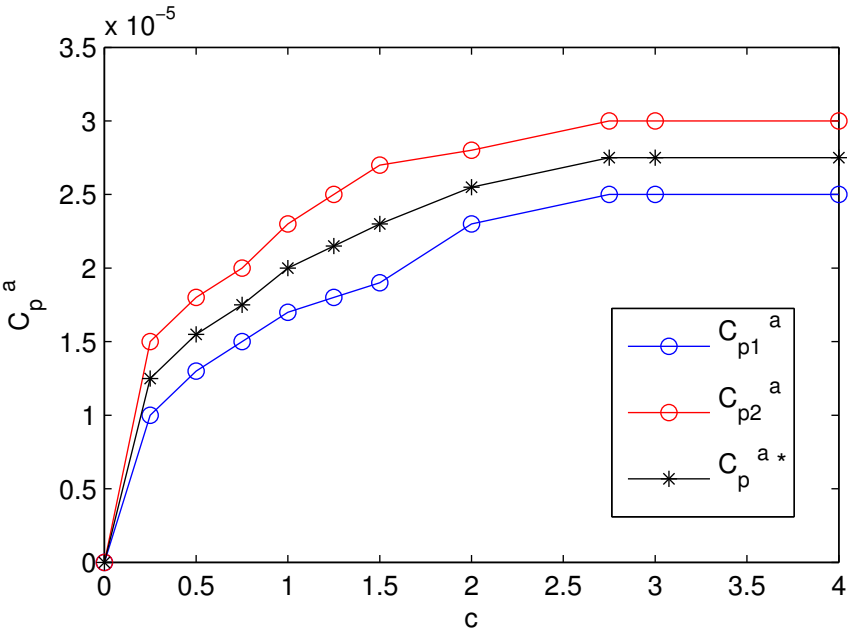

Figure 4.16: *Small-scale C_p^a values for the two rocks plotted together with upscaled C_p^a values found from volume averaging for the tilted layered grid.*

Table 4.7: *Small-scale C_p^a values for the two rocks and upscaled C_p^a values found from volume averaging.*

c	C_{p1}^a	C_{p2}^a	C_p^a*
0	0	0	0
0.25	0.00001	0.000015	0.000013
0.5	0.000013	0.000018	0.000016
0.75	0.000015	0.000020	0.000018
1.0	0.000017	0.000023	0.000020
1.25	0.000018	0.000025	0.000021
1.5	0.000019	0.000027	0.000023
2.0	0.000023	0.000028	0.000026
2.75	0.000025	0.000030	0.000028
3.0	0.000025	0.000030	0.000028
4.0	0.000025	0.000030	0.000028

Upscaled R_k for the different directions for $s_w = 0.25$ are plotted in Figure 4.17. We see that the values obtained for the x-direction are outside the range of the small-scale values of Rock 1 and Rock 2, similar as what happened for the simple layered grid in the previous section for the x- and y-directions. Also here we believe this to be an effect from the upscaling of C_p^a, but based on the results in Section 4.3.4 we do not believe the other simple averaging methods to produce upscaled values closer to being in the range of the small-scale values. Perhaps should other methods than simple averaging methods be considered. Upscaled R_k values for the y- and z-directions are here pretty similar, and are approximately in the middle of the small-scale values.

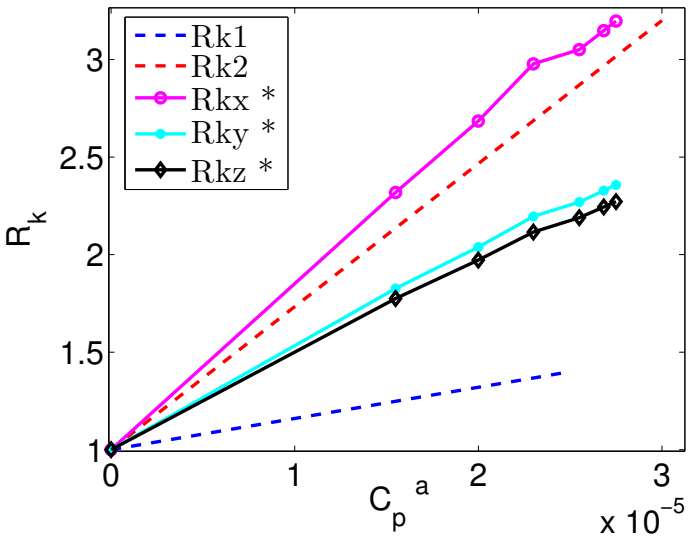

Figure 4.17: *Upscaled R_k values for the x-, y-, and z-directions for $s_w = 0.25$. for the tilted layered grid. The upscaled values for the x-direction are outside the range of the small-scale values.*

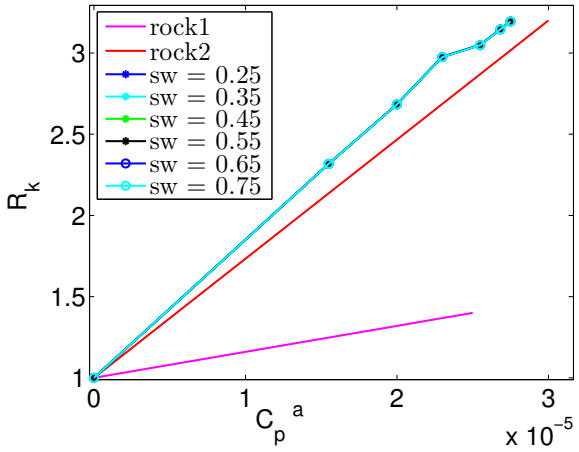

(a) Upscaled R_k values for the x-direction.

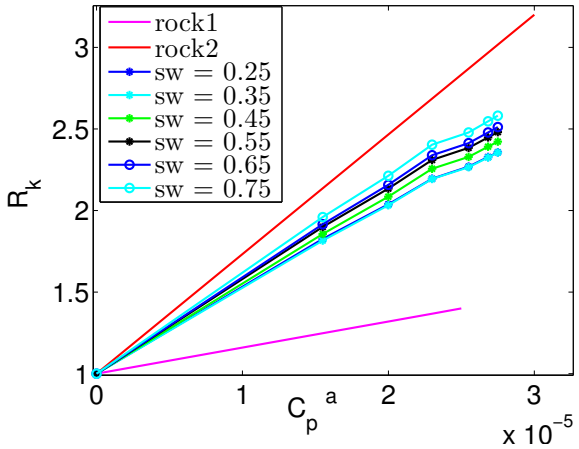

(b) Upscaled R_k values for the y-direction.

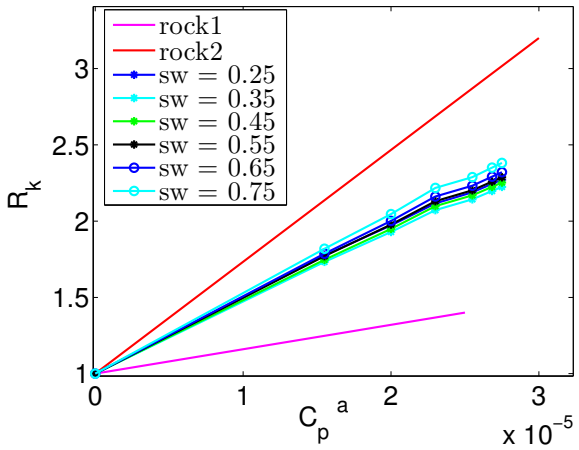

(c) Upscaled R_k values for the z-direction.

Figure 4.18: *Upscaled R_k values for different saturations for the tilted layered grid. The values obtained for the x-direction are outside the range of the small-scale values.*

Upscaled R_k values for the x-direction are plotted for different saturations in Figure 4.18a, and we see that the values depend very little on saturation. This is believed to be caused by the solution at steady state being constant saturation in space, as the initial saturation distribution is uniform in space. Upscaled R_k values for the y-direction are plotted in Figure 4.18b for different saturations, and we see that in y-direction the values depend on saturation. Also the upscaled values for the z-direction, which are plotted in Figure 4.18c, depend on saturation. For the three directions, the values obtained for the y-direction depends the strongest on saturation.

Upscaled values for RRF for the three directions are plotted versus saturation in Figure 4.19 together with the small-scale values, which are 1.4 and 3.2. The values for the y- and z-directions are almost similar, and appear to have approximately the same dependence on saturation. The upscaled values for both the y- and z-direction increase with saturation. The upscaled RRF values for the x-direction are just above the RRF of Rock 2, and depend very little on saturation as the R^*_{kx} values did not depend much on saturation either. The values for upscaled RRF for the different directions are given in Table 4.8.

s_w	RRF^*_x	RRF^*_y	RRF^*_z
0.25	3.2089	2.3590	2.2724
0.35	3.2074	2.3582	2.2270
0.45	3.2067	2.4264	2.2556
0.55	3.2063	2.4840	2.2906
0.65	3.2061	2.5156	2.3247
0.75	3.2059	2.5855	2.3862
mean	3.2069	2.4548	2.2928

Table 4.8: *Upscaled RRF values for the different directions for different saturations.*

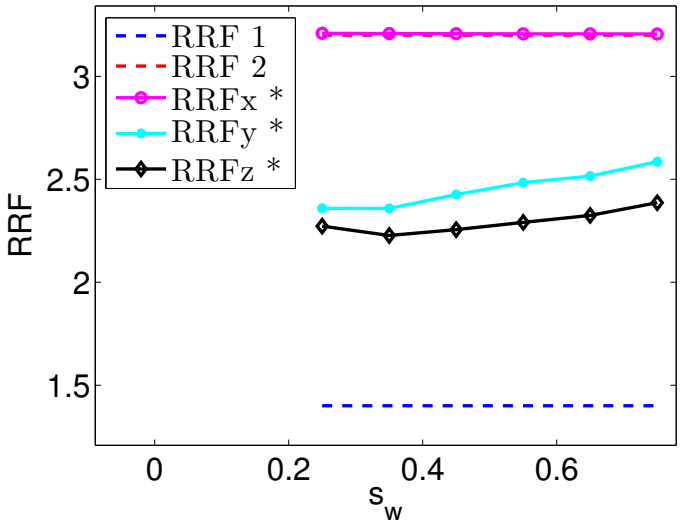

Figure 4.19: *Plot of the upscaled RRF values versus saturation for different directions for tilted layered grid, plotted together with the small-scale values.*

4.5 Upscaling of Oblong Grid

We now consider the upscaling of the oblong grid illustrated in Figure 4.20, which consists of four types of rock. The grid is a Cartesian grid of dimensions 100x2x2, and thus we only perform upscaling in the x-direction. The grid is assigned properties (permeability, porosity, and rock type distribution) based on properties of parts of the grid Test model 1 in [12]. Each type of rock is assigned different relative permeability curves, residual resistance factors, and C^a_p functions. The grid has nonuniform porosities, and nonuniform absolute permeabilities. The absolute permeability is isotropic in the x- and y-directions, but not in the z-direction.

We first perform single-phase upscaling, and obtain from this the upscaled absolute permeability

tensor:

$$\mathbf{K}^* = \begin{pmatrix} 10.69 & 0 & 0 \\ 0 & 55.3 & 0 \\ 0 & 0 & 35.9 \end{pmatrix} \text{mD}.$$

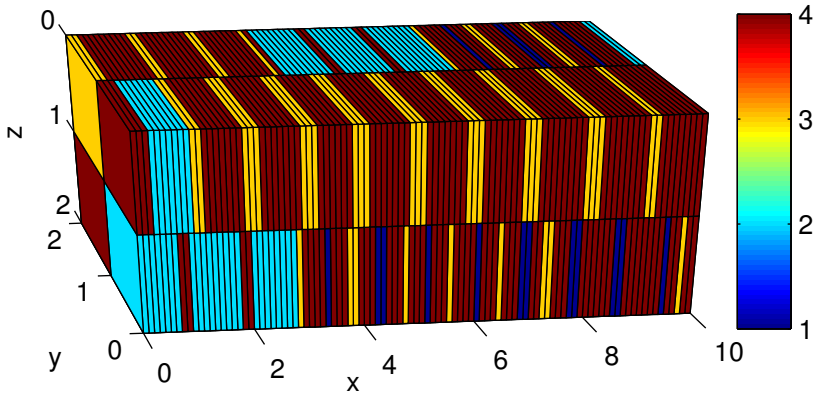

Figure 4.20: *Illustration of the oblong grid, where each color corresponds to a type of rock. The grid consists of four types of rock and of 100x2x2 = 400 cells. The grid is only upscaled in the x-direction.*

Upscaled relative permeabilities for oil and water are plotted together with the small-scale relative permeabilities in Figure 4.21.

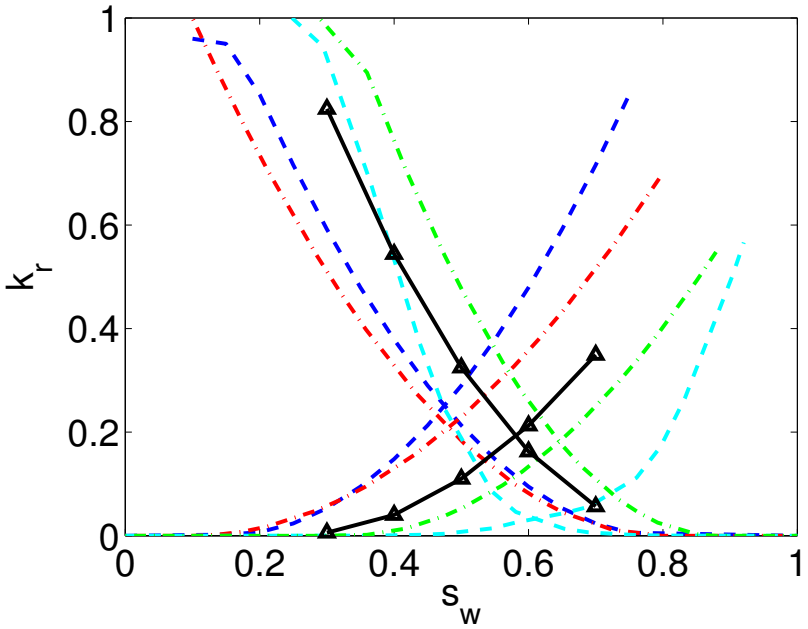

Figure 4.21: *Upscaled relative permeabilities for the x-direction plottes together with the small-scale relative permeabilities of the four types of rock in the oblong grid. The dashed lines are small-scale relative permeabilities, whereas the black solid lines are upscaled relative permeabilities in the x-direction. The decreasing lines (along the x-axis) are for oil, while the increasing lines are for water relative permeabilities.*

We upscale C_p^a using volume averaging, and the upscaled values are plotted together with the small-scale values of the different rocks in Figure 4.22. The values are given in Table 4.9.

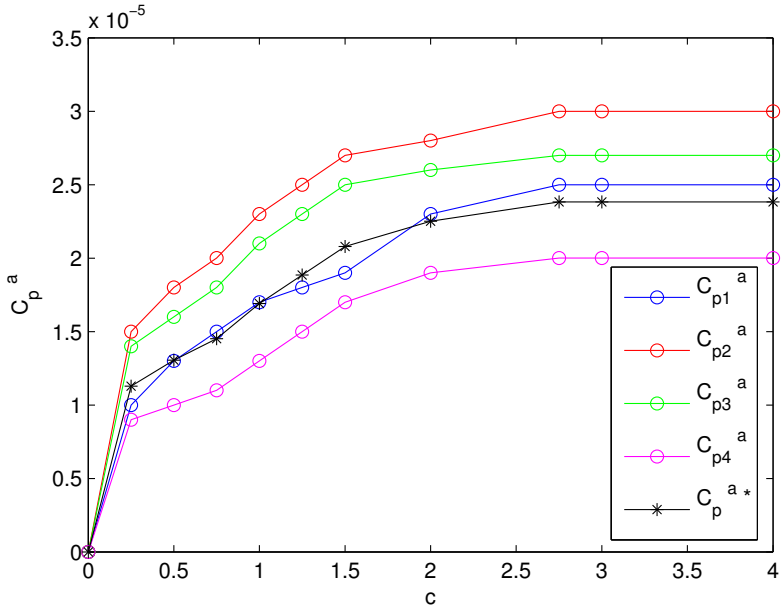

Figure 4.22: *Upscaled C_p^a values (black line) found from volume averaging plotted together with the C_p^a values of the four different rocks in the oblong grid.*

Table 4.9: *Small-scale C_p^a values for the four rocks and upscaled C_p^a values found from volume averaging.*

c	C_{p1}^a	C_{p2}^a	C_{p3}^a	C_{p4}^a	C_p^a*
0	0	0	0	0	0
0.25	0.00001	0.000015	0.000014	0.000009	0.000011
0.5	0.000013	0.000018	0.000016	0.000010	0.000013
0.75	0.000015	0.000020	0.000018	0.000011	0.000015
1.0	0.000017	0.000023	0.000021	0.000013	0.000017
1.25	0.000018	0.000025	0.000023	0.000015	0.000019
1.5	0.000019	0.000027	0.000025	0.000017	0.000021
2.0	0.000023	0.000028	0.000026	0.000019	0.000023
2.75	0.000025	0.000030	0.000027	0.000020	0.000024
3.0	0.000025	0.000030	0.000027	0.000020	0.000024
4.0	0.000025	0.000030	0.000027	0.000020	0.000024

We further upscale the permeability reduction factor R_k for the x-direction, and the values are plotted in Figure 4.23. The upscaled R_k values are almost equal to the values of Rock 2, and are not very different for different saturations. Figure 4.23b shows a close-up of the R_{kx}^* values, and also here there is not a clear pattern in how the upscaled R_k values depend on saturation. Upscaled RRF values for the x-direction are found from the slopes of the different lines, and the values are plotted in Figure 4.24 for different saturations together with the small-scale values for RRF in the different rocks. Also here the upscaled RRF values depend on saturation, but the dependence does not seem to be strong. The upscaled RRF_x values for different saturations are given in Table 4.10.

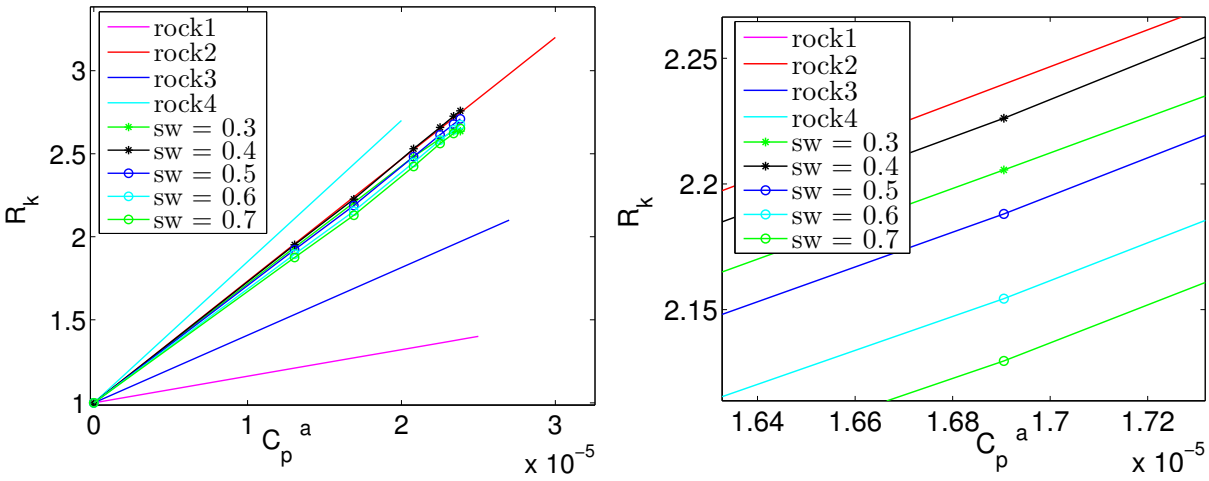

(a) Upscaled R_k values for different saturations plotted together with the small-scale values.

(b) Close-up of the upscaled R_k values.

Figure 4.23: *Upscaled R_k values for the x-direction for the oblong grid.*

s_w	RRF_x^*
0.30	2.66
0.40	2.76
0.50	2.7115
0.60	2.6778
0.70	2.6564
mean	2.6931

Table 4.10: *Upscaled RRF values for the x-direction for the oblong grid. The small-scale values are 1.4, 3.2, 2.1, and 2.7 for Rock 1, 2, 3, and 4, respectively.*

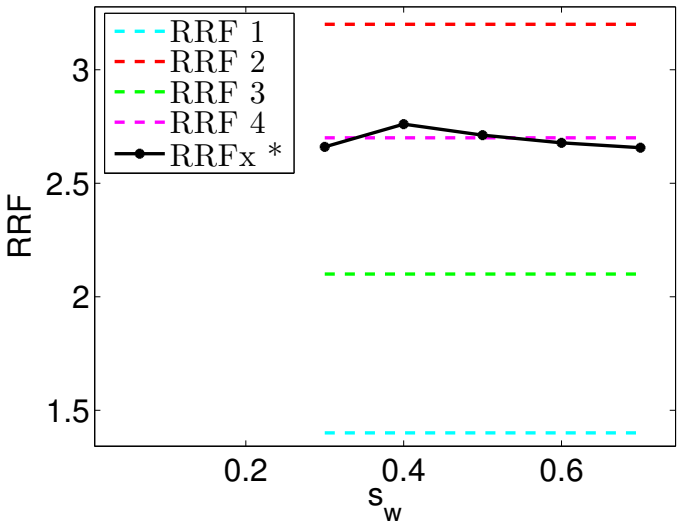

Figure 4.24: *Upscaled RRF values for the x-direction, plotted with the small-scale RRF values for the oblong grid.*

4.6 Upscaling of Small Realistic Case

We now look the at upscaling of a small realistic case illustrated in Figure 4.25 which consists of four types of rock. The position of the different rock types is shown in Figure 4.25a. The permeability is isotropic and is shown in Figure 4.25b. The porosity is nonuniform, and is plotted in Figure 4.25c.

From single-phase upscaling we obtain the upscaled absolute permeability tensor:

$$\mathbf{K}^* = \begin{pmatrix} 2.572 & 0.019 & -0.02 \\ 0.019 & 2.538 & 0 \\ -0.02 & 0 & 0.387 \end{pmatrix} \text{D}.$$

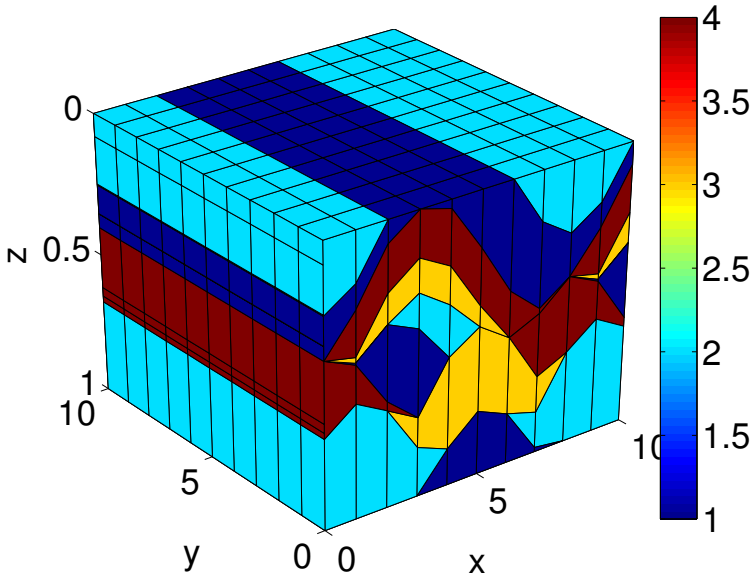

(a) Illustration of small realistic case, where each color represents a rock type.

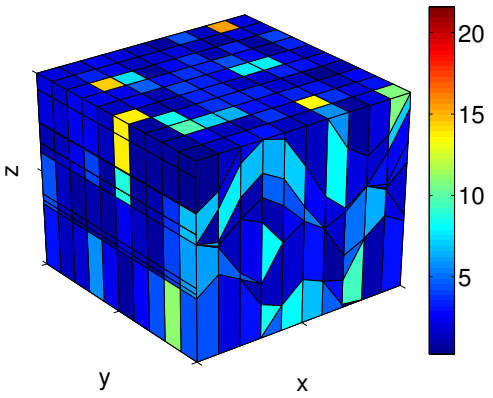

(b) Grid with permeability in Darcy. The permeability is isotropic.

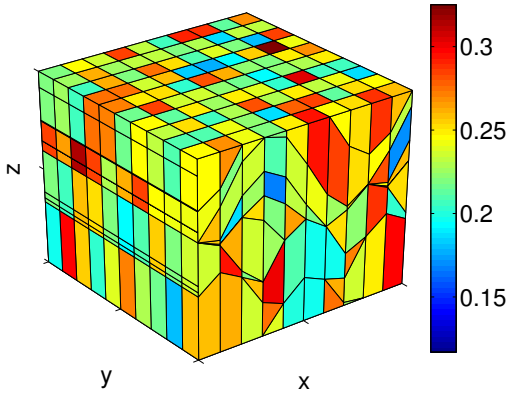

(c) Grid with porosity.

Figure 4.25: *Illustration of the grid of small realistic case with rock type, permeability, and porosity. The number of cells is 710.*

The upscaled relative permeabilities for oil and water are plotted together with the small-scale relative permeabilities in Figure 4.26. The black lines are for the upscaled relative permeabilities in the different directions. The values obtained for the x- and y-directions are almost equal.

Next, we upscale C_p^a for different concentrations using volume averaging. Figure 4.27 shows upscaled C_p^a values together with the small-scale values for the different rocks. The values are given in Table 4.11.

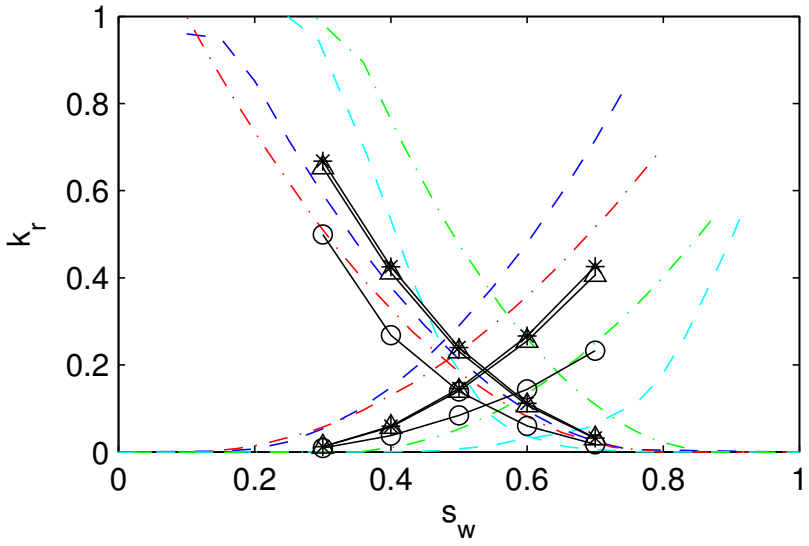

Figure 4.26: *Upscaled relative permeabilities for the different directions plotted together with small-scale relative permeabilities of the four types of rock for the small realistic case. The dashed lines are small-scale relative permeabilities, whereas the black solid lines are upscaled relative permeabilities for the different directions. The black lines with the circles are for the z-direction, while the lines with the triangles and stars are for the x- and y-directions, respectively. The decreasing lines (along the x-axis) are for oil, while the increasing lines are for water.*

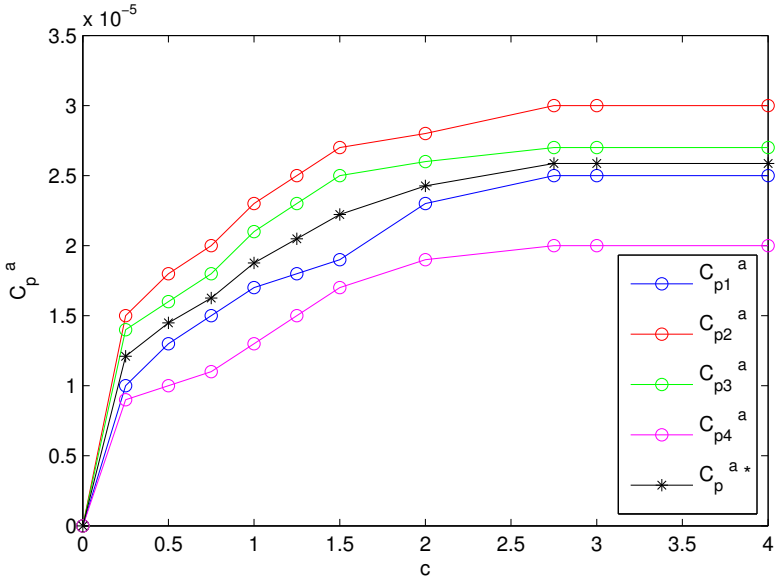

Figure 4.27: *Upscaled C_p^a values plotted together with small-scale values for the different rocks for the small realistic case.*

We further upscale R_k and RRF. Upscaled R_k values for the different directions for a water saturation of 0.25 are plotted together with the small-scale values in Figure 4.28. We see that the upscaled values obtained for the different directions are pretty similar.

Upscaled R_k values for different saturations for the different directions are plotted in Figure 4.29.

Table 4.11: *Small-scale values for C_p^a and upscaled values found from volume averaging for the simple realistic case with four rocks.*

c	C_{p1}^a	C_{p2}^a	C_{p3}^a	C_{p4}^a	C_p^{a*}
0	0	0	0	0	0
0.25	0.00001	0.000015	0.000014	0.000009	0.000012
0.5	0.000013	0.000018	0.000016	0.000010	0.000014
0.75	0.000015	0.000020	0.000018	0.000011	0.000016
1.0	0.000017	0.000023	0.000021	0.000013	0.000019
1.25	0.000018	0.000025	0.000023	0.000015	0.000020
1.5	0.000019	0.000027	0.000025	0.000017	0.000022
2.0	0.000023	0.000028	0.000026	0.000019	0.000024
2.75	0.000025	0.000030	0.000027	0.000020	0.000026
3.0	0.000025	0.000030	0.000027	0.000020	0.000026
4.0	0.000025	0.000030	0.000027	0.000020	0.000026

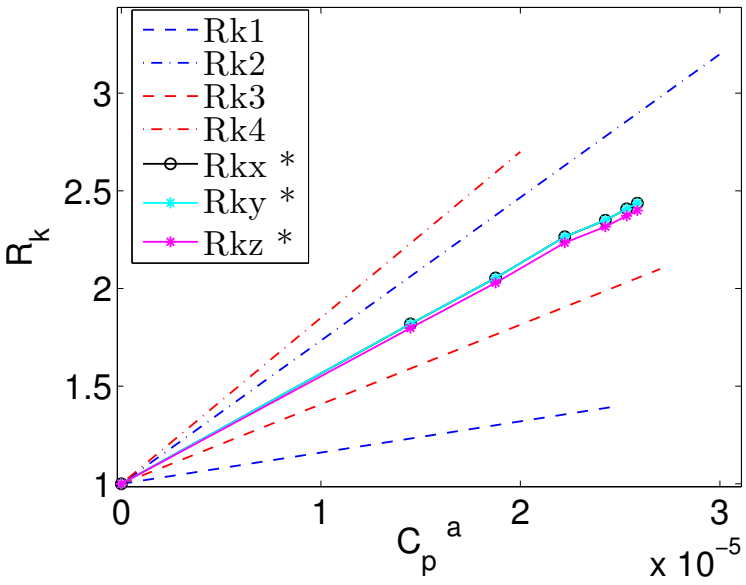

Figure 4.28: *Upscaled R_k values for the x-, y-, and z-directions for $s_w = 0.25$. The values obtained for the different directions are almost equal.*

The values obtained for the x-direction are plotted in Figure 4.29a. The values obtained for the y-direction are plotted in Figure 4.29b, while Figure 4.29c shows the upscaled R_k values for the z-direction. We see that the upscaled R_k values for all directions depend on saturation, but the dependence is the strongest in the y-direction.

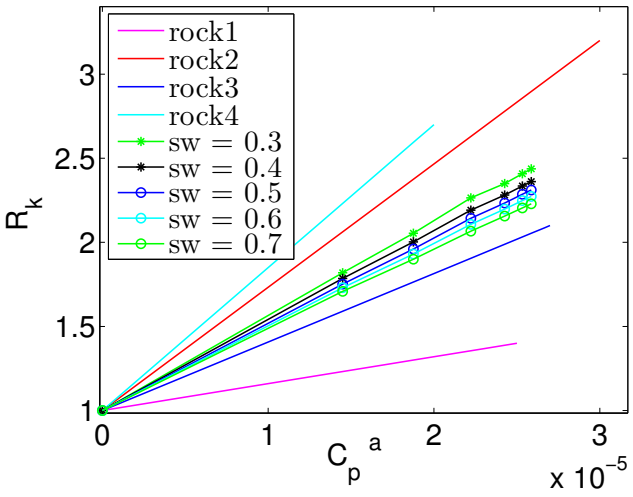

(a) Upscaled R_k values for the x-direction.

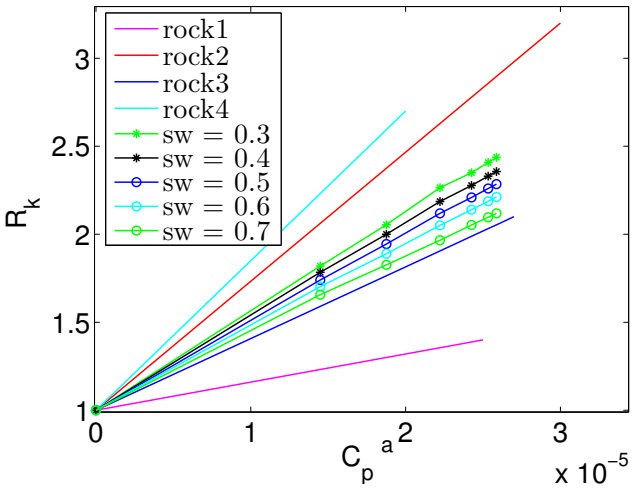

(b) Upscaled R_k values for the y-direction.

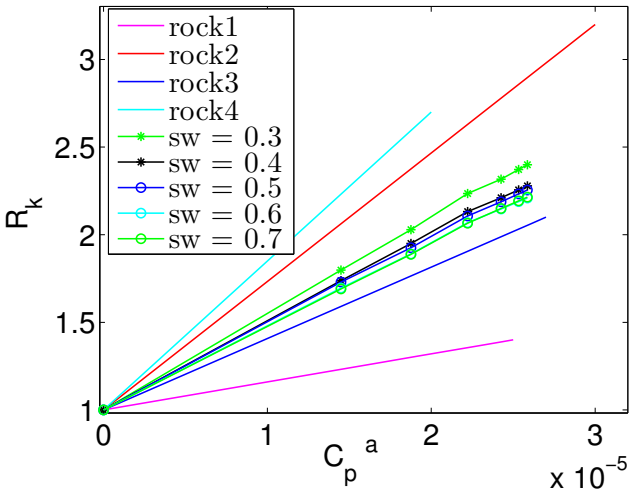

(c) Upscaled R_k values for the z-direction.

Figure 4.29: *Plots of upscaled R_k values for different directions for the small realistic case. The upscaled values depend on saturation, and the dependence is strongest in the y-direction.*

Upscaled values for RRF are found from the slopes of the upscaled R_k lines for the different directions, and the upscaled RRF values are plotted in Figure 4.30. In Figure 4.30a the upscaled RRF values for the different directions are plotted together with the small-scale RRF values for the different rock types. The upscaled RRF values for the different directions are relatively similar, and (almost) all decrease as saturation increases. The exception is upscaled RRF_z for $s_w = 0.7$. Figure 4.30b shows a close-up of the upscaled RRF values for the different directions. They are (almost) all decreasing lines, but does not have the same slope and shape. The upscaled RRF values are given in Table 4.12.

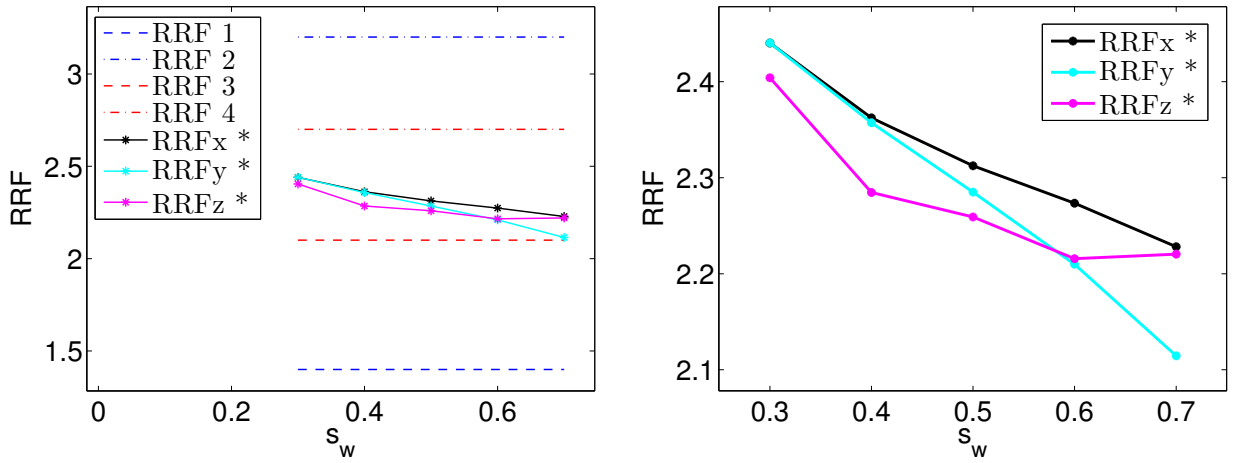

(a) *Upscaled RRF values for the x-, y-, and z-directions together with the small-scale values of RRF in the different rocks.*

(b) *Close-up of the upscaled RRF values for the different directions.*

Figure 4.30: *Upscaled values for RRF for the small realistic case. The values obtained for the different directions are relatively similar.*

Table 4.12: *Upscaled values of RRF for the small realistic case with four types of rock.*

s_w	RRF_x^*	RRF_y^*	RRF_z^*
0.30	2.4402	2.4403	2.4041
0.40	2.3623	2.3572	2.2846
0.50	2.3124	2.2850	2.2591
0.60	2.2734	2.2099	2.2157
0.70	2.2281	2.1145	2.2204
mean	2.3233	2.2814	2.2768

4.7 Challenges

As we increase the complexity of the system we want to upscale, we encounter several challenges with the program. The program (solver) can only handle up to a certain number of grid cells, and this number is strongly dependent on the number of types of rock in the grid. When the grid consists of only one type of rock it can easily handle tens of thousands of cells, but as soon as different regions are introduced the number decreases significantly. This is something that can probably be improved,

and which should be done in the future so that upscaling of larger and more complex grids can be performed in a reasonable time. Currently the solver can barely handle about 5000 cells when the grid consists of four types of rock.

Another challenge we encountered is that in some cases the system is not able to reach steady state, and this we saw for grids that are more complex than the ones that are upscaled in this chapter. The reason for this is currently unknown, and this should be examined further. A step in the right direction would probably be to make a qualified guess of what the steady state solution will look like, and then use this guess as the initial state when setting up the system. A qualified guess could be the saturation distribution obtained from the viscous or capillary limit for two-phase upscaling. Also this is left as further work.

4.8 Summary

In this chapter we have performed single-, two-phase, and polymer upscaling of four different grids. We have seen that the upscaled values of R_k may be outside the range of the small-scale values, which we believe to be caused by the upscaling of C_p^a. However, this only appears to happen for grids with layered rocks and when the flow is only along the layers. Other simple averaging techniques are attempted for the upscaling of C_p^a, but volume averaging seems to produce the most satisfying results. We have also seen that the upscaled R_k values depend on direction and are functions of saturation, even though the small-scale values are not. Thus, also upscaled RRF values become functions of saturation and depends on direction, as they are found by using the upscaled R_k values. How much the uspcaled values depend on saturation varies for different grids, but overall the dependence does not seem to be large. In the next chapter we evaluate the upscaling results for two of the grids in this chapter, and compare the solutions obtained using upscaled values on a coarse grid with the solutions obtained using the small-scale values on a fine grid.

Chapter 5

Evaluation of Upscaling Results

After obtaining upscaling results, it is important to check the correctness of these results, *i.e.*, how well the upscaled parameters produce a flow pattern similar to the one obtained using small-scale parameters. A natural way to check this is by comparing the solution of a system using small-scale parameters on a fine grid with the solution of the same system using upscaled parameters on a coarse grid. This is done in the following chapter to evaluate some of the results presented in Chapter 4.

5.1 How to Evaluate the Results

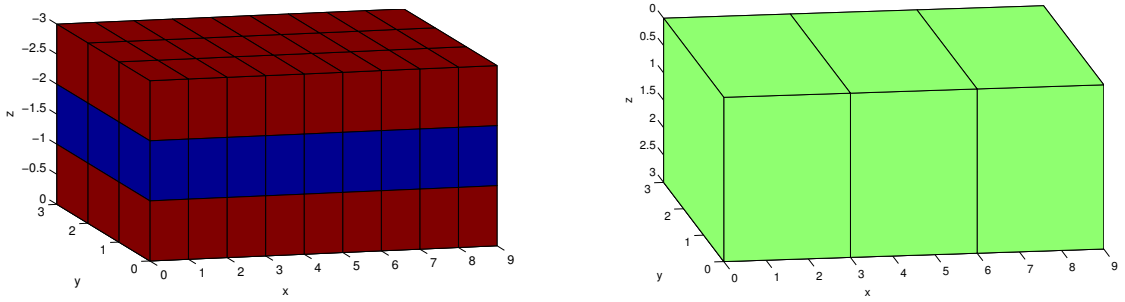

(a) *Fine scale grid which is duplicated three times. On fine scale the original grid is 3x3x3. Here it is duplicated three times in x-direction, which produces a 9x3x3 grid.*

(b) *Coarse grid. In this case it is three cells in x-direction, as the fine grid is duplicated three times in x-direction.*

Figure 5.1: *Illustration of duplicated fine scale grid and coarse grid with number of cells corresponding to the times of duplication. The grid in 5.1a is the duplicated fine scale grid, and the flow in this grid is found by using small-scale parameters. The grid in 5.1b is the coarse grid, where the flow is found by using upscaled parameters.*

A fine scale grid with fine scale parameters is upscaled to one coarse grid cell and a set of upscaled parameters for that coarse grid cell is obtained. When we want to compare the solutions the two different sets of parameters give, we can not just look at this fine scale grid and this single coarse grid cell, as on coarse scale this will only be one cell and not much of a solution to compare. Therefore, the grid is duplicated in one direction, so that we have a row of the same grid. The number of coarse cells will then be the number of times the fine scale grid is duplicated, and this may be as many

times as possible, and just limited by how many cells the computer can handle when duplicating the fine scale grid. Figure 5.1 illustrates the duplication of the simple layered grid in Figure 4.2. The grid is duplicated three times which corresponds to three coarse grid cells. The grid should be duplicated more than three times, but here it is just done for illustration purposes. Upscaling is performed for single-, two-phase and polymer flow, and the results are tested by comparing the fine and coarse scale solution of a two-phase system and polymer flow system. The upscaled permeability and relative permeability are tested by looking at a two-phase system, while the polymer upscaling is tested by looking at a polymer system.

We compare the solution obtained by using small-scale parameters on the small-scale duplicated grid and the upscaled parameters on the coarse scale by looking at the process of water and/or polymer displacing oil. By water and/or polymer displacing oil it is not meant pure water displacing pure oil, but rather that an area with mostly water is set up and "pushed into" an area containing mostly oil. This is to keep the saturations in the range of the saturations that the relative permeability curves are defined for. Fixed boundary conditions are used, and the flow is driven by a pressure gradient. Water (mainly) flows in on one side of the domain, and pushes the fluids present in the domain (mainly oil) towards the opposite side and out of the domain. No-flow boundary conditions are imposed on the other sides. Figure 5.2 illustrates the set up for the testing of two-phase upscaling and polymer upscaling. The arrows indicate flow direction. Mainly water comes in from the left hand side, and a water front will move towards the right and displace the oil. We expect first the water saturation at the outlet face to be low as only mainly oil will flow out first, but that it will increase when the water front hits the outlet boundary. This side where the fluids leave the domain will be referred to as the outlet boundary side. In the case of polymer flow the water will initially contain a layer with polymer which will spread out in the water and move with the water front. The amount of water that flows out is recorded for different times, and is compared for the two grids. In the case of polymer flow, also the concentration at the outlet boundary is recorded and compared.

We want to record the saturation at the outlet boundary side for the fine and coarse grid. For the fine scale grid an average saturation needs to be found for the grid cells that make up the outlet side face, and this is found by taking the volume average of the values of the cells belonging to the outlet boundary. This is done as in Equation (3.9i), but only using the values of the cells at the outlet boundary. The average concentration at the outlet boundary is found in a similar way, as in Equation (3.9j), but only using the values of the cells belonging to the outlet boundary. For the coarse scale there will only be one saturation and concentration value as there is only one cell. The saturation and concentration at the outlet boundary side is plotted against time, and compared for the two scales. Hopefully, the water and polymer front will hit the outlet boundary at approximately the same time when using small-scale and upscaled values.

The solutions obtained from the two grids will differ because the upscaled parameters are approximations to the small-scale parameters and will not produce exactly the same flow pattern, but also simply because the solutions are obtained from different grids. To study the effect that just using two different grids has on the results, we do a simulation where the small-scale grid is set to only consist of one type of rock so that there will be no upscaling effect. Then the difference in the solutions will be caused by just the grids being different. When performing upscaling with several types of rock in the small-scale grid and there actually being an upscaling effect, the solutions will no matter how good the upscaling is, differ as much as the solutions obtained here.

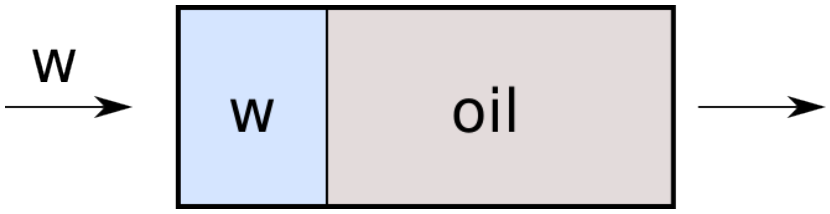

(a) Set up for two-phase flow.

(b) Set up for polymer flow.

Figure 5.2: *Illustration of how the systems are set up when comparing solutions of fine-scale system with coarse scale systems for two-phase flow (5.2a) and polymer flow (5.2b). Arrows indicates flow direction, and the w over the arrow at the left hand side indicated that mainly water comes in on that side. The flow is driven by a pressure gradient. Though the areas are referred to as water, oil and polymer, it is not meant pure water and oil, but simply that the area of oil consists of mostly oil, and the area of water consists mainly of water.*

5.2 Testing Simple Layered Grid

To test the upscaling results of the simple layered grid in Section 4.3 the grid is duplicated 30 times in x-direction, which gives 30 coarse cells in x-direction. This is illlustrated in Figure 5.3, which shows the small-scale duplicated grid and the corresponding coarse grid. In this way we test the upscaling results obtained for the x-direction.

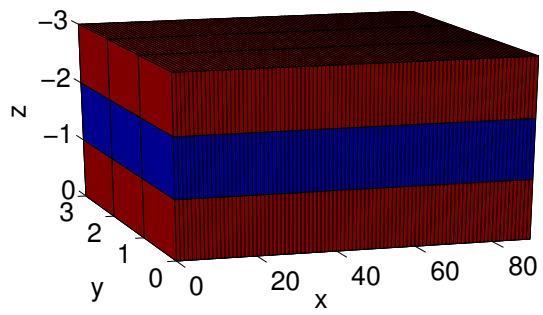

(a) Simple layered grid on small-scale duplicated 30 times. Different colors indicate different rock types.

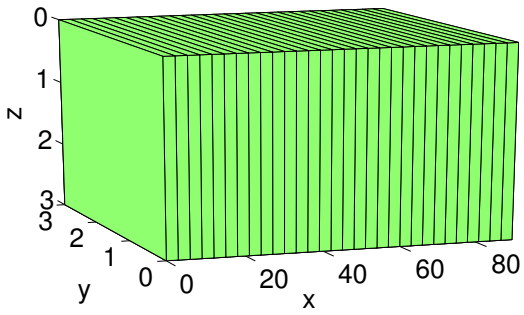

(b) Coarse grid with dimensions 30x1x1.

Figure 5.3: *Shows duplicated grids on fine and coarse scale for the simple layered grid.*

5.2.1 Difference Caused by Grids

We first run a simulation where the grids consist of only one type of rock to look at the effect that using two different grids has on the solutions. Figure 5.4a and Figure 5.4b shows the saturation set-up at initial state for the fine and coarse grid. The set-up is equal for the two grids as we want to compare the solutions of the same system. A pressure gradient of 1 bar is set up in x-direction so that it drives a flow in the positive x-direction. The system is solved for a number of time steps, which is typically some more steps than what is needed for the water front to reach the outlet boundary side. The amount of water going out through the outlet side is plotted against time for the solutions obtained for the two different grids.

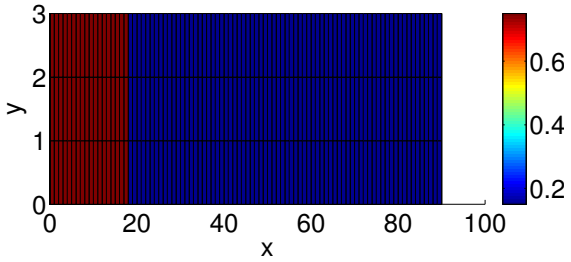

(a) Initial saturation in fine grid. Colorbar shows water saturation.

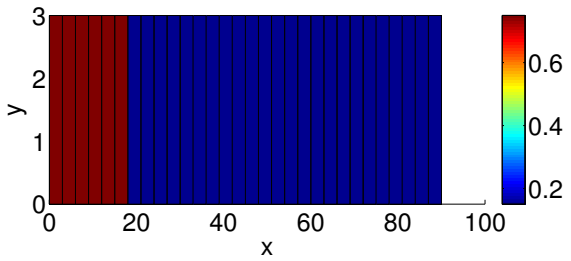

(b) Initial saturation in coarse grid. Colorbar shows water saturation.

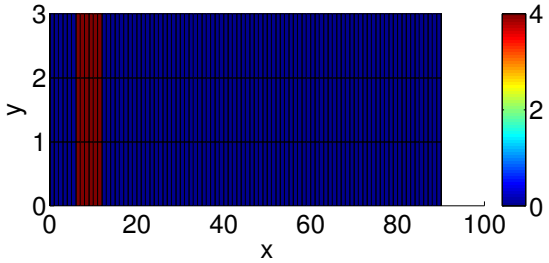

(c) Initial concentration in fine grid for polymer simulation. Colorbar shows polymer concentration.

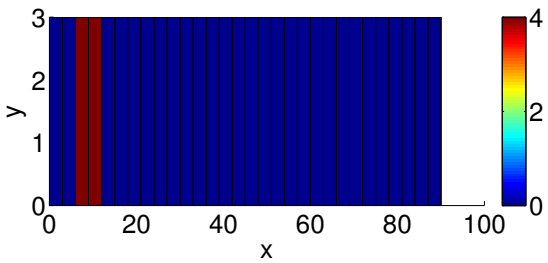

(d) Initial concentration in coarse grid for polymer simulation. Colorbar shows polymer concentration.

Figure 5.4: *Figure 5.4a and 5.4b shows initial saturation distribution set up for the fine and coarse grid used for both two-phase and polymer flow simulations. The red represents a water saturation of 0.75, whereas in the blue $s_w = 0.15$. Figure 5.4c and 5.4d shows initial concentration distribution in the two grids used when running a polymer flow simulation. The set-ups are similar for the two grids, as it must be since we want to compare the solutions of the same systems.*

We first consider the solution of a two-phase system for the two grids, where the polymer concentration is set to zero everywhere. The saturations for the two-phase system at the outlet boundary side are plotted in Figure 5.5a for the fine and coarse grid. We see that the solutions are very similar.

We then consider polymer flow in the two grids when there is only one type of rock present in the grids. The initial set-up for saturations is equal to the set-up for the two-phase system, but now a vertical layer with a polymer concentration of 4 is put in the water. This is illustrated in Figure 5.4c and Figure5.4d for the fine and coarse grid. For polymer flow we compare both the saturation and the concentration at the outlet boundary for each time step for the two grids. The saturations at the outlet boundary for polymer flow are plotted in Figure 5.5b, and also here the solutions obtained from the two grids are very similar. The polymer concentration at the outlet boundary is plotted

versus time in Figure 5.5c. We can see that there is some difference, but not much. The polymer spreads out in the water, and the polymer concentration at time step 23 is plotted in Figure 5.6.

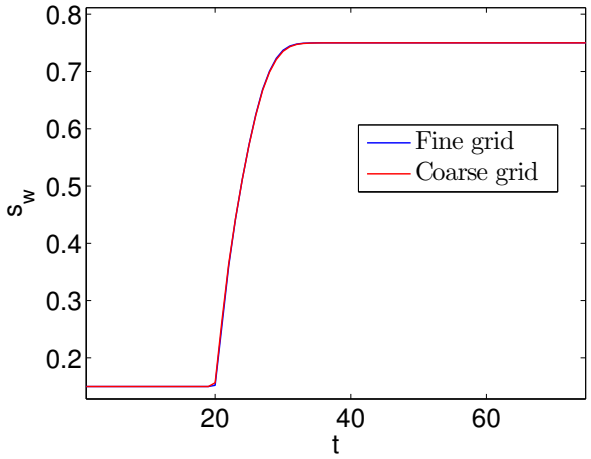

(a) Water saturation at outlet boundary as a function of time for fine and coarse grid with one type of rock for a two-phase system.

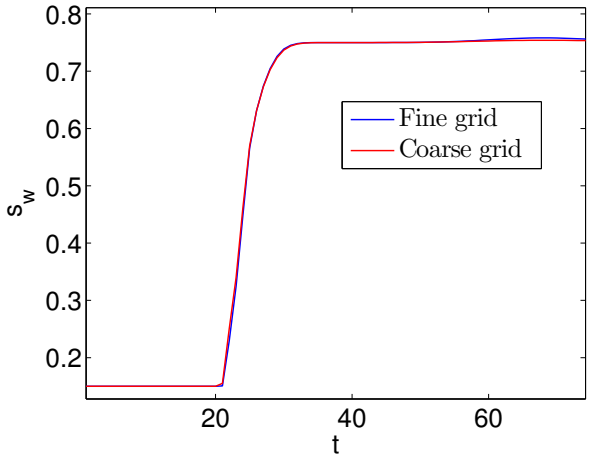

(b) Water saturation at outlet boundary as a function of time for the fine and coarse grid with one type of rock for a polymer flow system.

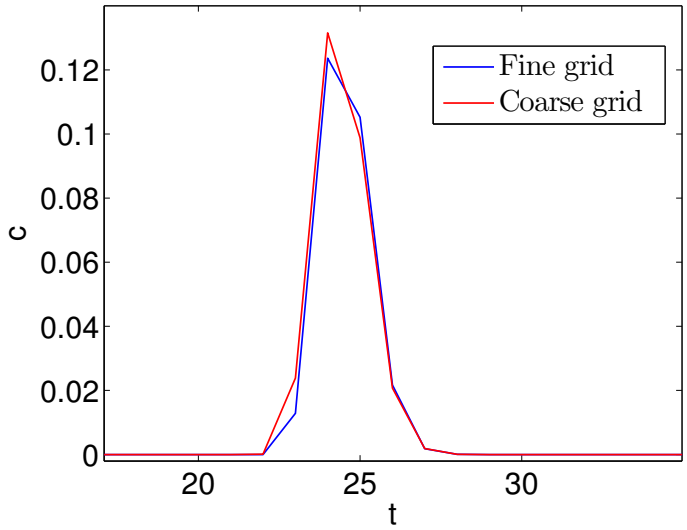

(c) Polymer concentration at outlet boundary as a function of time for the fine and coarse grid with one type of rock for a polymer flow system.

Figure 5.5: *Solutions obtained for the different grids when they consist of only one type of rock. The differences in the solutions are here only caused by solving on different grids, and the solutions obtained for the two grids are very similar.*

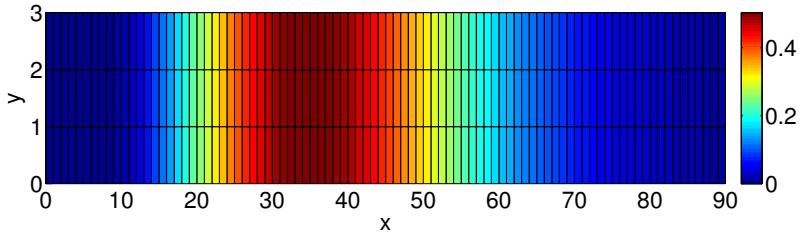

(a) Concentration in fine grid after 23 timesteps.

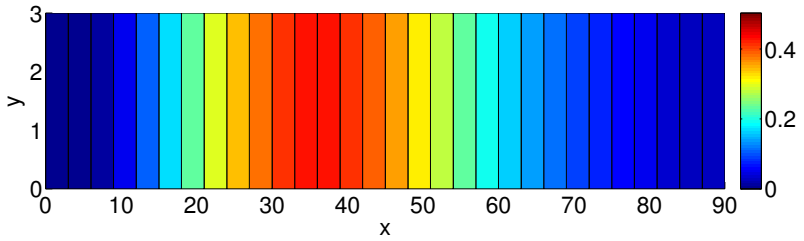

(b) Concentration in coarse grid after 23 timesteps.

Figure 5.6: *Concentration distribution in the fine and coarse grid after 23 time steps when there is only one type of rock in the grids. We see that the polymer spreads out in the water.*

5.2.2 Two-Phase Upscaling Results

Here, we evaluate the two-phase upscaling by comparing the solution obtained for a two-phase system using small-scale values on the small-scale grid with the solution obtained using upscaled values on the coarse grid. The water saturation at outlet boundary for the fine and coarse grid is plotted against time in Figure 5.7.

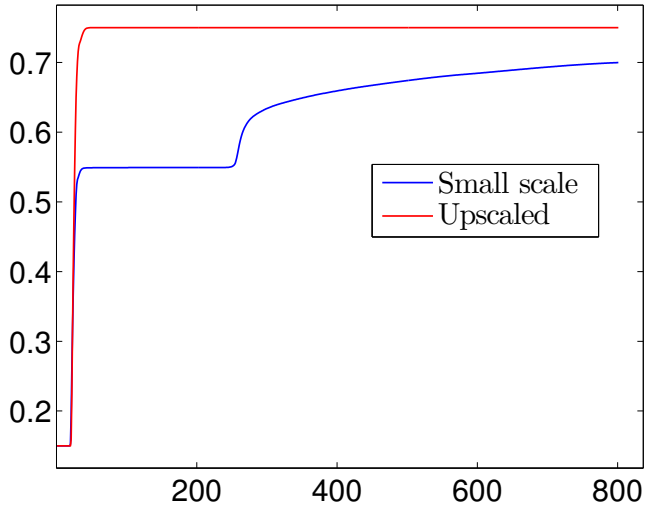

Figure 5.7: *Saturation at outlet boundary side versus time obtained for fine and coarse grid using small-scale and upscaled values, respectively. This is for a two-phase simulation. The small-scale curve bends off before the upscaled curve due to the low permeable layer in the small-scale grid.*

The small-scale curve bends off earlier than the upscaled because of the low permeable layer in the fine grid. Figure 5.8 shows the saturation distribution in the two grids after 25 and 100 time steps. In the small-scale grid water flows fastest through the top and bottom layers since these have the highest permeability. The layer in the middle has a much lower permeability, and we see that the water front moves a lot slower there. In the coarse grid each cell has the same properties, and thus the water front moves evenly. This explains why the small-scale curve bends off, while the upscaled curve does not.

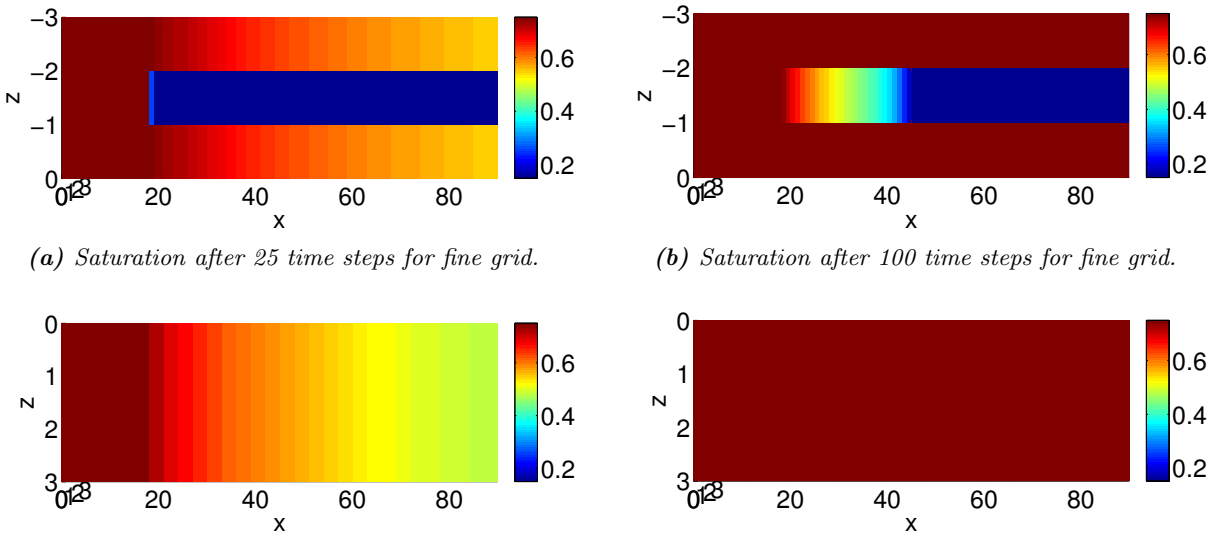

(a) Saturation after 25 time steps for fine grid.

(b) Saturation after 100 time steps for fine grid.

(c) Saturation after 25 time steps for coarse grid.

(d) Saturation after 100 time steps for coarse grid.

Figure 5.8: *Saturation distribution in fine and coarse grid after 25 and 100 time steps for two-phase flow. Water flows slow in the layer with low permeability on the fine scale, and this explains the shape of the curve in Figure 5.7.*

5.2.3 Polymer Upcaling Results

We consider the correctness of the polymer upscaling results by comparing the saturation and concentration at the outlet boundary face for the fine and coarse grid using small-scale and upscaled values, respectively. We obtained upscaled values for RRF that depend on saturation, and we here solve on the coarse grid using upscaled RRF values as functions of saturation, but also using the mean value of the upscaled RRF valules as a single upscaled value for RRF. This is to check how much the RRF dependence on saturation actually affects the solution, as the dependence did not seem to be very strong. So we compare the solutions obtained using small-scale values on the fine grid, using upscaled values on the coarse grid where upscaled RRF is a function of saturation, and using upscaled values on the coarse grid where upscaled RRF is the mean of $RRF^*(s)$. The saturations and concentrations at the outlet boundary sides are plotted in Figure 5.9 for polymer flow. The saturation curve is almost similar as to the one obtained for two-phase flow, and is plotted in Figure 5.9a. The concentration at the outlet boundary is plotted in Figure 5.9b versus time, and we see that there is a high peak after about 26 time steps, and also that the small-scale curve has a small peak after about 500 time steps. Figure 5.10 shows the concentration after 24 time steps in the fine and coarse grid, and we see that the polymer is moving slowly in the low permeable layer compared to the layers with high permeability. This is what causes the small peak in concentration

for the small-scale grid after about 500 time steps, as that is when the polymer moving through the low permeable layer reaches the outlet boundary side. Figure 5.9c shows a close-up of the highest concentration peak. The highest point of the peaks are at the same time step for small-scale and upscaled, but the shape of the peaks are a bit different.

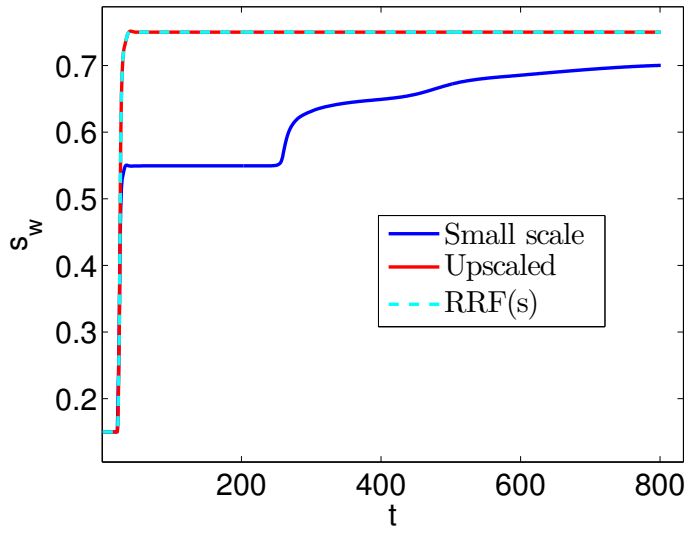

(a) *Saturation at outlet boundary as a function of time for the fine and coarse grid for polymer flow.*

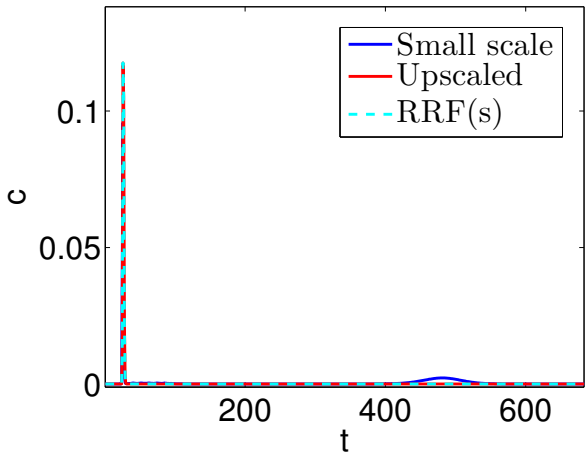

(b) *Concentration at outlet boundary as a function of time for fine and coarse grid.*

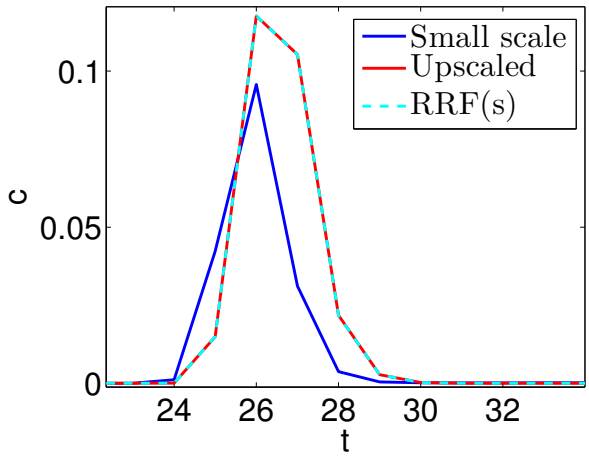

(c) *Close-up of the highest concentration peak in Figure 5.9b.*

Figure 5.9: *Comparison of solutions obtained for the fine and coarse grid using small-scale and upscaled values, respectively. This is for a polymer flow system. The red line with the legend upscaled is for solving with upscaled values where the mean of the upscaled RRF values are used as a a single upscaled value. The turquoise line is for upscaled values with the upscaled RRF values being functions of saturation.*

In Figure 5.9 it is difficult to see a difference between the solutions obtained using upscaled values where *RRF* is a function of saturation and using upscaled values where the mean value of *RRF* is used. We therefore zoom in to get a closer look, and this is done in Figure 5.11. We see that

there is practically no difference. So for this case we think that it is not necessary to include the dependence on saturation when using the upscaled RRF values, and that using the mean value gives satisfying results. For the simple layered grid the upscaled RRF values for the x-direction did not depend strongly on saturation, so for other cases where the upscaled values depends more strongly on saturation using the mean value of $RRF^*(s)$ may not give satisfying results.

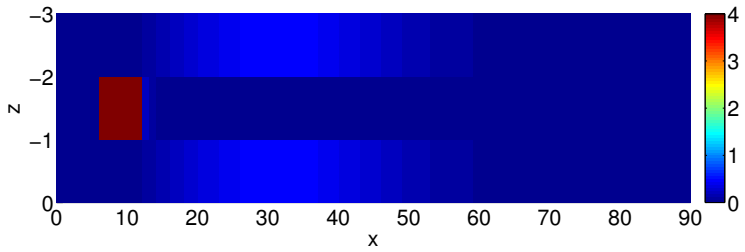

(a) Concentration after 24 time steps in fine grid.

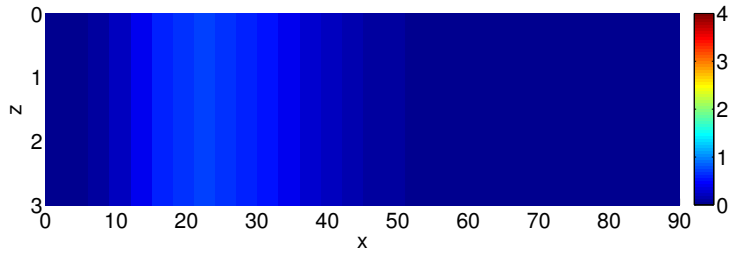

(b) Concentration after 24 time steps in coarse grid.

Figure 5.10: *Concentration distribution seen from the side of fine and coarse grid after 24 time steps. The polymer moves slower in the low permeable layer on small-scale as the water also moves slower there.*

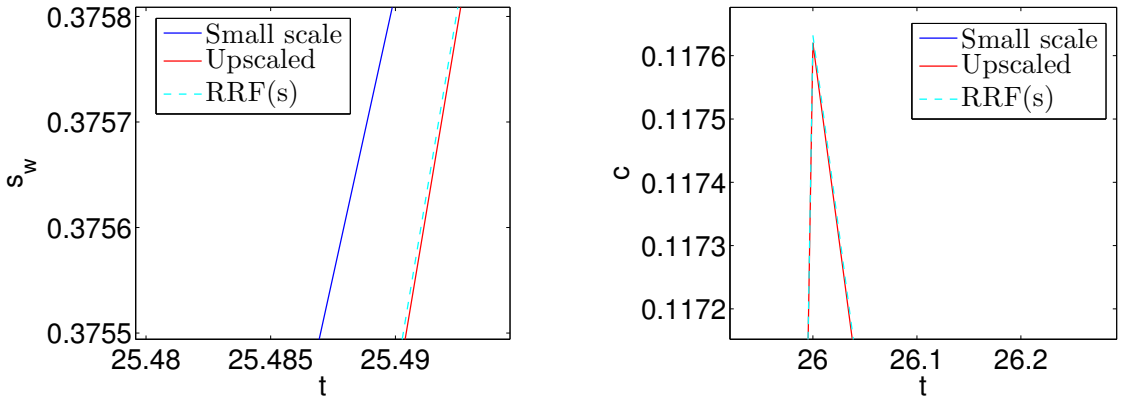

(a) Close-up of saturation curves for polymer flow. *(b) Close-up of concentration curves for polymer flow.*

Figure 5.11: *Close-up of saturation and concentration curves for polymer flow to have a closer look at the difference between using mean($RRF^*(s)$) and using $RRF^*(s)$. The difference is very small.*

5.3 Testing Oblong Grid

We now test the upscaling results for the oblong grid in Section 4.5 which consists of four types of rock. The grid consists originally of 400 cells, but is duplicated 10 times in the x-direction to evaluate the upscaling results. The duplicated fine-scale grid then consists of 1000x2x2 = 4000 cells, whereas the coarse grid consists of 10x1x1 = 10 cells in the x-direction. The duplicated small-scale grid is shown in Figure 5.12.

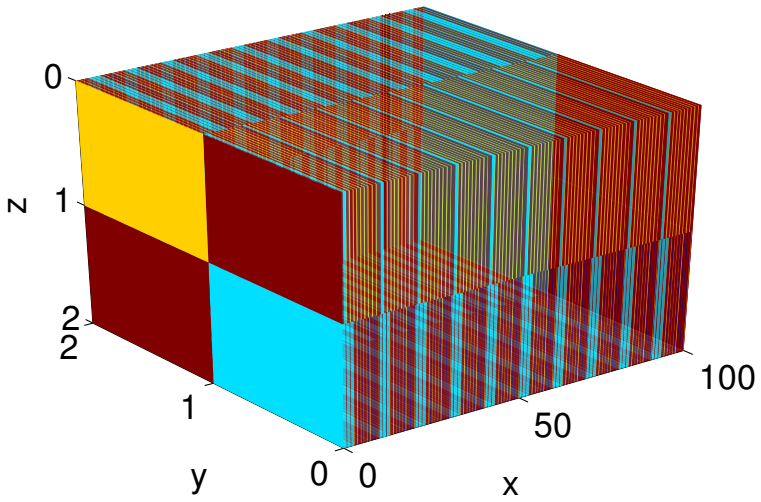

Figure 5.12: *Oblong grid duplicated 10 times in the x-direction. Colors indicate rock type.*

5.3.1 Difference Caused by Grids

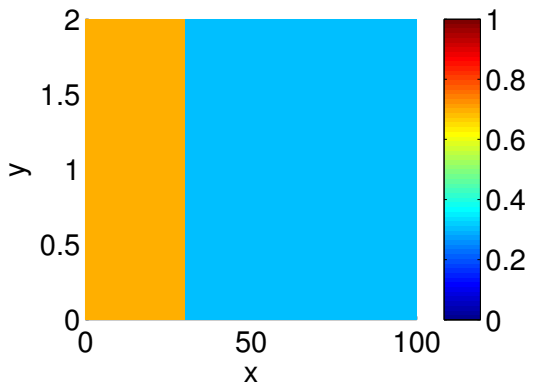

(a) *Initial saturation distribution. The water saturation is 0.7 in the water area and 0.3 in the oil area, and this is to keep in the range of saturations that the relative permeability curves are defined for.*

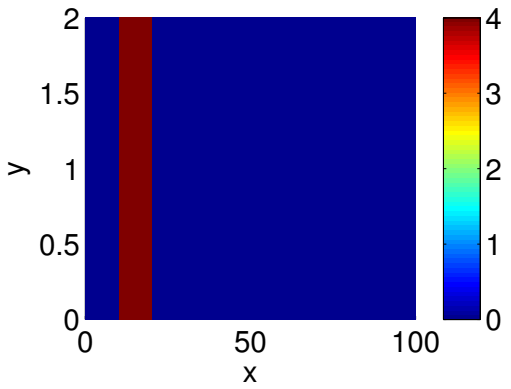

(b) *Initial concentration distribution. The concentration is zero everywhere except for a layer with $c = 4$ in the water area.*

Figure 5.13: *Inital set-up of saturation and concentration distribution. The set-up is the same for the fine and coarse grid, but the fine grid has many more cells than the coarse grid.*

Also here we start out with running simulations on the fine and coarse grid with the grids only containing one type of rock, so that we can see how different the solutions get simply because of the grids being different. Figure 5.13 shows the set-up at initial state. It is similar to the set-up used when evaluating the results for the simple layered grid, except that here the water saturations are 0.7 and 0.3 in the water area and oil area, respectively. This is to keep in the range of the saturations that the relative permeabilities are defined for. A pressure difference of 1 bar is set up over the domain in the x-direction to drive a flow in the positive x-direction.

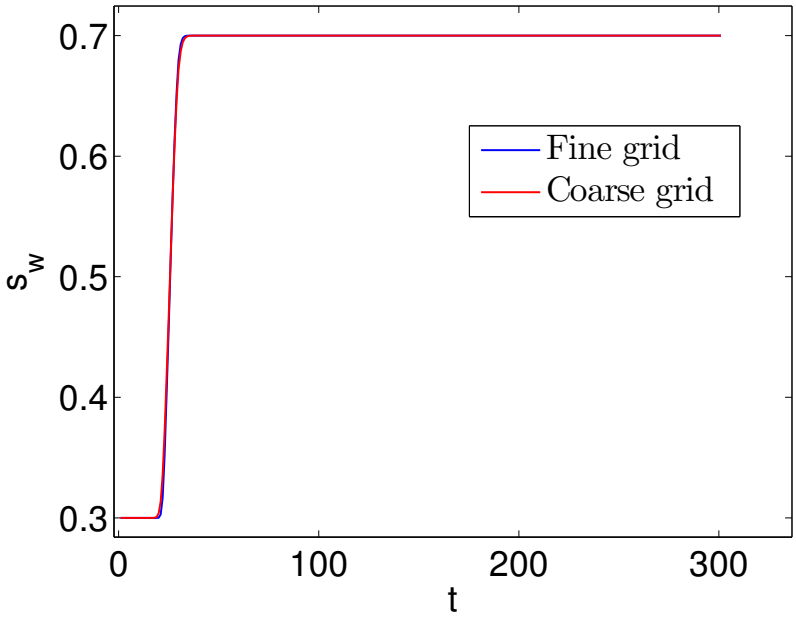

Figure 5.14: *Saturation at outlet boundary side versus time obtained for the fine and coarse grid when the grids consist of only one type of rock. This is for a two-phase simulation, and the curves obtained are very similar.*

For a two-phase system me measure the water saturation at the outlet boundary face at each time step, whereas for polymer flow we measure both the water saturation and polymer concentration. For two-phase flow the water saturation at the outlet boundary for the two grids are plotted in Figure 5.14, and the results obtained for the two grids are very similar. The water saturations at the outlet boundary face of the two grids for polymer flow are plotted in Figure 5.15. These are also fairly similar, but not as similar as for two-phase flow. For the fine-scale grid there is a small peak just after the saturation at the outlet boundary face has become 0.7, and this is after about 30 time steps. The water saturation is a bit higher than 0.7 here, and this is because the layer of polymer that is put in the water makes the water accumulate a bit. The accumulated water moves to the right, and the small peak represents the accumulated water reaching the outlet boundary face. Water with polymer has a higher viscosity than pure water, and will thus flow slower. This will make the water accumulate a bit as mainly water will come in from the left side. As time goes, the polymer spreads out and the accumulation will stop. For the coarse grid we do not see this effect at first sight, but if we zoom in we see that also the saturation for the coarse grid has a small peak at about the same place, but this peak is much smaller as not so much water is accumulated for the coarse grid. Figure 5.16 shows the saturation distribution for polymer flow for the fine and coarse grid after 30 time steps. We see that in both grids the polymer makes the water accumulate, but the accumulation is larger in the fine than in the coarse grid.

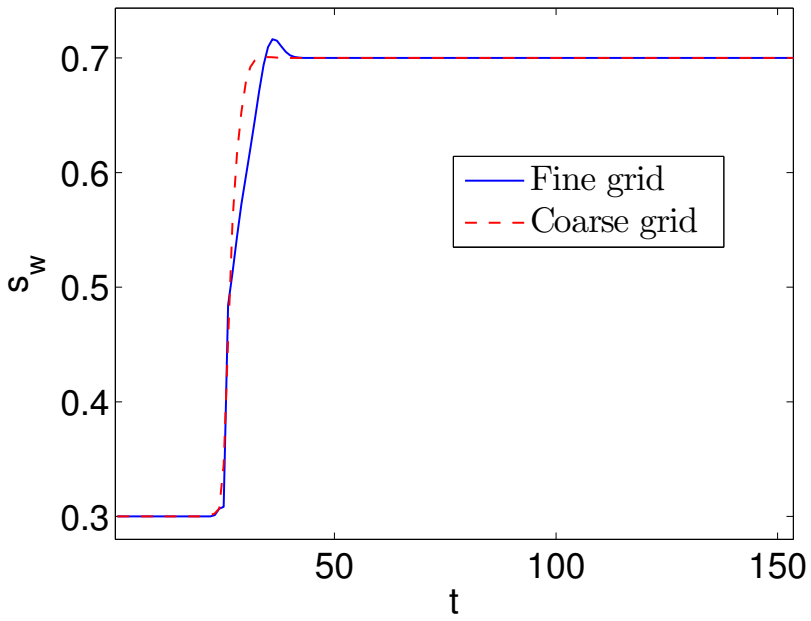

Figure 5.15: *Saturation at outlet boundary face versus time obtained for the fine and coarse grid when the grids consist of only one type of rock. This is for a polymer flow simulation.*

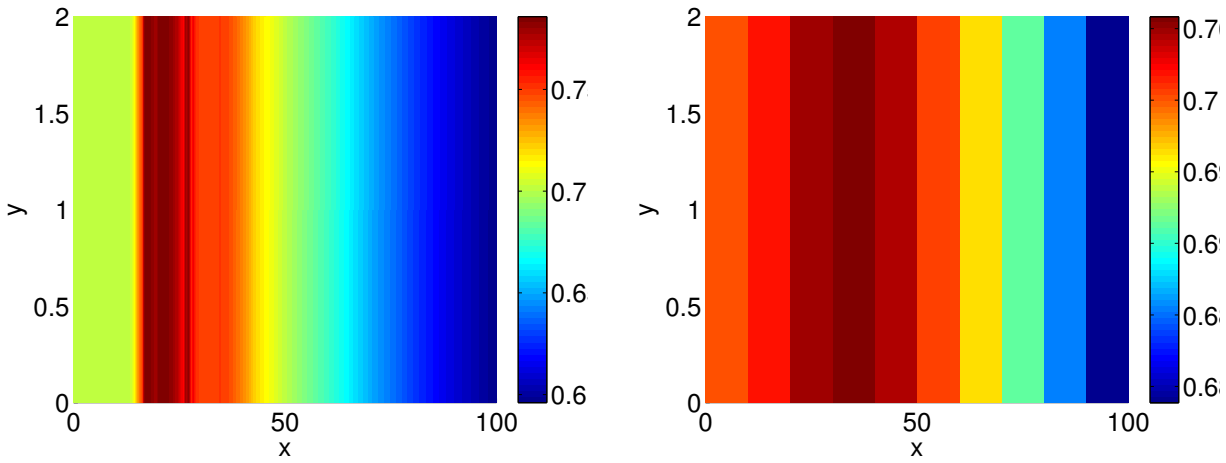

(a) *Saturation distribution in fine grid after 30 time steps for a polymer flow simulation.*

(b) *Saturation distribution in coarse grid after 30 time steps for a polymer flow simulation.*

Figure 5.16: *Saturation distribution after 30 time steps for polymer flow for fine and coarse grid when the grids consist of only one type of rock. Water is accumulated due to the presence of polymer, and is more accumulated in the fine grid than in the coarse grid.*

The polymer concentration at the outlet boundary face is plotted against time in Figure 5.17. The highest point of the curve is at the same time step for both small and coarse scale, but the coarse scale peak is a bit shifted to the left. Also the peak of the coarse scale is a bit higher than the small-scale concentration peak.

We have here seen how much the curves will differ when there is no upscalig effect, and the difference

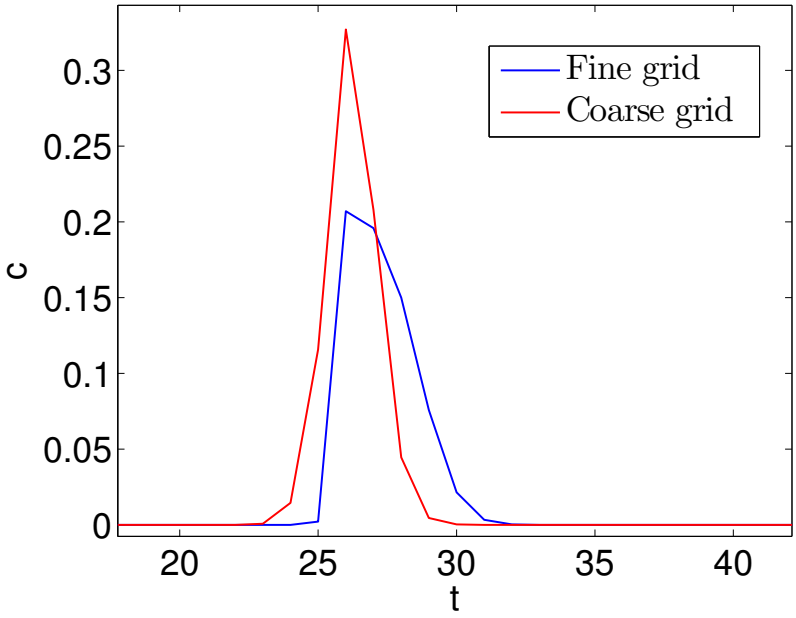

Figure 5.17: *Concentration at outlet boundary face versus time obtained for the fine and coarse grid when the grids consist of only one type of rock. The peak in concentration is a bit higher for the coarse grid.*

in solutions just being caused by solving on different grids. When performing upscaling with several types of rock in the small-scale grid and there actually being an upscaling effect, the curves will no matter how good the upscaling is, differ as much as the curves obtained here. Since the upscaling is an approximation, the curves will differ more than here.

5.3.2 Two-Phase Upscaling Results

We next consider the solution of the small-scale grid with different types of rock and the solution of the coarse grid with the corresponding upscaled values. The saturation curves versus time are plotted in Figure 5.18. The curves are pretty similar, but the small-scale curve has a minimum after about 30 time steps where the water saturation at the outlet boundary face is below 0.3, and this is not captured by the upscaling. For the coarse grid all the cells have the same properties, and thus the fluids flow evenly through the grid. On fine scale the permeabilities are different in different cells, and thus the fluids will prefer to go through certain cells and the flow will not be even through the grid. Figure 5.19 shows the saturation distribution in the fine and coarse grid after 35 time steps for a two-phase simulation. We see that the water saturation is higher in certain layers in the rock.

5.3.3 Polymer Upscaling Results

We here check the results obtained for the upscaling of polymer flow by comparing the saturation and concentration at the outlet boundary face for the fine and coarse grid using small-scale and upscaled values, respectively. We also here solve on the coarse grid with upscaled RRF values as functions of saturation and with a single upscaled RRF value which is the mean of the RRF values for different saturations. The saturation at the outlet boundary as a function of time for polymer

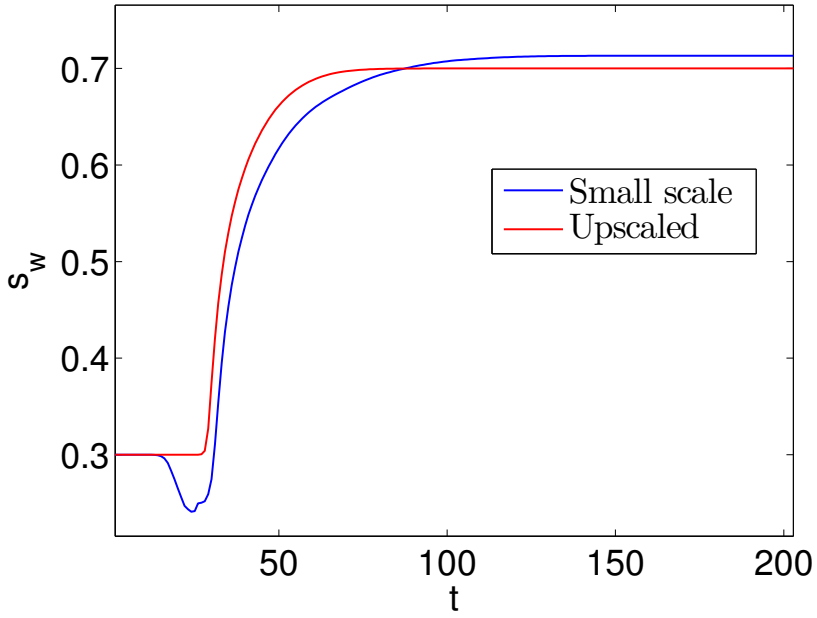

Figure 5.18: *Saturation at outlet boundary side versus time obtained for the fine and coarse grid using small-scale and upscaled values, respectively. This is for a two-phase simulation. The curves are relatively similar, but the small-scale curve has a local minimum that is not captured by the upscaling.*

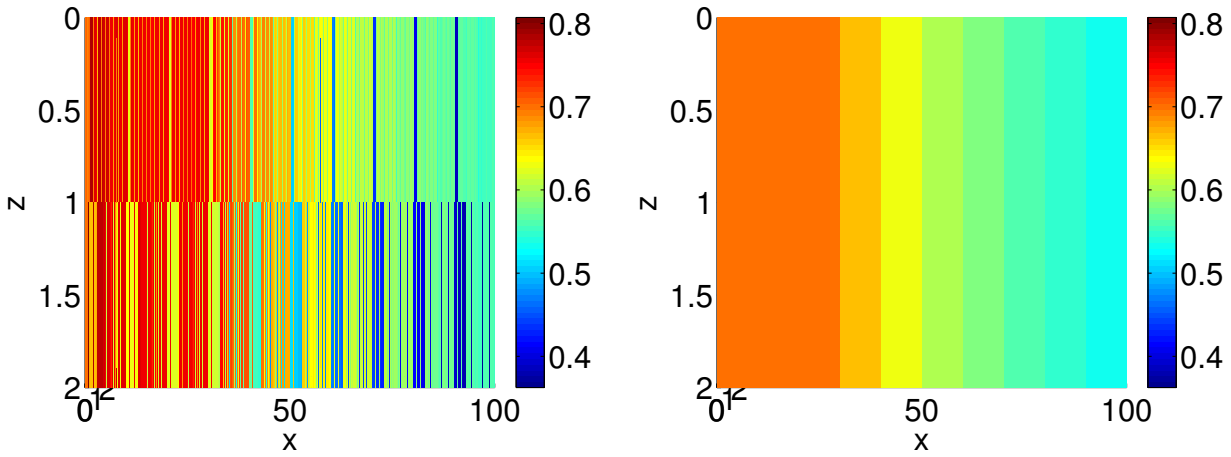

(a) *Saturation in fine grid.* ***(b)*** *Saturation in coarse grid*

Figure 5.19: *Saturation distribution for two-phase system in fine and coarse grid after 35 time steps. In the small-scale grid the water prefers to be in certain layers in the rock, whereas on coarse scale the cells have the same properties and thus the water front will flow evenly.*

flow is plotted in Figure 5.20 for the two grids. The small-scale curve has a local minimum which is not captured by the upscaling, but as we also saw this for the two-phase simulation we know that this is an effect from the upscaling of permeabilities, and not from the polymer upscaling. The water saturation is above 0.7 for a range of time steps for both the small-scale and upscaled solution, which

is caused by the polymer making the water accumulate. This we also saw when the grids consisted of one type of rock and there was no upscaling. The saturation is above 0.7 for a longer time for the small-scale curve than for the coarse-scale, so the curves deviates a bit from each other, but still they are relatively similar.

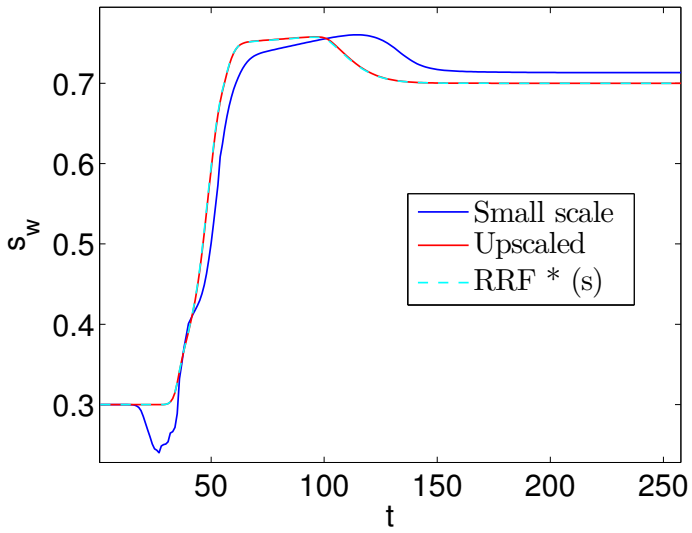

Figure 5.20: *Saturation at outlet boundary face versus time obtained for the fine and coarse grid using small-scale and upscaled values, respectively. This is for a polymer flow simulation. The red line with the legend upscaled is for solving with upscaled values where the mean of the upscaled RRF values are used as a a single upscaled value. The turquoise line is for upscaled values with the upscaled RRF values being functions of saturation. The upscaled curves deviates a bit from the small-scale curve, but still they are relatively similar.*

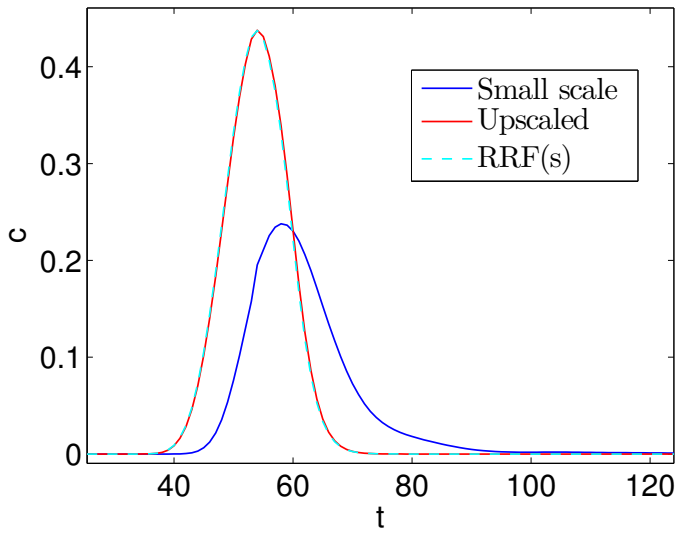

Figure 5.21: *Concentration at outlet boundary face versus time obtained for the fine and coarse grid using small-scale and upscaled values, respectively. The legends have the same meaning as in Figure 5.20.*

The concentration at the outlet boundary as a function of time for polymer flow is plotted in Figure 5.21 for the two grids. The peak for the coarse grid is higher than the small-scale peak, but this we also saw when the grids consisted of one type of rock, and thus we believe this mainly to be an effect of the grids being different. The peak for the upscaled curve is also a bit shifted to the left. This was also the case when there was only one type of rock in the grids, but here the peak has been more shifted relative to the peak of the small-scale curve. Figure 5.22 shows the concentration distribution in the fine and coarse grid after 40 time steps. We see that the polymer moves slower and certain layers in the rock on the fine scale.

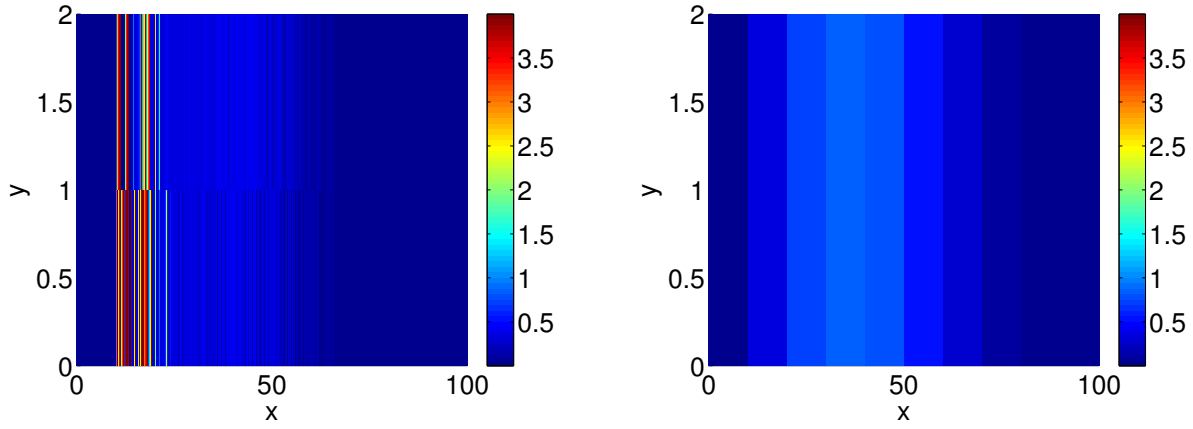

(a) Concentration in fine grid. *(b) Concentration in coarse grid.*

Figure 5.22: *Concentration distribution in fine (left) and coarse (right) grid after 40 time steps. The range of the colorbar is the same for easy comparison. See that for the fine grid polymer gets "stuck" (moves very slow) in some layers in the rock.*

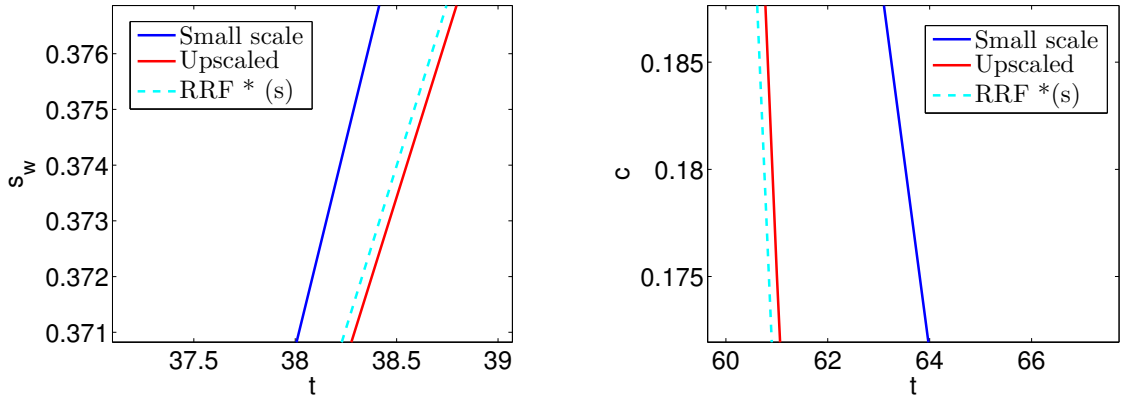

(a) Close-up of Figure 5.20, which shows the saturation at the outlet boundary for polymer flow. *(b) Close-up of Figure 5.21, which shows the concentration at the outlet boundary.*

Figure 5.23: *Close-up of saturation (left) and concentration (right) at outlet boundary obtained using $RRF^*(s)$ and using mean($RRF^*(s)$) to look at the difference between the solutions.*

When looking at Figure 5.20 and 5.21 it is difficult to see any difference between the curves obtained from using upscaled RRF values as functions of saturation and using the mean of the upscaled values. We therefore zoom in to get a closer look, and this is done in Figure 5.23. The solutions are

very similar, but there is a difference. However, we believe that the difference is small enough for the saturation dependence to be neglected, and that using the mean of the values will give satisfying results in this case.

5.4 Summary

In this chapter we have evaluated the upscaling results obtained for two of the grids in Chapter 4. We have compared the solutions obtained using small-scale parameters on the fine grid with solutions obtained using upscaled parameters on a coarse grid. The solutions appear to be in good agreement, though some small-scale effects are not captured by the upscaling. We compared the solutions obtained using upscaled RRF values as functions of saturation with solutions obtained using the mean value of $RRF^*(s)$ as a single upscaled value. The solutions did not differ much, and thus using the mean value of $RRF^*(s)$ appears to be a good approximation that produces satisfying results for the cases studied here. However, more tests should be run to see if this is valid for other cases.

Chapter 6

Discussions and Conclusions

In this thesis upscaling of polymer flow has been considered. Upscaling of single- and two-phase flow has already been studied extensively [8], but when it comes to upscaling of polymer flow we have not been able to find any literature concerning this, and thus we pretty much started from scratch. In this chapter we summarize the upscaling procedures used, discuss the results obtained and the conclusions drawn from them.

6.1 Discussions

One of the many methods that can be used for two-phase upscaling is to simulate to steady-state and then performing flow-based upscaling. We have used this method for the upscaling of relative permeabilities, and also chose to use this method for the upscaling of polymer flow. We started out by considering a possible upscaling effect of the mixing parameter and the viscosities of water and polymer. From the equations, we found analytically that at steady state the polymer concentration will be constant in space, and from this it follows that there will be no upscaling effect of the viscosities and the mixing parameter. We attempted to upscale the viscosities and the mixing parameter numerically by performing steady-state and flow-based upscaling, and also then found that there is no upscaling effect. Next, we considered the upscaling of the permeability reduction factor, and also here we performed steady-state and flow-based upscaling. We found that the upscaled values depend both on direction and saturation. The amount of adsorbed polymer was upscaled using volume averaging. The upscaled residual resistance factor has been found from the slope of the upscaled permeability reduction factor versus the upscaled adsorbed polymer concentration, and also became a function of saturation and direction. We have considered the upscaling of four different systems, where the results obtained for two of these have been tested.

6.1.1 Upscaling of C_p^a

Upscaled values for C_p^a have been found using volume averaging. For the simple layered grid other simple averaging techniques were also tested, but these did not appear to produce more satisfying results than volume averaging. We therefore decided to continue to upscale C_p^a using volume averaging. Volume averaging has the advantage of being a very simple and fast method, and no flow simulation is needed to obtain upscaled values. One might question how good the values obtained using this simple method are, and this should be further tested by comparing with results obtained

using more advanced methods. This is left as further work. A possibility would be to instead use volume averaging to upscale RRF, and then find upscaled C_p^a from the slope of upscaled R_k versus upscaled RRF. However, this would produce upscaled C_p^a values that would be functions of both concentration and saturation.

6.1.2 Upscaling of R_k and the Dependence on Saturation

The permeability reduction factor was upscaled for each direction and for different saturations, and the upscaled values were found to depend on both direction and saturation. The small-scale values of R_k produce straight lines that do not depend on saturation when plotted against C_p^a. Upscaled R_k values plotted against upscaled C_p^a values produce lines that are not perfectly straight and that depends on saturation. How strong the dependence on saturation is, varies for different systems, but it does not appear to be a certain pattern in the dependence. The upscaled R_k values are found using upscaled relative permeabilities which depend on saturation, and we believe that this is causing the upscaled R_k values to depend on saturation. The non-linearity occurring for the upscaled R_k values versus upscaled C_p^a we believe to be caused by the upscaling of C_p^a. For the simple layered grid the lines were straight when there was no upscaling effect of C_p^a, but became non-linear when there was an upscaling effect. We also saw that in some cases the upscaled R_k values versus upscaled C_p^a values were outside the range of the small-scale values, and also this we believe to be an effect from the upscaling of C_p^a. This typically happened for grids that consist of layers of rock and for upscaling in the directions where the flow was only along the layers, and not across.

6.1.3 Upscaling of RRF and the Dependence on Saturation

Upscaled RRF values are found using the upscaled R_k values, and as these depend on saturation and direction, so do the upscaled RRF values. Hence, RRF goes from being a scalar on small-scale to being dependent on both direction and saturation when it is upscaled. How much RRF^* depends on saturation varies for different grids, but the variation for a certain direction is typically about 0.1-0.2 for the grids we have studied. On small-scale RRF is a constant value, and introducing it as a function of saturation would complicate the model. We therefore consider and suggest to replace the upscaled RRF values that are functions of saturation with a single upscaled RRF value which is the mean of the saturation dependent values. In Chapter 5 we compared solutions obtained using upscaled RRF values as functions of saturation with solutions obtained using the mean value of the saturation dependent RRF^* values as a constant upscaled value, and the solutions were very similar. We therefore suggest to neglect the saturation dependence of the upscaled RRF values, and instead use the mean of the values as a single upscaled value. However, more tests should be run to see if this is a good approximation also for other cases. For cases where the upscaled RRF values depend more on saturation than what is seen here, using the mean of the values as a single value may not produce satisfying results.

6.1.4 Evaluation of the Upscaling Results

In Chapter 5, solutions obtained using upscaled parameters on coarse grids were compared to solutions obtained using small-scale parameters on fine grids for two of the cases in Chapter 4. The solutions naturally differ, and the upscaling does not capture all small-scale effects, but still the solutions are relatively similar. The water breakthrough happens at almost exactly the same time

when using upscaled parameters as when using small-scale parameters, and also the polymer reaches the outlet boundary at about the same time using the two grids. The upscaled values found for the other grids in Chapter 4 should also be tested, but this is left as further work. For the two grids for which the results were tested, we conclude that the upscaling works well and captures the main flow pattern. In the future, tests should also be run for large, realistic grids where the grids are divided into blocks that are upscaled, and then the upscaling results are tested by solving for the whole grid using small-scale values and for the upscaled grid using upscaled values.

6.1.5 Numerical Challenges

We have seen that the number of cells that the program can handle is highly dependent on the number of types of rock in the grid. The number of cells and types of rock the program can handle is something that most likely can be improved, but this has not been the focus here. This should however be done in the future so that upscaling of larger and more complex grids can be performed. We also saw that for complex grids it can be difficult to obtain steady state. Solving and reaching steady state goes fast and is unproblematic for simple grids, but for more advanced grids the solver struggles and a steady state is not always found. This has not been studied in detail here, but making a good guess about the solution at steady state and using this as the initial state may help. If the cells of the grid are too small, this may cause problems as it can cause the solution to have problems converging. Another reason for a system not reaching steady state may be that the time scale it would take for the system to actually reach steady state is too long, and that the system is not simulated for a long enough time. Understanding the problems with the steady state solver and improving it is left as further work.

6.1.6 Other Remarks

The upscaling results were obtained using $\omega = 1$, which corresponds to full mixing between water and polymer. A few tests were run for different values of ω, but the same upscaled values were obtained. We therefore believe that the upscaling results are independent of the mixing parameter, and thus independent of the degree of mixing between water and polymer.

Based on the fact that the upscaling of relative permeabilities depends on the pressure difference over the domain, we also expected that this might be the case for the upscaling of R_k. This was barely tested, and the upscaled values obtained using another pressure gradient were slightly different. How the upscaled values depend on the pressure gradient should be proper and further tested.

Upscaling of dead pore space has not been considered here, but as this is practically just a new porosity, we suggest to upscale S_{dpv} using volume averaging since that is how porosity is upscaled.

6.2 Alternative Approaches and Future Research

The goal of this thesis has been to develop techniques for upscaling of polymer flow. This goal has been reached by using steady-state methods and volume averaging to upscale parameters in the polymer equations. The upscaling techniques used in this thesis are only a few of the many various techniques that exists and can be used. In further studies, the techniques used here should be tested further by upscaling more complex systems and more advanced grids. The upscaling results should also be evaluated by comparing the flow pattern obtained using upscaled parameters on a coarse grid

with the fine-scale flow-pattern. Other methods for upscaling polymer flow should also be studied and the results compared to the results obtained using steady-state upscaling. We encountered some challenges when trying to upscale more advanced grids, and thus the solver and upscaling routine should be made more efficient and robust, so that it can handle more complex grids. Qualified guesses should be made for the initial conditions so that steady state can be reached faster. Also the steady state solver should probably be better understood and improved, so that steady state is reached for most systems.

Upscaling of polymer flow is a broad field where still lots of work and studies need to be done to obtain a decent knowledge about the subject. We still have many questions that are yet to be answered, and some of these may provide the base for future studies:

- How will including gravity and capillary forces affect the upscaling results?
- How are the upscaling results affected by the boundary conditions used in the upscaling? Which boundary conditions produce the best results?
- Will alternative upscaling techniques produce more satisfying results?
- How will including dead pore space affect the flow and results, and how should it be upscaled?
- Do the polymer upscaling results depend on the pressure gradient?
- Does upscaling C_p^a using volume averaging produce satisfying results? Should a more advanced method be used?
- How do upscaled RRF values depend on saturation for different grids?
- Is it necessary to include the dependence on saturation when using the upscaled RRF values, or can it be neglected?

6.3 Conclusions

For a system in steady state the polymer concentration will be uniform in space, and from this it follows that there is no upscaling effect of the mixing parameter and the viscosities. The upscaled values of the permeability reduction factor R_k depend on both direction and saturation. Upscaled values for the residual resistance factor RRF are found using these values, and thus also depend on direction and saturation. On small-scale the residual resistance factor is a scalar value for each rock type, and introducing a saturation dependence would complicate the model.

The saturation dependence of RRF appears to be weak, and solutions obtained using the mean of the saturation dependent upscaled RRF values are very similar to solutions obtained using the upscaled RRF values as functions of saturation. Therefore, we suggest to neglect the saturation dependence and instead use the mean of the upscaled RRF values as a single upscaled value.

Bibliography

[1] J. E. Aarnes, T. Gimse, and K.-A. Lie. *Geometrical Modeling, Numerical Simulation, and Optimization: Industrial Mathematics at SINTEF*, chapter An introduction to the numerics of flow in porous media using Matlab, pages 261–302. Springer Verlag, 2007.

[2] J. E. Aarnes, V. Kippe, K.-A. Lie, and A. B. Rustad. Geometrical modeling, numerical simulation, and optimization: Industrial mathematics at sintef. pages 303–356, 2007.

[3] K. Bjorlykke. *Petroleum Geoscience*. Springer Heidelberg Dordrecht London New York, 2010.

[4] P.L. Bondor, G.J. Hirasaki, and M. J. Tham. Mathematical simulation of polymer flooding in complex reservoir. *SPE Journal*, 12(5):369–382, 1972.

[5] Z. Chen, G. Huan, and M. Yuanle. *Computational Methods for Multiphase Flows in Porous Media*. Society for Industrial and Applied Mathematics, 2006.

[6] M. A. Christie. Upscaling for Reservoir Simulation. *Journal of Petroleum Technology*, 48(11): 1004–1010, 1996.

[7] M.A. Christie. Flow in porous media - scale up of multiphase flow. *Current Opinion in Colloid and Interface Science*, 6(3):236–241, 2001. ISSN 1359-0294.

[8] Louis J. Durlofsky. Upscaling of geocellular models for reservoir flow simulation: A review of recent progress. In *7 th International Forum on Reservoir Simulation*, pages 23–27, 2003.

[9] S. Jakupsstovu, D. Zhou, J. Kamath, L. Durlofsky, and E. H. Stenby. Upscaling of miscible displacement processes. In *Proceedings of the 6th Nordic Symposium on Petrophysics*, 2003.

[10] R.R. Jennings, J.H. Rogers, and T. J. West. Factors influencing mobility control by polymer solutions. *Journal of Petroleum Technology*, 23, 1971.

[11] K.-A. Lie, S. Krogstad, I. S. Ligaarden, J. R. Natvig, H. M. Nilsen, and B. Skaflestad. Open source MATLAB implementation of consistent discretisations on complex grids. *Computational Geosciences*, 16(2):297–322, 2012. ISSN 1420-0597. doi: 10.1007/s10596-011-9244-4.

[12] Lars Vingli Odsæter. Numerical Aspects of Flow Based Local Upscaling. Master's thesis, Norwegian University of Science and Technology, 2013.

[13] *ECLIPSE reservoir simulation software, Technical Description*. Schlumberger, 2011.1 edition.

[14] J. J. Sheng. *Modern Chemical Enhanced Oil Recovery*. Elsevier, 2011.

[15] K. S. Sorbie. *Polymer-improved Oil Recovery*. Glasgow: Blackie, 1991.

[16] M.R. Todd and W.J. Longstaff. The Development, Testing, and Application Of a Numerical Simulator for Predicting Miscible Flood Performance . *Journal of Petroleum Technology*, 24(7): 874–882, 1972.